THE UNIVERSITY OF

WARWICK

University of Warwick institutional repository: http://go.warwick.ac.uk/wrap

A Thesis Submitted for the Degree of PhD at the University of Warwick

http://go.warwick.ac.uk/wrap/3820

Time-Resolved Studies of the Photodissociation of Adenine

Kym Lewis Wells

Submitted for the qualification of Doctor of Philosophy.

University of Warwick.

Department of Chemistry.

April 2010

Table of Contents

List of Figures

List of Tables

Acknowledgements

Declaration

This thesis represents, to the best of the author's knowledge, original material. The work is solely that of the author, except where due credit is given in the text. This thesis has not been submitted for the award of any degree to any institute other than the University of Warwick.

Kym Lewis Wells

Publications

1.   "Dynamics of H-loss in adenine via the $^1\pi\sigma^*$ state using a combination of   ns and fs laser spectroscopy"; K. L. Wells, G. M. Roberts, V. G. Stavros; *Chem. Phys. Lett.*, **446**, 20 (2007)

2.   "Time-resolved velocity map ion imaging study of the NH_3 photodissociation"; K. L. Wells, G. Perriam, V. G. Stavros; *J. Chem.   Phys.*, **130**, 074308 (2009)

3.   "Competing $\pi\sigma^*$ states in the photodissociation of adenine"; K. L. Wells, D. J. Hadden, M. G. D. Nix, V. G. Stavros; *J. Phys. Chem. Lett.*, **1**, 993 (2010)

4.   "Imidazole derivatives as models for the UV photodissociation of adenine"; K. L. Wells, D. J. Hadden, M. G. D. Nix, V. G. Stavros; *Chem. Phys. Lett.*, *to be submitted* (2010)

Abbreviations

Abstract

A novel time-resolved velocity map ion imaging (TR-VMI) experiment has been constructed and successfully applied to the study of non-statistical dissociation processes.

The photodissociation of NH_3 following the population of the $v_2' = 4$ umbrella vibrational mode of the first electronically excited, $\tilde{A}^1A_2''$, singlet state, was initially studied. It was clearly observed that the N-H dissociation timescale was inversely proportional to kinetic energy released to the H fragment. Assignment of different kinetic energy regions of the TR-VMI transients to corresponding bending vibrational modes (v_2) of the $\tilde{X}^2B_1$ state NH_2 photoproduct clearly suggests that dissociation into the vibrationless NH_2 occurs in < 50 fs. Low kinetic energy channels, show extended dissociation timescales, strongly indicative of adiabatic dissociation to the first electronically excited state of NH_2 ($\tilde{A}^2A_1$).

With an aim of modelling the photodissociation dynamics of adenine, the photodissociation of pyrrole, imidazole, 2-methylimidazole, 4-methylimidazole and 2,4-dimethylimidazole following excitation at 200 nm were studied using time-resolved mass spectrometry (TR-MS) and VMI. In all cases ultrafast H elimination was observed in < 130 fs, consistent with direct dissociation via the repulsive $^1\pi\sigma^*$ potential energy surfaces. The photodissociation of 1-methyimidazole at this wavelength was also studied. Once again ultrafast H elimination was observed, but with greatly reduced yields, strongly suggesting

H elimination from the non-heteroatom co-ordinates (C-H) also partaking in the photodissociation dynamics at this wavelength.

TR-MS and VMI have also been applied to the study of the photodissociation of adenine, 9-methyladenine and 6-dimethylaminopurine. In all measured kinetic energy spectra a high kinetic energy channel has been observed, strongly suggesting the participation of $^1\pi\sigma^*$ potential energy surfaces of both the azole and amino co-ordinates in H elimination following excitation at 200 nm. Power dependence studies at 266 nm suggest H elimination, but subsequent TR-MS measurements seem to suggest that this is not due to the participation of the $^1\pi\sigma^*$ potential energy surfaces at this excitation wavelength.

1. Introduction

1.1 Early Indications of Ultra-fast Processes

Over the past century advances in experimental methodologies have enabled the temporal resolution at which we are able to investigate chemical processes to greatly increase[1-2]. This has enabled us, for example, to gain a greater understanding of how the motion of atoms within a molecule influences chemical reactivity.

The early potential energy surface (PES) of the H + H_2 reaction developed by Eyring and Polanyi[3] allowed chemists for the first time to envisage dynamical processes across these PES's, which would eventually give rise to "femtochemistry", a relatively recent development in experimental methods which allows real time investigation of the transition states of chemical processes on the femtosecond (1 fs = 1 x 10^{-15} s) timescale.

Critical to this however, was the later work carried out by Eyring[4] and separately Evans and Polanyi[5] towards development of transition state theory, which in itself was an extension of Arrhenius's work towards relationships between temperature and rates of reactions[3] which yielded equation 1.1. In this equation, the rate constant k (for any two reacting species) is dependant on the temperature T, the activation energy required to initiate the reaction E_a, which is unique to the reaction in question, R the universal gas constant and A the pre-exponential factor.

$$k = Ae^{-E_a/RT} \qquad\qquad (1.1)$$

Evans and Polanyi's work led to the formulation of transition state theory which yielded an explicit expression for the pre-exponential factor, shown in equation 1.2.

$$k = \frac{k_B T}{h} K^{\neq} = \frac{k_B T Q^{\neq}}{h Q_A Q_B} e^{-E_0/kT} \qquad (1.2)$$

where k_B is Boltzmann's constant, h is Planck's constant, $K^{\neq}$ is the constant for the formation of the activated complex, or transition state (TS), Q is the partition function for the reactant species (A and B) and the TS (the partition function is a normalised thermal distribution over the density of states) and E_0 is the zero point energy corrected activation energy. This equation shows that the fastest reaction is given by $k_B T/h$, which is equivalent to the frequency of passage through the transition state. At room temperature this equates to 6.2×10^{12} reaction events passing through the TS per second, corresponding to approximately 160 fs for the fastest bi-molecular reaction at 298 K. This result clearly showed the necessity of temporally short sampling methods (from hundreds to tens of fs resolution, and indeed smaller as technology continues to improve) to investigate processes involving molecular motion in real time.

1.2 Short Pulses from Broad Bandwidths

By observation of the line-widths of spectroscopic transitions it is possible to determine the timescale of the transition between the states involved, by virtue of the time-energy uncertainty relationship.

$$\Delta\tau = \frac{\left(\dfrac{4\ln 2}{2\pi}\right)}{\Delta E} \qquad (1.3)$$

$$\Delta\tau = \frac{\left(\dfrac{\ln 2}{\pi}\right)}{\Delta E} \qquad (1.4)$$

Equation 1.3 gives the relationship between lifetime τ and full width half maximum (FWHM) E for a transform limited, Gaussian pulse (where the time-bandwidth product is assumed to be at its minimum value) whilst equation 1.4 shows the same relationship for a Lorentzian pulse (essentially the pulse is born of a homogeneous transition).

Whereas equations 1.3 and 1.4 offer mathematical solutions to this relationship for specific pulse types, the general time-bandwidth product (equation 1.5) offers a general solution.

$$\Delta E \Delta \tau \geq \hbar \qquad (1.5)$$

Where $\hbar$ is the reduced Planck's constant ($h/2\pi$). This relationship clearly shows that if the lifetime τ is short, then the energy uncertainty must be large.

1.3 Franck-Condon Principle

Allowed vibronic transitions, where a vibrational transition and electronic transition occur simultaneously, can be understood in terms of the Franck-Condon principle. That is, since nuclei are much heavier than electrons (proton = 1.67 x 10^{-27} kg, electron = 9.11 x 10^{-31} kg), electronic transitions occur much faster than nuclear motion. As such intense transitions occur vertically, where there is minimal perturbation on the displacement of the nuclei relative to their equilibrium position, and where there is greatest overlap between the ground and excited state wavefunctions. That is not to say that other localised states will not be populated, as these too will have appreciable probability of having overlap at the equilibrium internuclear separation (**Figure 1.1**).
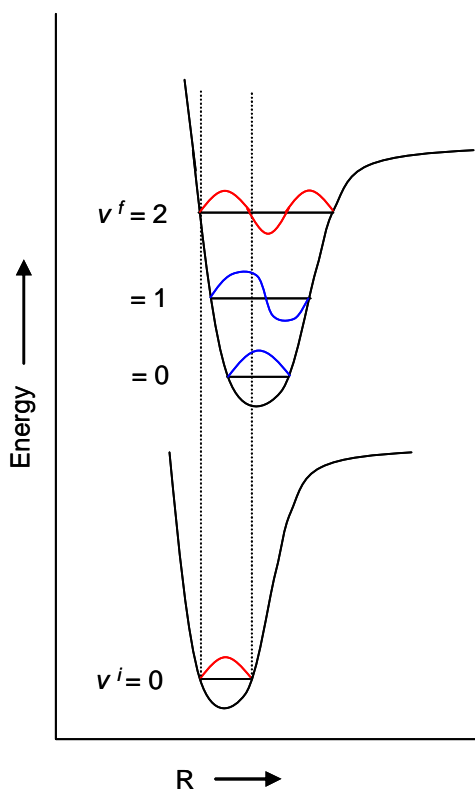
Figure 1.1, most likely transition is highlighted in red (dashed lines to guide the eye), as this has the greatest overlap between ground and excited state wavefunctions, and with minimal displacement from the equilibrium nuclear configuration.

The wavefunctions describing initial and final states (ψ^i and ψ^f respectively) can be broken down to electronic and vibrational components, as shown by equations 1.6 and 1.7.

$$\psi^i = \psi_e^{\;i}\psi_v^{\;i} \qquad (1.6)$$

$$\psi^f = \psi_e^{\;f}\psi_v^{\;f} \qquad (1.7)$$

$$S = \int \psi_v^{\;f}\psi_v^{\;i} dR \qquad (1.8)$$

The intensity of these vibronic transitions are proportional to the square modulus of the transition dipole moment, $|\mu_{fi}|^2$, which in turn is proportional to the square modulus of the overlap integral (Franck-Condon factor) between the initial vibrational state and final vibrational state, $S(v_f, v_i)$ (equation 1.8). When $S = 1$, there is maximum overlap between the two vibrational wavefunctions, when $S = 0$, there is minimal overlap. As a result, the larger the value of S, the greater the transition probability.

1.4 Laser Developments

In much the same way that Q-switching (generation of pulses by controlling the stimulated emission of the gain medium) has enabled the generation of nanosecond (1 ns = 1 x 10^{-9} s) laser pulses, modelocking techniques have enabled the generation of ultrashort pulses ranging from picoseconds (1 ps = 1 x 10^{-12} s) to fs. As a result, this has allowed real-time observation of chemical processes to become a viable alternative to frequency resolved techniques (however, initial work began in the 1960's[6-7]).

In a lasing system, the bandwidth (and hence temporal profile) of a generated pulse is limited by the number of axial modes *N* supported by the cavity of length, *L*, and the gain medium. The number of axial cavity modes multiplied by the energy separation of these modes, $\Delta \upsilon$, gives the bandwidth. The pulse width is given by the inverse of the bandwidth, the relationship between these properties is shown in equations 1.9 and 1.10 where c' is the speed of light through the cavity medium.

$$\Delta \upsilon = (\Delta \tau N)^{-1} = \frac{c'}{2L} \qquad (1.9)$$

$$\Delta \tau = (N \Delta \upsilon)^{-1} \qquad (1.10)$$

These expressions assume that all resonant modes are of equal intensity. In real laser systems this is not true. In a laser medium, the resonant mode intensities are de-scaled by a Gaussian line-shape function. As such the relationship becomes

$$\Delta \tau = \frac{\left(\dfrac{4 \ln 2}{2 \pi} \right)}{N \Delta \upsilon} \qquad (1.11)$$

which is essentially equation 1.3. Generation of ultrafast pulses can either be attained by active or passive methods. In active mode locking the cavity loss is modulated using an external optical component (e.g. an acousto-optic modulator). In doing this only pulses with round trips synchronised with this

perturbation are able to survive and amplify through further stimulated emission. Typically active mode locking techniques generate ps pulses.

Early lasers generating ultra-short pulses (tens of ps to hundreds of fs) were based on dye systems. The large optical bandwidth over which the gain medium can support stimulated emission allows temporally short pulses. Discovery of titanium doped sapphire (Ti:Al$_2$O$_3$) as a lasing medium[8] has allowed solid state lasers to become the preferred choice for ultra-short pulse generation. This four level laser system has a whole manifold of states that allow a very broad spectral bandwidth to amplify, as shown in **Figure 1.2**, and given that $\Delta\tau$ is proportional to $1/N\Delta\upsilon$, this results in very short pulses. Since in a four level laser system the radiative transition from state a to state b has been decoupled from the ground state, re-absorption of the emitted light is greatly reduced (state b undergoes ultrafast relaxation back to the ground state). As such less pumping intensity is required to obtain a suitable population inversion compared to a traditional three level system.
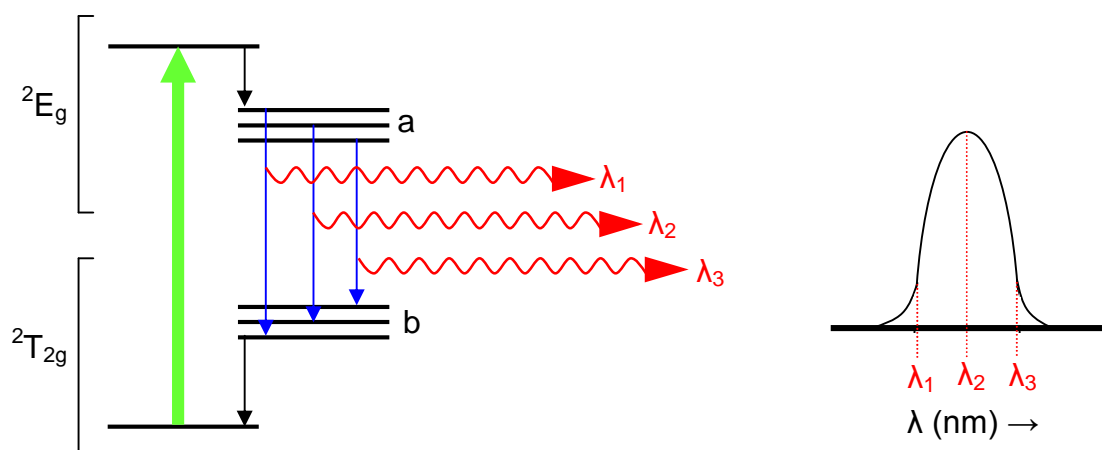
Figure 1.2, depiction of vibronic transitions available in Ti:Al$_2$O$_3$, which enable large optical bandwidth transitions.

Passive mode-locking exploits the optical Kerr effect, as shown in equation 1.12 where n is the refractive index of the medium, n_2 is the non-linear index of refraction of the medium (or optical Kerr coefficient) and I is the optical intensity. Equation 1.12 describes the change in the refractive index of a region of medium exposed to a strong electric field relative to that of the medium not experiencing the field. Ultrafast pulses have very high intensities, and as such cause this effect to occur in the gain medium. This results in "self focussing"[9], illustrated in **Figure 1.3**, of the pulse as it traverses through the medium, as the pulse train intensity continues to grow. Pulsed lasers exploiting this phenomenon have recorded temporal pulse widths much shorter (~ 5 fs) than their non-passive counterparts.

$$\Delta n = n_2 \cdot I \qquad (1.12)$$
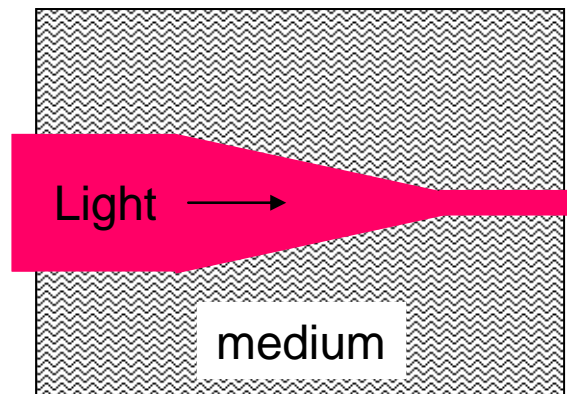
Figure 1.3, self focussing of an intense beam of light (strong electric field) via the optical Kerr effect as it passes through a medium.

Femtosecond lasers have found use in dynamics experiments and have proved useful tools for the development of coherent control experiments[10-12].

_____

1.5 Important Experimental Techniques

The understanding of dynamics in isolated (gas phase) molecules has been greatly aided by the development of several different experimental techniques. What follows is a description of these techniques and how these can be applied to study ultrafast processes relevant to the work carried out in this thesis.

1.5.1 Multiphoton Ionisation

Until the advent of lasers, exploration of multiphoton processes was not possible, due to the weak intensity of such transitions which involved non-resonant states. With the increased field strength offered by laser systems experimental observation of such processes became achievable[13].

Of particular importance in the context of this work are multiphoton ionisation mechanisms (MPI). A selection of possible ionisation schemes are shown in **Figure 1.4**.
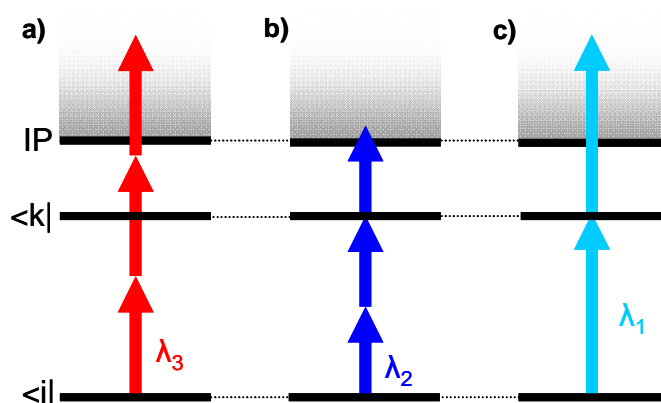
Figure 1.4, schematic of 3 possible MPI schemes: a) non-resonant multiphoton ionisation; b) 2 + 1 REMPI; and c) 1 + 1 REMPI. Other schemes are possible.

_____

Non resonant MPI is the simplest case of these kinds of processes, where absorption of more than one photon is required to exceed the ionisation potential (IP) of the atom or molecule, the initial photon populating a virtual state prior to ionisation. If an excited state within the species of interest is resonant at the one or two photon level, the efficiency of this process is greatly increased, through resonance enhanced multiphoton ionisation (REMPI). This is only possible if the transition probability from the ground state to the resonant intermediate state has a non-zero probability.

The probability, A_{if}, of a two photon transition within a molecule moving with a velocity, v, from the ground sate, S_i, to an excited state, S_f, via an intermediate state, S_k, can be written as[14]:

$$A_{if} \approx \frac{\gamma_{if} I_1 I_2}{\left[\omega_{if} - \omega_1 - \omega_2 - v \cdot (k_1 + k_2)\right]^2 + \left(\gamma_{if}/2\right)^2} \times \left| \sum_k \frac{R_{ik} \cdot \hat{e}_1 \cdot R_{kf} \cdot \hat{e}_2}{\omega_{ki} - \omega_1 - v \cdot k_1} + \frac{R_{ik} \cdot \hat{e}_2 \cdot R_{kf} \cdot \hat{e}_1}{\omega_{ki} - \omega_2 - v \cdot k_2} \right|^2$$

(1.13)

ω_1 and ω_2 correspond to the frequency of the two photons. k_1, $\hat{e}_1$, I_1 and k_2, $\hat{e}_2$, I_2 are the respective wave vectors, polarization unit vectors and intensities of the two light waves, γ_{if} is the linewidth for the transition and R_{ik} and R_{kf} are the matrix elements of the $S_k \leftarrow S_i$ and $S_f \leftarrow S_k$ transitions.

When S_k is a virtual state it is a linear combination of all allowed one photon transitions from S_i, and as such population of the virtual state borrows intensity from all possible allowed transitions. This means that with a finite laser

bandwidth, there is only limited population of the virtual state. That is when R_{ik} and R_{kf} are small, A_{if} is also small.

In the resonant case when $\omega_1 + \omega_2 = \omega_{if}$ the first factor in equation 1.13 increases, resulting in an increase in A_{if}.

1.5.2 Probing Kinetic Energy

In the photodissociation of a molecule AB we may characterise this process in terms of energy in the system, due to the conservation of energy using equation 1.14[15],

$$E_{photon} + E_{AB} = D_0(A - B) + E_{trans} + E_A + E_B \quad (1.14)$$

where, E_{photon} is the photon energy, E_{AB} is the internal energy within AB, E_A and E_B are the internal energies of the photoproducts A and B and E_{trans} is the total translational energy imparted upon A and B during the dissociation. Partitioning of translational energy between fragments A and B is dictated by the reduced mass, as shown in equation 1.15.

$$\mu_{AB} = \frac{M_A \times M_B}{M_A + M_B}$$

$$(1.15)$$

μ_{AB} is the reduced mass of the molecule AB and M_A, M_B are the respective masses of fragments A and B. The reduced mass shows the splitting of the E_{trans} into the distinct photoproducts by conservation of momentum (that is

$M_A V_A = M_B V_B$ where V_X is the velocity of the respective product). For example, in the photodissociation of ammonia (M_{NH2-H} = 0.94), with the photoproducts NH_2 (M_{NH2} = 16) and H (M_H = 1), 94 % of the total translational energy, E_{trans} is deposited onto the H photofragment.

With prior knowledge of the dissociation energy and careful observation of kinetic energy release, one is able to infer information with regards to the internal energy of the photofragments.

1.5.2.1 Doppler Spectroscopy

The wavelength of light absorbed (λ) by an atom moving with a velocity (V) relative to the incoming light compared to the wavelength of light absorbed by a stationary atom (λ_0) is described by equation 1.16[15].

$$\lambda = \lambda_0 \left(1 \pm \frac{V}{c} \right) \qquad (1.16)$$

where c is the speed of light. It is clear that if photodissociation yields a range of velocities over its photoproducts, then the lineshape with respect to this absorption is broadened. This provides us with information regarding the kinetic energy distribution of the photodissociation products.

1.5.2.2 Photofragment Translational Spectroscopy

Using equation 1.14 we can see that by knowing the dissociation energy of a molecule and by measuring the kinetic energy of a photodissociated fragment using a well-defined photon energy, we can infer information regarding the internal quantum states of the two photofragment products.

Following a photodissociation event, the kinetic energy of each fragment shown in equation 1.17, can be summed to give the total kinetic energy release (TKER) as represented in equation 1.18.

$$KE = \frac{1}{2}mv^2 \tag{1.17}$$

$$TKER = \frac{1}{2}m_A v_A^2 + \frac{1}{2}m_B v_B^2 \tag{1.18}$$

Observation of H elimination using this method has become popular, since the internal energy term for the H fragment is zero, simplifying equation 1.14. As momentum is conserved in the photodissociation, the *TKER* can be re-written as shown in equation 1.19, where the conservation of momentum has been taken into account, and the velocity is now represented by the field free region (*L*) and the time of flight of the H (t_H).

$$TKER = \frac{1}{2}m_H\left(1 + \frac{m_H}{m_A}\right)\left(\frac{L}{t_H}\right)^2 \tag{1.19}$$

Equation 1.14 can be now re-written as equation 1.20.

$$E_{photon} = D_0(A - H) + E_A + TKER \qquad (1.20)$$

Since the dissociation energy of a particular species is, in most cases, already known (and if not, may be directly inferred from the *TKER* spectra), as is the exact energy of a photon, measuring the *TKER* in this manner gives direct information regarding the internal quantum states of the unobserved fragment (*A*).

Previous photofragment translational spectroscopy experiments would ionise the H atoms at the interaction region[16]. More recent experiments have used Rydberg tagging[17], by optically exciting the H following dissociation to a high Rydberg state, and allowing them to pass down the flight path, immediately before the detector, a small electric field ionises these H photoproducts ready for detection. In doing this space/charge effects are eliminated which blur the kinetic energy released, improving the kinetic energy resolution.

1.5.3 The Photoelectric Effect

The photoelectric effect was first mathematically described by Einstein in 1905[18], and first observed when metal surfaces were bombarded with monochromatic light. It was seen that electrons were ejected from a surface when the photon energy of the incident light exceeded a value (work function, Φ), characteristic of the metal itself. The velocity of the ejected electrons was

also observed to increase linearly with the increase of photon energy as it exceeded the value of the work function (equation 1.21). These observations also showed that varying the intensity of the incident light did not increase the kinetic energy of the photoelectrons, and bore no impact upon electron ejection if the photon energy was below that of the work function.

$$KE_e = \frac{1}{2}m_e v^2 = E_{photon} - \Phi \qquad (1.21)$$

Photoelectron spectroscopy is essentially the photoelectric effect in the gas phase. Following photoionization of a polyatomic molecule, the electron carries off the excess energy in the form of kinetic energy. The only difference is that we simply substitute the work function in equation 1.21 for the ionisation potential (IP) of the molecule of interest. The relationship between photon energy and kinetic energy of the ejected electron is shown in **Figure 1.5**.
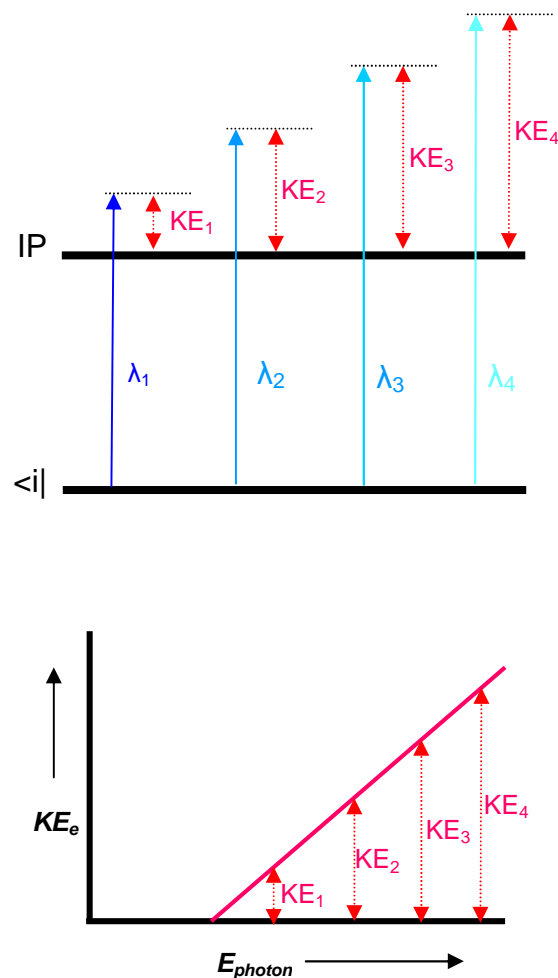
Figure 1.5, (top) plot showing relationship between photon energy and kinetic energy of ejected photoelectrons. (bottom) The intercept on the photon energy axis corresponds to the ionisation potential of the molecule.

Interpretation of photoelectron spectra requires the use of Koopman's theorem, which states that the ionization is instantaneous and that the ionisation energy is equal to the orbital energy of the ejected electron. This implies that we are able to determine the orbital from which the electron has departed from, with the observed bands (corresponding to different orbitals) also exhibiting vibrational structure.

The combination of this methodology with fs time-resolved pump probe methodologies (as discussed below), has enabled photoelectron spectroscopy

to be applied in a time-resolved fashion to help study complex ultrafast optically initiated processes[19].

1.6 The Nobel Prize

These new ultrashort laser pulses along with REMPI and photoelectron spectroscopy have been combined and applied to the study of real time dynamics, on the femtosecond timescale.

Early work by Zewail, regarding the photodissociation of ICN and NaI[20], successfully showed real time observation of unimolecular photodissociation, by carefully controlling the time delay between two laser pulses. This pump-probe methodology requires two steps. Firstly, optical excitation (pump) with the first laser pulse, propagating a coherent superposition of eigenstates (wavepacket) onto an excited state PES. Secondly, use of the second pulse (probe) to initiate an event that can be monitored as a function of the time delay between the pump and probe pulses that enables one to detect the condition of the photoexcited state (or products) at each temporal delay.

Zewail monitored the appearance of photoproducts as a function of temporal delay between the two pulses, and hence observed the photodissociation of both ICN and NaI in real time. In these measurements, the pump pulse photoexcited the molecule of interest while the probe pulse detected the photoproduct by further excitation of CN or I (depending on the system) leading to fluorescence. By recording the fragment's fluorescence intensity as a

function of pump/probe delay, Zewail was able to extract timescales for the photodissociation. In the NaI system, Zewail extended these measurements and also managed to observe the motion of the propagated wavepacket across the excited state PES. Observation of a series of steps in the fluorescence intensity at a series of pump-probe delays was indicative of bond contraction and elongation along the excited state PES.

This research along with other research completed in the late eighties and early nineties[1-2] earned him the Nobel Prize in chemistry in 1999. The techniques developed by Zewail are continually being used to this day to study the dynamics of a multitude of systems. One of the most studied systems of late using time-resolved spectroscopy is adenine.

1.7 Adenine- Motivations

Photostability of molecules in pre-biotic times was a large factor for determination of abundant molecular species, and as such photostability can be considered an environmental pressure that forced natural selection of the chromophores of biological molecules[21].

Of particular interest is the photostability of nucleic (acid) bases which are constituents of deoxyribonucleic acid (DNA). These relaxation pathways following photoexcitation must play a critical role to the potentially dangerous results that photo-induced damage may cause[22]. The fluorescence quantum yields of the nucleic acids is very low[23]. This suggests that very fast non-

radiative pathways diffusing potentially harmful internal energy are effectively competing with and overcoming the radiative relaxation processes[24].

Unravelling these fast non-radiative processes may therefore provide us with critical insight into why these molecules are so stable. The fact that these processes are very fast also means that time-resolved experiments are particularly pertinent here.
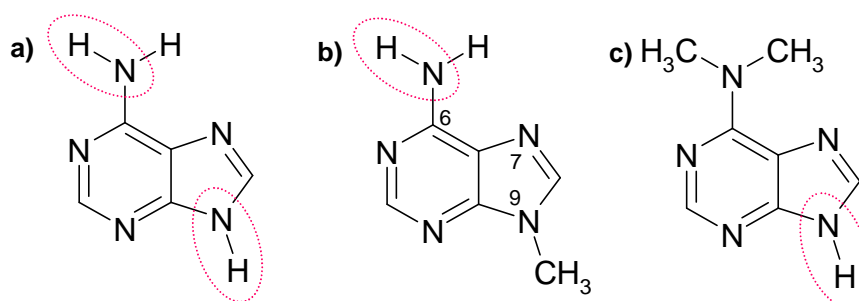
Figure 1.6, a) N^9-H adenine; b) 9-methyladenine; c) 6-dimethylaminopurine. Important heteroatom co-ordinates highlighted in red. 9-methyladenine ring structure numbered.

The primary aim of this body of research has been to understand and interpret the complex interplay of different dynamical process that result in the dissipation of energy following UV excitation of the DNA base adenine. In particular the involvement of dissociative mechanisms with respect to the heteroatom co-ordinates (highlighted) have been investigated, through time-resolved mass spectroscopy and velocity map ion imaging, both in adenine itself and model chromophore systems, shown in **Figure 1. 6**.

1.7.1 Theoretically Suggested Relaxation Mechanisms

Broo[25] was the first to try and understand these non-radiative processes using computational methods. He was able to identify possible relaxation mechanisms in 2-aminopurine and the N^7-H and N^9-H isomers of adenine which accounted for observed differences in the luminescence quantum yields. The first of these was proposed as a pseudo Jahn-Teller interaction, involving vibronic coupling of the first excited state with the ground state when large out of plane motion occurs in the adenine isomer. The absence of this channel in 2-aminopurine was attributed to the dissimilar bond length alterations on the six membered ring in the adenine isomers and 2-aminopurine, ultimately giving different force constants for the required out of plane bending mode that opens this channel. Differences between tautomerisation of the excited states was also suggested as a possible causes for different luminescence profiles, whilst a charge transfer mechanism from the ring system to the amino group was also identified, although this was noted as being small.
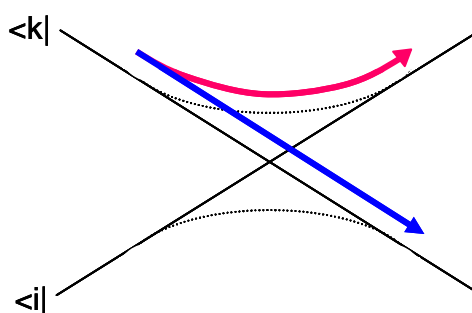
Figure 1.7, CI between PES i and k. Adiabatic surfaces, where Born-Oppenheimer approximation holds shown in dashed. Diabatic surfaces, where Born-Oppenheimer approximation fails shown in solid. Blue arrow shows non-adiabatic passage of a wavepacket through the CI between states i and k, red arrow depicts adiabatic dissociation, where the CI is avoided.

Further theoretical comparisons between 2-aminopurine and adenine have been drawn by Serrano-Andres *et al.*[26]. A local minimum on the ππ* surface on 2-aminopurine, which is energetically below the lowest conical intersection (CI) with the ground state[27] results in an energy barrier hindering wavepacket motion towards the ground state causing the differences in fluorescence quantum yield. A CI is a point of degeneracy between two PES's, as illustrated in **Figure 1.7**. CI's play a critical role in mediating non-adiabatic dynamics. In adenine, no local minimum was found and as such the wave-packet has a barrier-less reaction pathway to pass through this CI. Further CI's were found between the ππ* and nπ* surfaces in both molecules. Relaxation through these CI's were proposed to be of greater importance in the 9H-adenine isomer, as the barrier for this CI in the 7H isomer was slightly higher. Further characterisation of the PES's of 2-aminopurine has since accurately described deformations required in the six membered ring to access these CI's[28]. 6-aminopyrimidine has been investigated as a model for this puckering mechanism on the 6-membered ring[29-30].

Nielsen and Sølling[31], using time-dependant density functional theory (TDDFT) identified the N^9-H co-ordinate as being responsible for motion of the excited wavepacket away from the Franck-Condon region. They also concluded that a ring-puckering mechanism, and stretching along the N^9-C bond would also lead to the same effect. More recently, Barbatti and Lischka identified a plethora of CI's that arise as the pyrimidine and imidazole rings distort[32].

Marian[33], using combined density functional theory (DFT) and multireference configuration interaction (MRCI) methods calculated the electronic spectrum of 9H-adenine. At the Franck-Condon region, the nπ* surface was found to be only 0.1 eV below the ππ* surface. Marian suggested that the proximity of these two surfaces may result in ultrafast relaxation coupling between them. This work also suggests that this pathway will be active in adenine derivatives with substitutions at the N^9 co-ordinate.

Serrano-Andrés *et al.*[34] found that significant coupling occurred between the ππ*/nπ*, and suggested that this should result in sub-picosecond relaxation. In the same work, they also suggested a CI directly between the ππ* and S_0 surfaces should be active in the relaxation dynamics.
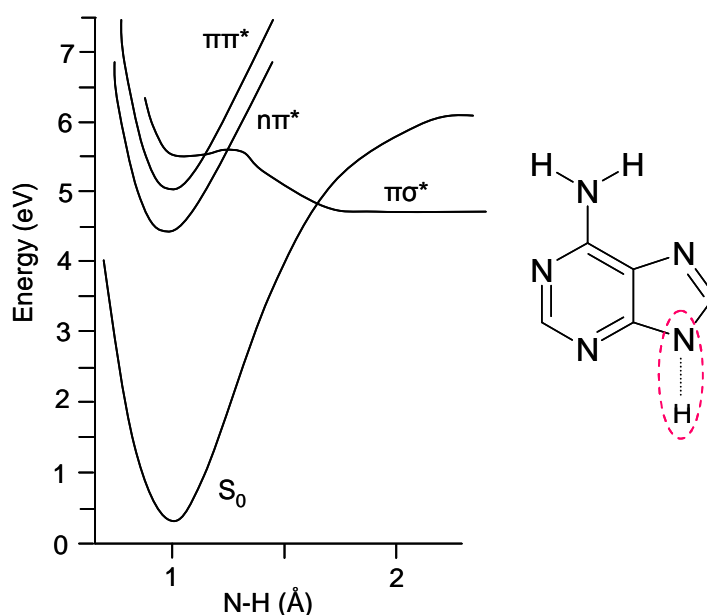
Figure 1.8, schematic of the PES of adenine, with respect to the N^9-H co-ordinate (highlighted). It is worthy of note that the PES of the amino co-ordinate is extremely similar to that of the azole. Adapted from reference 38.

The latest theoretically predicted pathway involves the dissociative πσ* surfaces identified by Sobolewski and Domcke[35-38] (**Figure 1.8**) and have

caused much controversy in the literature from an experimental standpoint (see below). These surfaces form CI's with the optically populated surfaces, providing a direct dissociative pathway for the propagated wavepacket to traverse towards direct dissociation, yielding H and adenyl co-fragments.

1.7.2 Experimental Gas Phase Investigations

Using resonant multiphoton ionisation (REMPI) over a range of wavelengths Kim *et al.*[39] were able to experimentally show where the nπ* and ππ* surfaces lie energetically, and which were later theoretically predicted to within fairly good agreement[33,40]. Further more, REMPI experiments found the most frequent form of adenine was the N^9-H tautomer, the spectrum dominated by a ππ* transition, with no direct optical population of the nπ* surface[41]. Theoretical calculations of oscillator strengths and experimental observations made by Kleinermanns group, suggest that optical population of the nπ* state is indeed probable[42].
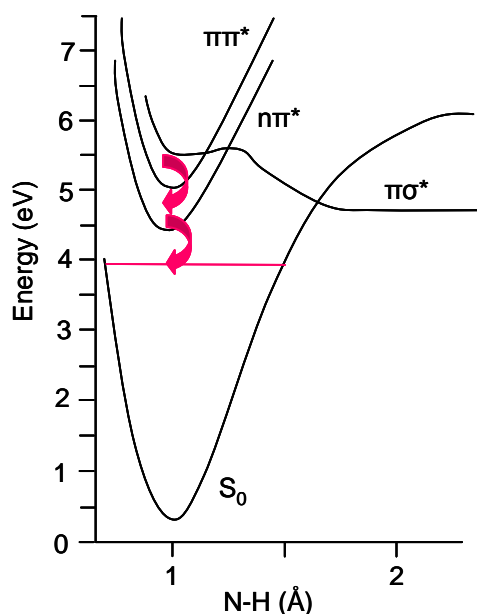
Figure 1.9, schematic depicting the slow internal conversion mechanism, linking the optically prepared $\pi\pi^*$ to S_0 via the $n\pi^*$ state. This results in population of a high vibrational mode (N-H) of the S_0 state.

Kang *et al.*[43] used fs Time-Resolved Mass Spectrometry (TR-MS) to investigate the photodissociation dynamics of adenine. By monitoring the adenine ion yield as a function of time delay between pump (267 nm) and probe (800 nm) laser pulses, they were able to directly observe the dissipation of energy within the adenine molecule. The decay timescales they observed for N^9-H adenine and N^9-methyl adenine were 1.00 +/- 0.05 ps and 0.94 +/- 0.03 ps respectively. These similar decay times, and relatively slow timescales suggested relaxation occurring through vibronic coupling between $\pi\pi^*$ and $n\pi^*$ before the wavepacket passing through a CI on route to the ground state surface shown in **Figure 1.9**. Under this same picture it was also assumed that the contentious $\pi\sigma^*$ does not play a significant role in relaxation dynamics at this wavelength. Femtosecond pump-probe transient absorption spectroscopy experiments in solution also found the N^9-H tautomer to be dominant[44]. The fitted decay timescales for the N^9-H and N^9-methyl derivative were found to be

the same (within experimental accuracy), and as such these authors again cited vibronic coupling between the ππ* and nπ* surfaces before passage to the ground state surface via a CI as the responsible relaxation mechanism.

The first experimental evidence that seemed to support the participation of the πσ* channel came from Stolow and co-workers[45-46]. Using time resolved photo-electron spectroscopy (TR-PES), they found evidence that upon excitation at 267 nm an ultra-fast component to their transients was observed which was consistent with what would have been expected with a purely dissociative state, and as such this was tentatively assigned as being due to the πσ* surface. Due to fact that in this experimental set-up they were able to correlate the measured kinetic energy of the electron versus time after initial wavepacket propagation, they were able to determine that internal conversion (IC) from the ππ* to the nπ* occurs in 50 fs (due to the large number of overlapping vibronic states), and that IC from the nπ* to ground occurs in 750 fs. Further experiments by Stolow and co-workers[47] compared the photoelectron spectra from N^9-H and N^9-methyl adenine. Although similar relaxation time-scales were recorded, distinctly different electron binding energies were identified. This led the authors to the conclusion that very different dynamical processes were taking place. In a more recent mini-review by these authors[48], they concede that more recent high-level ab-initio calculations do imply that the CI between the ππ* and πσ* is not energetically accessible at 267 nm.

Following photodissociation at 243 nm, Hünig *et al.*[49] were able to detect H (via a 2+1 REMPI mechanism), which they interpreted as being due to the repulsive

πσ* surface. Zierhut *et al.*[50] also observed H following photodissociation at both 239.5 nm and 266 nm. At 239.5 nm the Doppler profile of the resonantly (1+1 REMPI) detected H showed a clear perpendicular anisotropy (β_2 = -0.9), that is the photoproducts showed a clear angular dependence with respect to the laser polarisation (this will be discussed in detail later), indicating a very fast dissociative mechanism, while at 266 nm the Doppler profile was largely isotropic. Comparisons (at both wavelengths) of the mass spectra from N^9-H and N^9-methyl adenine showed markedly different H yields, suggesting the active participation of N^9-H fission as a competitive relaxation pathway, consistent with the proposed πσ* surface.

Canuel *et al.*[51], using fs TR-MS (and later TR-PES and photo-ion yield measurements[52]), examined the photodissociation dynamics following excitation at 267 nm. A bi-exponential fit to the observed N^9-H and N^9-methyl derivative revealed very similar decay dynamics, corresponding to transient decays of τ_1 = 100 fs, τ_2 = 1100 fs and τ_1 = 110 fs, τ_2 = 1300 fs respectively. This similarity was used to exclude the possibility of the involvement of the πσ* surface at 267 nm in N^9-H adenine. Instead, the fast component (~100 fs) was noted as being similar to the oscillatory period of the several out of plane vibrations, which are crucial to ring deformations which have been consistently calculated to be of potential importance to relaxation dynamics. The slow component (~ 1100 fs) was attributed to IC via the $\pi\pi^* \rightarrow n\pi^* \rightarrow S_0$ mechanism as reported elsewhere.
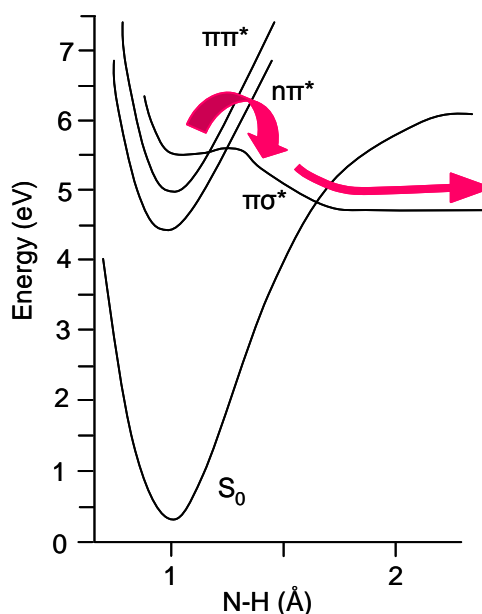
Figure 1.10, schematic depicting N-H bond fission along the dissociative πσ* surface, resulting in H and adenyl cofragment.

Total kinetic energy release (TKER) experiments by Ashfold *et al.*[53] examined the photodissociation of adenine at various photon energies between 280 and 214 nm. Their carefully conducted experiments which monitor accurately the kinetic energy imparted upon the H photo-product clearly showed that no fast dissociation pathways were observed until initial excitation energies at or below 233 nm. The observed fast structure was attributed to the N^9-H fission via the πσ* surface, as shown in **Figure 1.10**. As excitation energy increased (as excess energy above the ππ*/πσ* CI increased) the involvement of this channel was clearly seen to increase.

1.7.3 Dynamics Calculations

Chen and Li[54] reconciled the experimental lifetimes with computed surfaces. Their calculated surfaces showed a 0.137 eV barrier on the nπ* surface which has been cited as the source of the large 750 fs lifetimes for the excited nπ*

surface. Chin *et al.*[55] also compared experimental resonant two-photon ionisation (R2PI) line-width measurements with calculated lifetimes over a range of excitation energies. Similar trends between the two sets of data were observed. As excitation energy increased the lifetime decreased.

Barbatti and Lischka[32] were the first to complete true dynamics simulations on N^9-H adenine and 6-aminopyrimidine. In the N^9-H adenine simulations they showed that following population of the higher of the two ππ* surfaces (there are two ππ* surfaces in very close proximity in adenine), relaxation proceeds extremely fast, with this surface losing the entire wave-packet population within 25 fs. 50 % of this population was calculated to pass to the lower of the two ππ* surfaces, before passing to the nπ* surface, which has the entirety of the wave-packet population within 60 fs. After 75 fs depopulation of this state begins through a series of CI's due to distortion of the six membered ring. The authors determined the lifetime of the ππ*→nπ* process to occur on the timescale of approximately 22 fs, whilst the nπ*→S_0 was calculated as occurring on average in 538 fs. Although these values are in good agreement with what has been seen by Stolow[45-47], it is worthy of note that these simulations are from excitation at 5.12 eV (242 nm), an excitation energy not covered experimentally by Stolow and co-workers (highest excitation energy used was 250 nm).

Fabiano and Thiel[56] examined the relaxation of N^9-H adenine using surface hopping simulations. Following optical excitation into the higher ππ* surface, they found that relaxation occurred through a two step mechanism, with

ππ*→nπ* occurring in 45 fs and nπ*→S_0 occurring in 570 fs. These results are again in good agreement with Stolow[45-47]. In this study only the S_0, nπ* and ππ* (higher) surfaces are included in the simulations, as the Rydberg character of the πσ* surface made adequate description impossible.

Lei *et al.*[57] completed dynamics simulations at two different excitation energies, 5.0 eV (248 nm) and 4.8 eV (258 nm). At both excitation wavelengths they found that the wavepacket passes from ππ* to nπ* to S_0, albeit on different timescales. For the higher excitation energy, relaxation to S_0 occurred in 750 fs while at the lower excitation energy, relaxation occurred in 1120 fs, in good agreement with experimentally observed lifetimes[45-47,51].

1.7.4 Solvated Adenine

The study of condensed phase adenine can be split into two sub groups, cluster experiments, which act as intermediate experiments to connect gas phase data with true condensed phase data, and condensed phase experiments themselves.

1.7.4.1 Clusters

Using R2PI at 266 nm Kim *et al.*[58] compared relative yields of different $Adenine_m(H_2O)_n$ clusters with yields obtained through electron impact ionisation. They found that for clusters with n = 1 photoionisation yielded 1 % of that observed from electron impact ionisation, and for n ≥ 2, a 10 % relative

yield was observed. This disparity was attributed to the energetic increase of the $n\pi^*$ surface (which increases vibronic coupling with the adjacent $\pi\pi^*$ due to the closer energetic proximity) when clustered with proton donating solvents. This energy state rearrangement forces wave-packet propagation upon photo-excitation to reach a repulsive portion of the $n\pi^*$ surface, ultimately causing the hydrogen bonding between the H_2O and adenine to be weakened, resulting in dissociation of the cluster. In 2005 Kang *et al.* completed TR-MS measurements[59] which suggested that all water molecules are lost from the cluster within 200 fs due to the repulsive portion of the $n\pi^*$ surface. Later studies by Ritze *et al.*[60], featuring both theoretical studies and TR-MS measurements, came to different conclusions. The observation of an ultrafast exponential decay constant of 110 +/- 30 fs in the Adenine-H_2O cluster ion signals was interpreted as being indicative of the participation of the repulsive $\pi\sigma^*$ surface, resulting in H loss or population of the vibrationally hot ground state. This assignment was made due to the calculated strong stabilization of the $\pi\sigma^*$ surface by the solvating H_2O.

Using MPI techniques in 2007 and 2008 Nam *et al.*[61-62] found that protonated adenine-water clusters proceeded to dissociation following proton transfer. They also found that the efficiency of proton transfer was closely related to the ionisation wavelengths employed. Single photon ionisation studies by Belau *et al.* measured the appearance energies for small clusters of the four DNA bases with water[63]. A general trend was found that higher clusters had slightly lower appearance energies.

1.7.4.2 In Solution

Zewail and co-workers, examined 2-aminopurine dissolved in water and ethanol[64] as a probe for studying the excited state decay of the solvated DNA bases. In water the decay of the fluorescence signal was seen to be ultrafast, described by two time constants, 200 fs and 870 fs. It was noted that in the less polar solvent (ethanol) the decay occurred over a much longer time period (16 ps).

Femtosecond fluorescence up-conversion spectroscopy experiments by Pancur _et al._[65] on aqueous N^9-H adenine, N^7-H adenine and adenosine (ribose moiety at the N^9 co-ordinate) were completed in 2005 to investigate the observed dynamics in solution. The work clearly showed, in the N^9-H tautomer, an inverse relationship between excitation energy and fluorescence decay time. The decrease in the lifetime of the N^9-H tautomer at excitation wavelengths of 265 nm and below was interpreted as due to the $\pi\sigma^*$ surface. The observed dynamics for the two other species was consistent with the $\pi\pi^*$/$n\pi^*$/S_0 IC mechanism.

Linear-response free energy calculations by Yamazaki and Kato[66] examined the PES of adenine with regards to the N^9-H co-ordinate to determine the dynamical relaxation pathways responsible in a polar solvent. This study suggested that the vibronic coupling between the two $\pi\pi^*$ surfaces is largely responsible for relaxation. The involvement of the $n\pi^*$ surface was also shown to be reduced, as the separation between this and the prepared $\pi\pi^*$ surface

increased. The barrier height for πσ* surface decay also increased, suggesting that in solution the involvement of this directly dissociative pathway is less favourable than in the gas phase.

Studies on 6-dimethylaminopurine[67] revealed very different decay dynamics in solution than adenine itself. Fluorescence up-conversion measurements suggested that fast conversion from a locally excited state to an intramolecular charge transfer (ICT) state occurred in only ≈ 650 fs. By exchanging the water solvent for dioxane they successfully eliminated this IC mechanism.

1.7.5. Other Bases

Although adenine is the most extensively studied of the DNA bases, there is also a growing body of research related to thymine, guanine and cytosine.

The photodissociation of thymine was studied by Schneider *et al.*[68]. Using velocity map ion imaging (VMI) and Doppler profile measurements, they observed translational energy distribution over the resonantly ionised H (1+1') which was consistent with a statistical IC dissociation ($\pi\pi^*/n\pi^*/S_0$) mechanism through the S_0 surface following excitation over a range of wavelengths ranging from 230 nm to 270 nm. This suggested no participation of the πσ* surface. Further evidence of this $\pi\pi^*/n\pi^*/S_0$ IC mechanism was observed in thymidine, and thymine oligomers by Kwok *et al.*[69], although it is worth noting that in thymidine and thymine oligonucleotides, the heteroaromatic co-ordinate is bonded to ribose (rather than H), essentially eliminating H via the πσ* surface.

Combined theory and TR-MS experiments by González-Vázquez and co-workers[70] examining thymine and microsolvated thymine clusters also failed to identify any participation of the $\pi\sigma^*$ surface in the observed dynamics. From the measured parent transient, two decay components were extracted corresponding to 100 fs and 7 ps, attributed to population via IC of the $n\pi^*$ surface and S_0 respectively.

Recent surface hopping calculations by Asturiol *et al.*[71] have predicted that this $\pi\pi^*/n\pi^*/S_0$ IC mechanism should occur in under 1 ps. They also suggest that a CI between the initially prepared $\pi\pi^*$ and S_0 will also contribute to the observed dynamics. Similar results were obtained by Serrano-Andrés and co-workers[72] when simulating guanine dynamics.

1.7.6 Base Pairs

Of more biological significance than the isolated DNA base, is the understanding of the relaxation processes active in DNA base pairs (guanine-cytosine and adenine-thymine (adenine-uracil in RNA)).

Woutersen and Cristalli[73] examined the effect of hydrogen bonding between the adenine-uracil Watson-Crick base pair, and its effect on the dissipation of energy following vibrational excitation (no electronic excitation). Within isolated uracil, they found that following excitation of the N-H stretching mode, the relaxation proceeds via an intermediate state, before proceeding to lose vibrational excitation in 1.1 ps. In the Watson-Crick base pair, a similar two step

relaxation process was observed, but examination of the transient absorption spectra identified the intermediate state as being different in the monomeric uracil and base-pair. The relaxation of the adenine-uracil base-pair was measured as occurring in 340 fs, significantly faster than in the isolated base. This more efficient relaxation was attributed to the populated N-H stretching mode transferring some of this energy to the hydrogen bonding between the bases. An example of hydrogen bonding is shown in **Figure 1.11** between adenine and thymine.
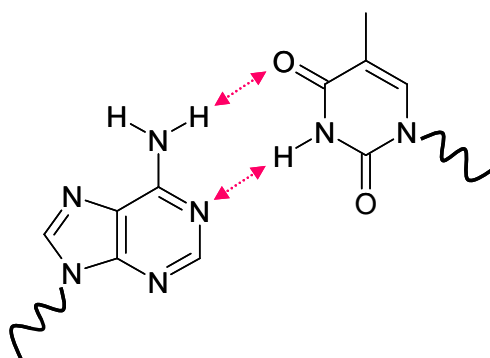
Figure 1.11, an example of hydrogen bonding between adenine and thymine in Watson-crick configuration. Red double headed arrows clearly show the involvement of the hetero atom co-ordinates in DNA structure. Bonds leading to sugar phosphate backbone shown in bold.

Schultz and co-workers[74] examined 2-aminopyridine dimers (examining the electronically excited states) using TR-MS and computational methods. Comparing the decay observed in the dimer to 3 and 4 membered clusters, a faster decay of 65 +/- 10 ps was observed for the dimer compared to 1.5 ns decays for the other species. The faster process was attributed to proton transfer between the model bases through a charge transfer surface of $\pi\pi^*$ character which had CI's with both the initially prepared $\pi\pi^*$ surface and S_0. Through TR-MS measurements of the adenine-thymine base pair[75], these authors also observed an ultrafast relaxation channel through the $\pi\pi^*$ and $n\pi^*$

surfaces of one of the bases within the dimer, in addition to a slower process (40 ps) was observed which was interpreted as possible evidence of a H-transfer process between the bases. Earlier studies[76] also examining adenine-thymine pairs, gave a characteristic timescale of 100 fs for passage from the $\pi\pi^*$ to the $n\pi^*$, followed by relaxation to the ground state in 2.4 ps. No evidence of proton transfer was observed in these adenine-thymine pairs. Lack of this process was also noted in electron-ion coincidence measurements[77], although this study did allow positive identification of the $\pi\pi^*$ and $n\pi^*$ nature of the excited surfaces involved in the dynamics. It is clear from these conflicting conclusions that the presence of a proton transfer mechanism is far from conclusively proven.

1.7.7 Larger Structures

Studies on nucleotides, single-stranded oligonucleotides and double stranded oligonucleotides began in recent years in the condensed phase using a variety of techniques.

Single and double stranded adenine-thymine oligonucleotides were studied by Crespo-Hernández *et al.*[78-79] using fs transient absorption spectroscopy. They found relaxation of isolated bases occurring on much faster timescales (<1 ps) than in the larger oligonucleotide structures. The very similar relaxation time-scales ($\approx$ 125-150 ps) observed in isolated single and double stranded oligonucleotides led to the conclusion that base stacking within the strand, rather than base-pair formation, was facilitating relaxation.

Further evidence of the involvement of base stacking on the relaxation dynamics was observed by Kwok *et al.*[80]. Using a time-resolved fluorescence technique, distinct differences were observed in the relaxation dynamics between adenosine and a single stranded adenine oligonucleotide. In a DNA base monomer, relaxation from the initially prepared $\pi\pi^*$ to S_0 was measured to occur in $\approx$ 2.5 ps. Analysis of the fluorescence profiles eliminated the involvement of the $n\pi^*$ and $\pi\sigma^*$ surfaces in the observed dynamics. Relaxation in the oligonucleotide strand was measured as occurring in $\approx$ 22 ps, passing through two weakly emitting excimer states. The actual transfer from the initially localised excitation to the delocalised excimer state was concluded as being mediated through base-stacking.

Schwalb and Temps[81], using time-resolved fluorescence spectroscopy, further extended this picture. These authors showed that base sequence and indeed higher order structures formed by the oligonucleotides are heavily implicated in the relaxation dynamics and timescales observed. In short, their results point towards the multicomponent nature of photoresistivity when one moves from the micro to the macro level.

1.8 Models for Adenine

The wealth of dynamics studies in these species (e.g. adenine) often come to conflicting conclusions regarding the involvement of particular mechanisms and the relevant PES's. To help gain an understanding of the complex interplay

between these surfaces, and to clarify the multiple relaxation pathways that may or may not be involved, smaller model species have been studied.

1.8.1 Five Membered Ring Models

Imidazole is the structural analogue of the 5-membered ring component in adenine, and as such is an ideal simple polyatomic molecule for indirect study of the N^9-H co-ordinate within the DNA base. As such work has been performed on imidazole, and analogues there-of to build a better understanding of the dynamical processes in action following optical excitation of adenine.

1.8.1.1 Pyrrole

There is a considerable lack of dynamical studies in imidazole in the literature given its relevance with regard to adenine. Pyrrole is structurally extremely similar to imidazole, and has been the subject of several studies, and as such is an ideal species for comparison. The structures of pyrrole and imidazole are shown in **Figure 1.12** as too is adenine for comparison.
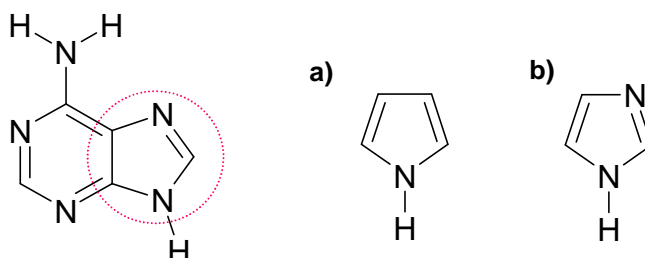
Figure 1.12, a) pyrrole and b) imidazole. 5-membered ring highlighted on adenine.

Sobolewski and Domcke's[82] calculated surfaces, shown in **Figure 1.13**, clearly suggest the presence of a dissociative πσ* surface in pyrrole, such as

expected in adenine. Combined theoretical and experimental findings also imply that H-transfer processes (speculatively observed in nucleic acid base pairs, as discussed earlier) between model chromophore systems, such as pyrrole, via πσ* surfaces are indeed active[83].
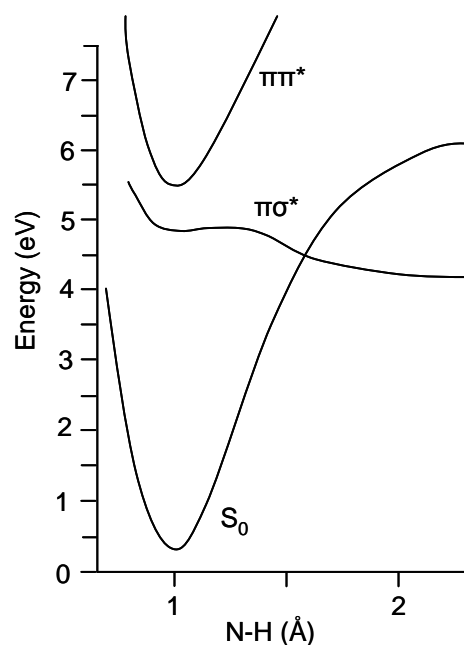
Figure 1.13, schematic representation of the PES's of pyrrole, which are extremely similar to those of imidazole. Adapted from reference 82

Other relaxation pathways following photoexcitation involve ring distortion, and breaking of the ring structure itself[84-86] (at the N-C co-ordinate) have been identified by Barbatti and Lischka. These dynamical simulations show that these pathways should compete effectively with the H elimination mechanism via the πσ* surface with respect to the heteroatom co-ordinate. Blank *et al.*[87] also extensively studied the photodissociation of pyrrole. They observed fragmentation channels which yielded photoproducts which were consistent with the pathways later suggested by Barbatti and Lischka.

Velocity map ion imaging experiments were completed by the Temps group[88-89], resonantly ionising the H fragment with a 2+1 REMPI mechanism. The results clearly implicated coupling of the ππ* and πσ* surfaces, resulting in ultrafast H elimination, in line with the repulsive nature of the πσ* surface.

H-Rydberg tagging experiments by Cronin *et al.*[90] observed the coupling between the ππ* and πσ* surfaces, but noted that, as the level of optical excitation increased, the relative participation of this pathway reduced. This was attributed to an ππ*→nπ*→S_0 IC mechanism, similar to that observed in adenine. Using TR-MS Lippert *et al.*[91] also observed two pathways following excitation at 250 nm and was the very first time-resolved study detecting the H photoproduct. They measured dissociation via the πσ* as occurring in only 100 fs. They also measured a slower pathway occurring in 1.1 +/- 0.5 ps, which was attributed to a slower IC mechanism. It is worth noting that at this excitation wavelength, there is insufficient energy to populate the ππ* surface, leading to direct excitation of the πσ* state.

Very recent results by Beames *et al.*[92] saw no evidence of a 1+1 REMPI signal via the ππ* surfaces, strongly suggesting very efficient ultrafast depopulation of these PES through the πσ* PESs. The 2,5-dimethylpyrrole derivative was also studied, and a 1+1 REMPI signal via one of the ππ* surfaces was seen. This finding clearly shows the sensitivity of electronic excited state behaviour in these heteroaromatic systems to relatively minor adjustments in structure.

1.8.1.2 Imidazole

H-Rydberg tagging experiments by Devine *et al.*[93] on imidazole resulted in similar results to their pyrrole data. These measurements once again displayed a reduction in the contribution of the "fast" H pathway as the optical excitation increased.

Further dynamical simulations by Barbatti and Lischka[94] in imidazole, again suggest the involvement of a ring puckering and ring opening mechanism at the N-C co-ordinate, as suggested by their pyrrole simulations. To date, no experimental efforts to study these mechanisms have yet been made.

1.8.2 Ammonia

Perhaps the simplest model for the heteroatom co-ordinates in adenine is ammonia. The non-adiabatic dynamics exhibited by ammonia have been extensively studied, making this an ideal system to investigate as we build in molecular complexity to imidazole and then to adenine, which is the central theme of this thesis.

1.8.2.1 Linewidth Measurements

The UV absorption spectroscopy of ammonia has been studied extensively[95]. Using line-width measurements, Vaida *et al.*[96-97] noted the dominance of the v_2' absorption progression in the first electronically excited state (umbrella

vibrational mode), observing lifetimes for these states ranging between 117 fs ($v_2' = 2$) to only 38 fs ($v_2' = 14$). These results suggested the $\tilde{A}^1A_2''$ PES (first electronically excited singlet state) was directly dissociating following UV excitation. Similar line-width measurements were made by Ziegler[98-99], with lifetimes ranging from 118 fs ($v_2' = 0$) to 21 fs ($v_2' = 6$). Later absorption studies by Nakajima et $al.$[100] showed that as the degree of deuteration increased, the timescales for dissociation decreased.

The $\tilde{A}^1A_2''$ surface was further experimentally studied by Henck et $al.$[101-102] using microwave-optical double resonance measurements. Increasing dissociation rates for excitation above the $v_2' = 1$ mode were attributed to coupling of this bending mode into one of the N-H co-ordinates, ultimately leading to dissociation. Further evidence of the v_2' progression was seen by Xie et $al.$[103] using REMPI photoelectron spectroscopy. Resonances in the intermediate $\tilde{A}^1A_2''$ state corresponding to the $v_2' = 0$, 1 and 3 were detected.

1.8.2.2 Theoretical Studies

Vaida and co-workers[104] calculated the absorption and emission spectra of NH_3 and ND_3 at the CASSCF level. Good agreement was found between the experimentally observed transition moments and calculated values. It was observed that only small intensity transitions into the symmetric vibrational mode (v_1') on the $\tilde{A}^1A_2''$ surface were found, accounting for the lack of this progression in the absorption measurements. Seideman[105] used these surfaces, and corresponding transition moments to model the photodissociation

dynamics. Qualitative trends for the dissociation timescales for the v_2' progression were reported that matched the experimentally reported values, but quantitatively the lifetimes ($\approx$ 0.97 ps to $\approx$ 2.7 ps) were significantly different from experimentally measured line-width measurements. Seideman also noted the photoproduct angular distribution was dependant upon the internal states populated in the products, and that following photodissociation a mixture of product angular distributions should be observed. Seideman noted that the accuracy of these calculations was limited by the quality of the PES's that were available. Soon after, Kuntz and co-workers[106] published the PES of ammonia, with the study of the photodissociation dynamics in mind.

Dixon[107] progressed this further. By including the bending within the NH_2 co-fragment (v_2), many of the issues seen in the literature with regard to this process were reduced. Dixon also developed an impact parameter model which enabled the calculation of an anisotropy parameter for dissociation into different NH_2 product quantum states. In association with Hancock[108], Dixon later refined this model. This work identified the CI between $\tilde{A}^1A_2''$ state and $\tilde{X}^1A_1$ surface (ground state) as being of great importance in defining the outbound trajectory of the H photoproduct. Yarkony[109] further highlighted the role played by CI's in this photodissociation process.

Marquardt et $al.$[110] calculated the ground state PES of NH_3 using an analytical 6-dimensional representation. The qualitative accuracy of this surface was maintained at large inter-nuclear separations, making it ideal for studies into this photodissociation process. Truhlar and co-workers.[111], shortly afterwards

employed a multi-reference method and single reference method to simulate the ground and first excited state and found good agreement between the two.

Truhlar later employed these surfaces to perform trajectory calculations, in doing so the surfaces were found to be non-representative in certain regions. This stimulated Truhlar to develop new diabatic surfaces[112], depicted in **Figure 1.14**. Truhlar subsequently published two studies that probed the dissociation dynamics of ammonia following population of specific vibrational modes of the excited state. The first of these studies[113] examined dissociation following population of the umbrella bending mode ($v_2' = 0$-6) in the A-state. The results suggested that the dissociation proceeds non-adiabatically, resulting in ground state NH_2, with the remaining energy being accounted for as kinetic energy imparted (mainly) onto the H product. Similar results were obtained in the second study[114], where dissociation from the symmetric stretch and anti-symmetric stretch (v_1' and v_3' respectively), clearly showed that as excitation energy increased, the relative yield of adiabatic dissociation (leading to electronically excited NH_2) increased, independently of which of the two vibrational modes was populated.
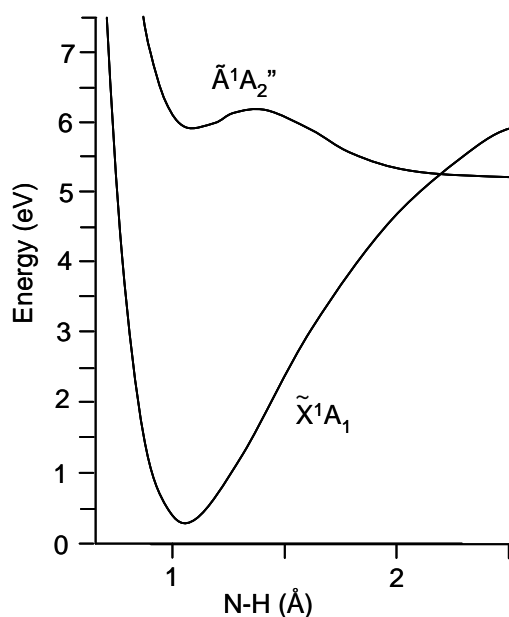
Figure 1.14, Schematic representing the PES of NH$_3$, adapted from reference 111.

Lai *et al.*[115] also used these surfaces[112] to simulate the absorption spectra of NH$_3$. The simulation predicted lifetimes between 13 fs (v_2'= 5) and 314 fs (v_2'= 12), in fairly good qualitative agreement with experimentally observed values in the frequency domain[96-99].

1.8.2.3 Photodissociation Studies

Initial attempts to study the Ã^{1}A$_2$" surface in the frequency domain with rotational resolution were limited due to the fast dissociation following population of this state. Xie *et al.*[116] developed an ion dip technique to probe the Ã^{1}A$_2$" surface after internal conversion from a higher lying surface.

Biesner *et al.*[117-118] were able to determine the distribution of different populated states in the NH$_2$ fragment using TKER. In these experiments different quanta of excitation were deposited into the v_2' mode of the Ã^{1}A$_2$"

state and the dissociation was allowed to proceed, after which the kinetic energy deposited on the H products was detected. From this the internal energies of the partner NH_2 fragments were deduced. It was noted that the adiabatic dissociation channel was accessible at excitation energies in excess of 6.02 eV, and indeed this channel contributed strongly to the observed H signal. In the very high kinetic energy regions of the signal (where only non-adiabatic dissociation is energetically feasible) fine structure was reported. This clearly showed that the corresponding ground state NH_2 fragments were preferentially formed with excitation deposited into the v_2 mode (bending mode), with a wide range of different rotational states also populated. Although Truhlars[113] dynamics simulations qualitatively reproduced the observed kinetic energy profiles observed from the H products, there was still a significant difference between experiment and theory.

Later work within the same group.[119-120] used the same technique to investigate the anisotropy in the H photoproduct as a function of NH_2 quantum states. They found that photoproducts with little rotational excitation were preferentially detected perpendicular to the transition dipole moment (β_2 = -1), whilst photoproducts formed with large amounts of rotational excitation were observed parallel to the transition dipole moment (β_2 = +2). These results helped Dixon to develop his impact parameter model[107], which was later used to simulate the observed angular dependence of the product recoil as a function of NH_2 quantum states[121].

The rovibrational state distribution of NH_2 formed in the first electronically excited state ($\tilde{A}^1A_2$) was examined following dissociation of ammonia at 193.3 nm by Leone and co-workers[122-123], using time-resolved Fourier transform infrared emission spectroscopy. The majority of the observed emission was found to be from the vibrationless ($v_2 = 0$) state, but some contribution was observed from the $v_2 = 1$ and $v_2 = 2$ state. It is worth noting that the excess energy available following adiabatic dissociation is only ≈ 3200 cm^{-1}. Yamasaki et al.[124] investigated the vibrational energy distribution of NH_2 in the $\tilde{X}^2B_1$ state (ground state) following dissociation of ammonia at 193.3 nm, using laser induced fluorescence. They found that the $\tilde{X}^2B_1$ state was predominantly formed with various quanta of vibrational excitation in the v_2 mode, although some $v_1 = 1$ mode excitation was also detected.

Vibrationally mediated experiments by Crim and co-workers[125-130], employing a variety of different detection techniques, have shown great promise. In these experiments, a vibrational band of the $\tilde{X}^1A_1$ state of ammonia is populated, before electronic excitation. The observed relative yield of adiabatic vs. non-adiabatic dissociation was shown to be sensitive to the intermediate vibrational state populated in the electronic ground state. Care was taken to ensure that the total excitation (sum of vibrational excitation and electronic excitation) was equal in all cases compared. The observed differences were attributed to the different Franck-Condon factors for the electronic excitation step, essentially accessing different regions of the excited state PES. Experiments by Akagi et al. [131], specifically evaluating the $\tilde{F}$ranck-Condon factors from two different vibrational states of the $\tilde{X}^1A_1$ surface, quantified the difference in Franck-

Condon factors for the $v_1 = 4$, $v_3 = 1$ combination band and $v_1 = 5$ band (of the A-state) by both time-dependant wavepacket calculations and experiment. Differences between the results were rationalised as being to due to interactions of different vibrational states and by different quantum yields of N-H bond fission.

Using a time-resolved REMPI-PES technique, Liu *et al.*[132] studied the dissociation dynamics of the $\tilde{E}'^1A_1'$ Rydberg state of ammonia. The recorded transient spectra for each transition (in the v_1 series) showed biexponential decays, with all measured time-constants being in the range $\tau_1 < 185$ fs and $\tau_2 < 1348$ fs, with and average value of $\tau_1 = 59$ fs and $\tau_2 = 622$ fs. Previous TR-MS measurements made by Yin *et al.*[133] agreed fairly well with these values ($\tau_1 = 60$ +/- 4 fs, $\tau_2 = 936$ +/- 92 fs). They accounted for the ultrafast decay component as being due to IC to the $\tilde{A}^1A_2''$ surface, the lifetime of which was measured as 51 +/- 4 fs. The long time scales were assigned as dissociation time-constants from the initially excited Rydberg state.

1.8.2.4 The Amino Photoproduct

Following adiabatic dissociation, where the NH_2 product is left in the $\tilde{A}^1A_2$ state, radiative relaxation (fluorescence) has been measured as occurring over the microsecond timescale[134]. Both calculations[135] and experiments[136] have since explored the ground and first electronically excited surfaces of NH_2.

_____

1.8.2.5 NH$_3$ - A Model for Hydrogen Transfer Mechanisms?

Hertel and co-workers[137] used TR-MS to examine the lifetimes of ammonia clusters following excitation at 155 nm, populating a mixture of the B^{1}E$\tilde{''}$ and C^{1}A$_1$' states (accessed at 7.43 eV and 7.91 eV respectively). They found that the monomer decayed in 7.7 ps, significantly longer than the measured lifetimes of the Ã^{1}A$_2$" state. The extended timescale was rationalised as due to IC to the Ã^{1}A$_2$" state, followed by dissociation. They were unable to resolve the lifetimes of the (NH$_3$)$_n$ clusters due to a lack of time-resolution, but they noted all clusters were protonated. They were able to measure the lifetimes of the (ND$_3$)$_n$ series of clusters (n = 1 to 5) which showed a decreasing lifetime with increasing cluster size (τ = 570 fs to τ = 400 fs). These clusters were also protonated, suggesting that the clusters were formed via break-up of n+1 clusters, following H transfer. Hertel[138-139] later employed TR-PES to examine NH$_3$ clusters. In these experiments, the clusters were excited at 208 nm (populating the Ã^{1}A$_2$" state). After examining the dimer, it was seen that the H transfer state had a lifetime of only 130 +/- 60 fs. In comparison, the H transfer state for the trimer was measured as 2.7 +/- 0.6 ps, the longer timescale attributed to a slow IC process. A later study by the same group[139] found that for larger cluster sizes, the lifetime of this transfer state decreased. Similar studies have also been conducted by this group in other clusters[140].

_____

1.9 Summary

The photodissociation of adenine, with respect to the heteroatom co-ordinates, is still a matter of some debate. This body of work aims to address this by: (a) studying the photodissociation of the simplest model system of the heteroatom co-ordinate ammonia, (b) studying the photodissociation of imidazole, which is a model system for the five membered ring in adenine and (c) by applying the knowledge gained from the studies above to look at the photodissociation of adenine itself.

2. Experimental

2.1. Basic Pump-probe Arrangement

A commercially available regenerative amplifier Ti:Al$_2$O$_3$ (Ti:Sapph) system (Spectra-Physics, Spitfire Pro XP) was used to generate 800 nm laser pulses of 35 fs temporal duration at a 1 kHz repetition rate (optical bandwidth of 630 cm^{-1}). A simplified (for clarity) optical lay-out is illustrated in **Figure 2.1**. Particular aspects of the setup will be expanded upon in the proceeding sections.
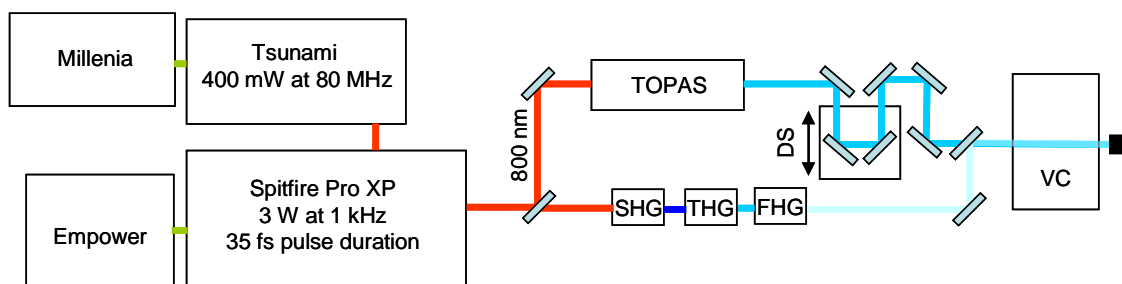
Figure 2.1, simplified optical arrangement. DS is motorised delay stage, axis of motion shown. VC is the vacuum chamber. SHG, THG and FHG are the second, third and fourth harmonic generating crystals. TOPAS is an optical parametric amplifier.

A Kerr-lens mode-locked Ti:Al$_2$O$_3$ oscillator (Tsunami) produces an 800 nm, 80 MHz pulse train with pulse energies of 5 nJ/pulse. For gas phase multiphoton excitation experiments, these pulses are insufficient in energy. To amplify these pulses to an acceptable energy, they are amplified (1 in every 80000) through a regenerative amplifier unit (Spitfire Pro XP), resulting in pulse energies of approximately 3 mJ/pulse, i.e., a gain of 6 x 10^5.

The output beam from the regenerative amplifier is divided into three beams using beam-splitters. Two thirds of this output is used to pump two separate optical parametric amplifiers (TOPAS, Light Conversion) equally, one is set-up to produce UV radiation the other infrared, which is not utilised in these experiments. The UV output acts as probe in the experiments described and is typically set at 243.1 nm, to resonantly ionise H photoproducts through a 2 + 1 REMPI mechanism, as shown in **Figure 2.2**.

The remainder of the laser output is diverted through a series of non-linear optical crystals to generate the second, third and fourth harmonics. Both the fourth harmonic (200 nm) and third harmonic (266 nm) have been used as optical pumps in the experiments performed.
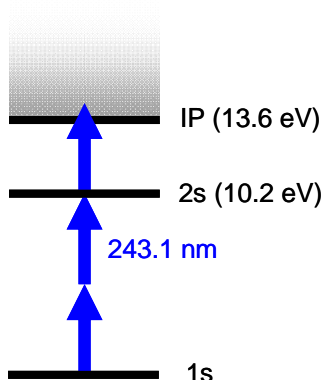
Figure 2.2, 2 + 1 REMPI mechanism, to ionise neutral H through the intermediate 2s state.

The probe beam (243.1 nm) is passed over a motorised delay stage, which accurately alters the optical path length the probe beam traverses (and hence controls the temporal delay between the two pulses). A delay stage movement of 1 μm corresponds to an optical delay of ≈ 6.7 fs.

Both beams are focussed through separate 500 mm focal length lenses prior to entering the chamber. The probe beam output from the OPA is 3 mm in diameter. To enable tight focussing and hence higher intensities (since probing of the H is a three photon process) this diameter is increased to 8 mm using a Galilean telescope. Equation 2.1 where d_F is the beam diameter at the focal length, λ is the laser wavelength, F is the focal length and d_i is the beam diameter at the lens clearly shows that the beam diameter at the focus is inversely proportional to initial beam diameter. The pump beam is focused to a diameter of $\approx$ 18 μm with an area of $\approx$ 254 μm^2 and the probe to $\approx$ 19 μm and an area of $\approx$ 290 μm^2.

$$d_F = \frac{4 \cdot \lambda \cdot F}{\pi \cdot d_i} \qquad (2.1)$$

The corresponding power densities for the 200 nm and 243 nm pulses are $\approx 6.6 \times 10^{12}$ Wcm^{-2} and $\approx 2.3 \times 10^{13}$ Wcm^{-2} respectively. These values have been calculated using equation 2.2, where I is intensity, P is measured laser power, τ is pulse duration, R_{rep} is the laser repetition rate and A is focal area.

$$I = \frac{P}{\tau \cdot R_{rep} . A} \qquad (2.2)$$

Both beams meet at a dichroic beamsplitter and are diverted by a removable silver mirror and collinearly aligned outside of vacuum through a 50 μm pinhole before the removable optic is taken out to allow the beams to pass into the vacuum chamber through a calcium fluoride window. By measuring the

respective H yield as a function of temporal delay between the two pulses, and subsequent fitting of these transient spectra (to be discussed), allows real time observation and measurement of photodissociation events.

2.1.1 Nonlinear Optical-Mixing

As light passes through a medium, the electric field of the light induces polarization of the electrons in the lattice[141]. This effect can be described by equation 2.3.

$$P = \varepsilon_0 (X^{(1)} E + X^{(2)} E^2 + X^{(3)} E^3 + ...) \qquad (2.3)$$

$$E = E_0 \sin(\omega t) \qquad (2.4)$$

where P is the dielectric polarization of the medium, $X^{(1)}$ is the 1st order susceptibility term, $X^{(2)}$ is the second order term, and so on, these terms describe the response of the electrons in the lattice to an electric field, and ε_0 is the electric permittivity of free space. E is the electric field, as defined by the light wave shown in equation 2.4. Substituting for the electric field into equation 2.3 yields,

$$P = \varepsilon_0 X^{(1)} E_0 \sin(\omega t) + \varepsilon_0 X^{(2)} E_0^2 \sin^2(\omega t) + \varepsilon_0 X^{(3)} E_0^3 \sin^3(\omega t) + ... \quad (2.5)$$

Using the trigonometric identities of the higher order terms yields equation 2.6. Inspection of this result clearly shows the origin of the frequency doubling and

tripling effects observed in birefringent crystals, i.e. the fundamental is up-converted to generate the second and third harmonics 2ω and 3ω respectively.

$$P = \varepsilon_0 X^{(1)} E_0 \sin(\omega t) + \frac{\varepsilon_0 X^{(2)}}{2} E_0^{\,2} (1 - \cos(2\omega t)) + \frac{\varepsilon_0 X^{(3)}}{4} E_0^{\,3} (3\sin(\omega t) - \sin(3\omega t)) + ...$$

(2.6)

At low intensities most optical processes may be understood with reference to the first order susceptibility term, but at higher field strengths the relative participation of higher order terms increases. As a result, these processes grew in popularity with the development of lasers.

In the optical arrangement described above, these higher order processes are exploited to yield UV radiation, more specifically the third and fourth harmonics of the 800 nm fundamental are used as the pump, and by the OPA output as probe. **Table 2.1** lists the polarizations of the harmonics generated in the home-built fourth harmonic generation unit.

Wavelength	Harmonic	Crystal	Polarization
800 nm	Fundamental	-	Ordinary
400 nm	2nd	BBO	Extraordinary
266 nm	3rd	BBO	Ordinary
200 nm	4th	BBO	Extraordinary

Table 2.1, crystals utilised for generation of second, third and fourth harmonics of the 800 nm and their respective polarizations.

2.2 Vacuum Chamber

The species under study is heated and co-expanded with He (typically 2 bar backing pressure) through an Even-Lavie pulsed valve[142] , into a differentially pumped vacuum chamber. Typical operating pressures of $\approx$ 6 x10^{-6} mbar and $\approx$ 3x10^{-7} mbar are routinely achieved in the source and interaction chambers respectively (**Figure 2.3**). The molecular beam is subsequently skimmed, before passing through a series of open-lens electrodes (voltages set to velocity focussing ratio, as described in section 2.5), where it is intercepted by the pump and probe pulses.
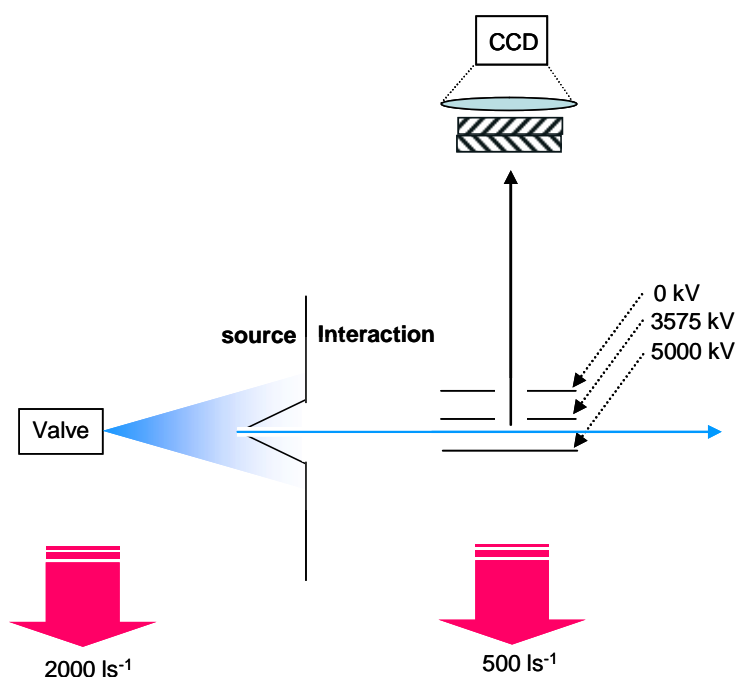
Figure 2.3, schematic of the vacuum chamber arrangement. The collinearly aligned beams intercept the molecular beam (orthogonal to page) between the rep/acc electrodes, which accelerate generated ions through a 500 mm field free drift region towards a position sensitive detector.

2.2.1 Time of Flight Mass Spectrometry

The generated ions are accelerated through a drift region towards a position sensitive detector. The "time of flight" of a particular mass fragment can be described in simple terms by equation 2.7. For more complex electrode configurations, consisting of multiple acceleration regions, flight times can be calculated as shown by Wiley and Mclaren[143].

$$t = \sqrt{\frac{l^2}{V_{acc}^2}} \cdot \sqrt{\frac{m}{z}} \qquad (2.7)$$

$$KE = V_{acc} \cdot z = \frac{1}{2}mv^2 \qquad (2.8)$$

where l is the flight path, V_{acc} is the accelerating voltage, m is the fragment mass and z is the charge. From this relationship it is clear to see that since the same kinetic energy (as shown in equation 2.8) is applied to all fragments (of the same charge) lower mass fragments will traverse the drift region faster than heavier fragments.

At the terminus of the drift region, the generated ions are detected by a 40 mm chevron microchannel plate and fast phosphor screen (decay time ≈ 1.2 ms), which acts as a position sensitive detector, with a CCD camera recording the fluorescence signal of the phosphor screen at the rear of this detector.

This set-up can be used as a Time-Resolved Mass Spectrometer, where current is drawn directly from the phosphor screen and recorded with a home-

built LabVIEW program through an oscilloscope. Alternatively the setup can be switched to Velocity Map Ion imaging (VMI) conditions, where the generated image at the rear of the phosphor screen is recorded by the CCD camera and collected, once again, by a home-built LabVIEW program. VMI will be discussed in more detail shortly.

2.2.2 Molecular Beams

An ensemble of molecules at a given temperature will have a statistical selection of energy levels populated. This population is described by the Boltzmann distribution shown by equation 2.9 where T is temperature, k is the Boltzmann constant, n_i is the number of molecules occupying a particular state i with energy ε_i and N is the total number of molecules across all energies.

$$\frac{n_i}{N} = \frac{e^{-\frac{1}{kT}\varepsilon_i}}{\sum\limits_{i} e^{-\frac{1}{kT}\varepsilon_i}} \qquad (2.9)$$

The simplest way to interpret the impact of such a distribution upon spectroscopic studies is to look at the effects of rotational excitation within an ensemble of molecules relative to the ground state (n_0). The Boltzmann distribution of such an ensemble is given by equation 2.10.

$$\frac{n_j}{n_0} = (2j+1) \cdot e^{-\frac{1}{kT}\varepsilon_j} \qquad (2.10)$$

where j is rotational quantum number. The $(2j+1)$ term is required to deal with the degeneracy of the rotational states. By repeating this calculation over a series of different temperatures, as shown in **Figure 2.4**, where the first few populated rotational states of the $v_2 = 0$ (bending) mode of NH_2 are shown as a function of temperature, it becomes clear how the distribution of populated rotational states increases with temperature. Ultimately this serves to complicate all forms of spectroscopy, as the amount of accessible transitions increases as temperature increases, resulting in spectroscopic congestion. It is clear that to observe a pure transition it is necessary to cool the analysed species, to limit the population distribution to the lowest energetic state. To obtain an ensemble of molecules in a uniform low energy (10's of wavenumbers) the use of supersonic expansions has become common.
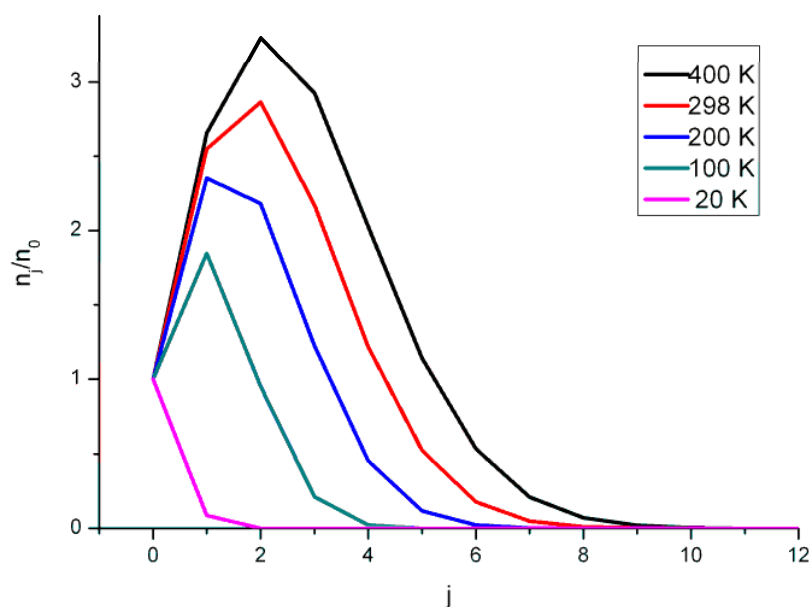
Figure 2.4, Boltzmann distribution of populated rotational states in the $v_2 = 0$ and of NH_2 (X-state), term values taken from reference 117. As temperature drops the statistical distribution of populated states reduces.

A supersonic expansion occurs when a high pressure gas is allowed to expand through an orifice/nozzle[144] to a region of low pressure, where the random motion of the molecules in the gas is converted into translational motion, effectively converting the random thermal motion into directed flow in the expanding gas. This results in cooling of the translational motion of molecules relative to each other. Cooling of rotational and vibrational modes is achieved through collisions in the molecular beam with the seed gas (more precisely, in the early stages of the molecular beam, since collision events are proportional to the ratio between nozzle diameter and distance downstream[145]).

One of the limiting factors of utilising supersonic expansions is the high gas through-put into a vacuum. This problem has been overcome, to a degree by operating pulsed valves[146] which reduce the load upon the pumping systems. Assuming a valve operates at 1 kHz with a 10 µs opening time, the gas load is only 1/100th of an equivalent non-pulsed valve.

2.3 Instrument Response Function and Time Zero

Temporal resolution is limited by the cross correlation of the pump and probe pulses. To determine this "instrument response function" non-resonant ionisation is used to measure the ion signal as a function of the temporal overlap of the two pulses. This also determines time zero, i.e. the temporal delay between the two pulses is zero.

Non-resonant ionisation is sensitive to time zero, since the highest ion signal is expected at the temporal delay where the highest photon density is achieved, that is temporal overlap. Non-resonant ionisation also eliminates the effects of populated states upon the measured cross correlation, which could significantly broaden the instrument response function. The profile of the ion signal obtained is then fitted with a Gaussian function to yield the instrument response function, as shown in **Figure 2.5**.
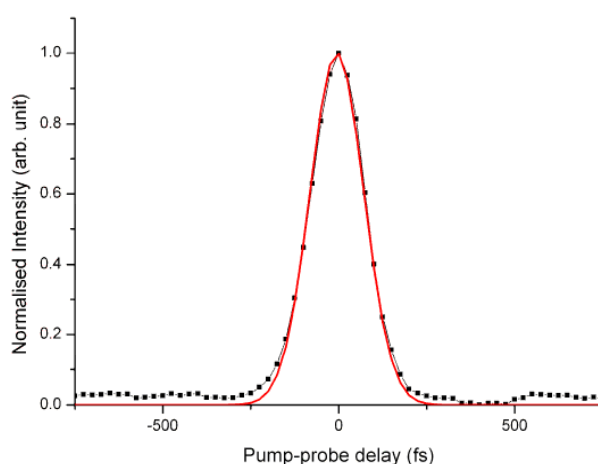
Figure 2.5, cross correlation measurement of ^{129}Xe ion signal as a function of pump probe delay (black); fitted Gaussian yielding an instrument response function of 180 fs also shown (red).

2.4 Fitting of Transient Spectra

The experiments described in this thesis mainly focus on measuring the appearance time of H^+ as a function of time delay between pump and probe laser pulses. The mathematical representation of the photoproduct appearance times is best described by an exponential rise convolved with a Gaussian function.

Mathematica was used to generate an analytical form of the convolution of a exponential rise with a Gaussian function. This function was imported to Origin 7.5^{TM} and used to iteratively optimise fit variables to yield timescales for photoproduct appearance.

$$y = y_0 + \left(A * \left(1 + erf\left(\frac{x - x_0}{B} \right) - \left(\exp\left(\frac{B^2 - (4 * \tau * (x - x_0))}{4 * \tau^2} \right) \right) * \left(1 - erf\left(\frac{\left(B^2 - 2 * \tau * (x - x_0)\right)}{2 * B * \tau} \right) \right) \right) \right)$$

$$\text{where;} \quad B = \frac{G}{\sqrt{4 \ln 2}}$$

(2.11)

Convolution is required, since the laser pulses are not infinitely short in time, effectively "broadening" the observed transient signals as a function of the cross-correlation of the pump and probe pulses. The Gaussian replicates this cross-correlation and the exponential rise is used to model the rise in signal, indicative of a directly formed photodissociation product. This is depicted in equation 2.11 where y_0 is the baseline, A is an amplitude factor, x_0 is the time-zero adjustment, G is the cross correlation of pump and probe pulses and τ is the exponential rise time, i.e. the photo-product appearance time. During the fitting procedure x_0 is allowed to vary between -15 and +15 fs, within the accuracy of experimental x_0 determination to yield the best optimised fits.

2.5 Velocity Map Ion Imaging

VMI was developed from the early ion imaging experiments by Chandler and Houston[147]. In this experiment, CH_3I was dissociated, via the A-band, by a

single photon at 266 nm. The neutral methyl was subsequently ionised through a 2 + 1 REMPI mechanism. This occurred between a repeller electrode and a ground electrode, resulting in the acceleration of the photoproducts towards a position sensitive detector. The resultant image collected from the position sensitive detector was a 2D projection of the 3D distribution of the generated photoproducts, containing the angular dependence of the photoproduct formation and velocity distribution of said products (**Figure 2.6**).
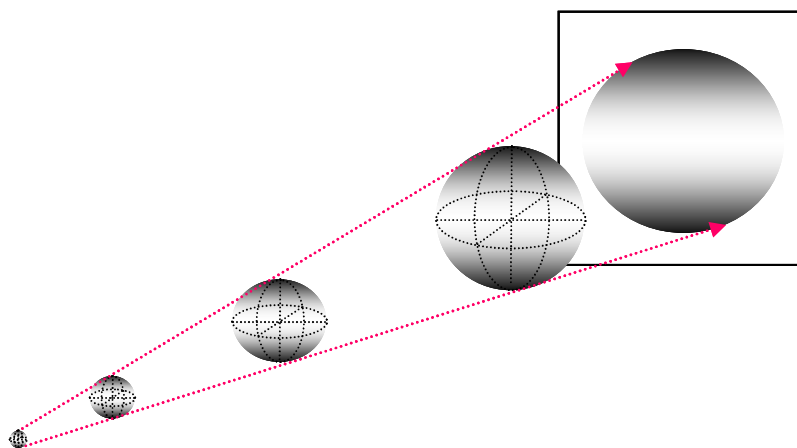
Figure 2.6, expansion of the three dimensional distribution of photoproducts (Newton sphere) prior to projection onto a two dimensional plane (detector).

Eppink and Parker[148] refined these ion imaging experiments by using open lens electrodes. Previously, grids would cover the lenses, essentially reducing ion transmission and causing distortion of ion trajectories. By removing these effects it was now possible to accurately map the initial velocities of the generated photoproducts, i.e., all photoproducts with the same initial velocity are mapped onto the same radius upon the detector. More specifically, all products formed with the same initial velocity vector are focussed upon the same point on the detector.

As the photoproducts are separated by time of flight mass spectrometry, gating the gain of the position sensitive detector, or simply using deflector plates to remove unwanted mass fragments, allows VMI images of individual photoproducts to be detected.

$$KE = \frac{1}{2}mv^2 = \frac{1}{2}m[R/(Nt)]^2 \propto R^2 \qquad (2.12)$$

Equation 2.12 describes the relationship between the mapped velocity (in the plane perpendicular to the time of flight axis) and image radius, R. N is a magnification factor that relates the image radius to velocity, v, and time-of-flight, t, as shown by equation 2.13. The magnification factor is a constant for a given repeller/accelerator voltage.

$$R = Nvt \qquad (2.13)$$

These imaging techniques have been applied to the study of several different chemical systems with great success[149-150].

2.6 Anisotropy

It is well known that non-imaging techniques that measure kinetic energy are able to also measure the angular dependence of photoproduct formation as a function of laser polarization, such as TKER measurements and Doppler spectroscopy[151]. These methods, however, give a one dimensional picture of the measurement of this angular dependence, so to see a full angular

distribution of products, experiments need to be completed over a selection of orientations of light polarization relative to the detector.

With ion imaging methods however, because each two dimensional projection contains the entire three dimensional distribution, this angular dependence can be determined from only one experimental orientation. It is imperative in these experiments that the electric component of the laser light is parallel to the plane of the detector (i.e., cylindrical symmetry), to enable accurate measurement of velocity and spatial anisotropy.

When a dissociation event initiated by absorption of single photon occurs faster than the rotational period of the parent molecule (photoexcitations whose transition dipoles are aligned to the polarization vector of the photon are selectively excited), the generated fragments will retain spatial anisotropy. If the dissociation is slow relative to the rotational period however anisotropy will be lost, as the molecule undergoes rotation prior to dissociation. The mathematical expression describing the spatial anisotropy is given by:

$$I(\theta) = \frac{(1 + \beta P_2(\cos\theta))}{4\pi} \qquad (2.14)$$

P_2 is the second order Legendre polynomial and is given by:

$$P_2(x) = \frac{(3x^2 - 1)}{2} \qquad (2.15)$$

In equation 2.14, I, is the product intensity at a given angle, θ, relative to the polarization vector, and β is the anisotropy parameter.

For multiphoton processes higher order Legendre polynomials are required, but these are beyond the scope of these measurements. Angular distribution may be expressed in terms of a combination of sine and cosine distributions, as illustrated in equation 2.16.

$$I(\theta) = a\sin^2\theta + b\cos^2\theta \qquad (2.16)$$

where a and b are coefficients that describe the relative contributions of sine and cosine distributions respectively. The anisotropy parameter, β, may now be represented by equation 2.17[152].

$$\beta = \frac{2(b-a)}{2a+b} \qquad (2.17)$$
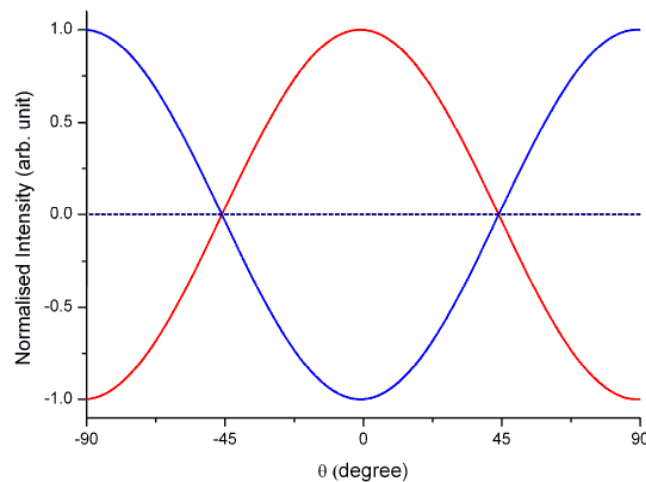
Figure 2.7, normalised intensity (between -1 and 1 for clarity) of product alignment (θ) relative to laser polarization. (Red) parallel process, $\beta_2 = 2$; (blue) perpendicular process, $\beta_2 = -1$; and (dashed line) isotropic process, $\beta_2 = 0$, clearly showing no angular alignment.

Figure 2.7, shows three normalised fragment distributions for a one photon process. Firstly for parallel dissociation (cos^2 distribution) photofragments are formed in line with the transition dipole where $a = 0$, $b = 1$ and $\beta_2 = 2$. Secondly, for perpendicular dissociation (sin^2 distribution) dissociation occurs at 90° to the transition dipole where $a = 1$, $b = 0$ and $\beta_2 = -1$. Finally for an isotropic dissociation, a combination of these two limiting cases results. In this instance, there is no angular dependence from photoproduct formation with coefficients equalling $a = 0.5$, $b = 0.5$ leading to $\beta_2 = 0$.

The anisotropy parameter gives characteristic information regarding the angular distribution of the photo-dissociation process studied, and therefore provides complementary information to accompany the recorded kinetic energy spectrum. This enables further characterisation of the studied processes, and initial states populated, as will become evident in the proceeding chapters.

2.7 Image Processing

The 2D projection is a convolution over all angles of the 3D Newton sphere. The result of this is that at each radius in the 2D projection, interference from signal originating outside of the plane of the detector will be present. This is illustrated by the xz plane in **Figure 2.8.** To obtain a velocity spectrum from this image, it is necessary to take a slice through the sphere ($\alpha = 0$). But this is not directly possible from the image. As such deconvolution of the 2D projection is necessary with respect to α. To achieve this, a polar onion peeling (POP) algorithm is utilised, based upon the work of Roberts *et al.*[153]
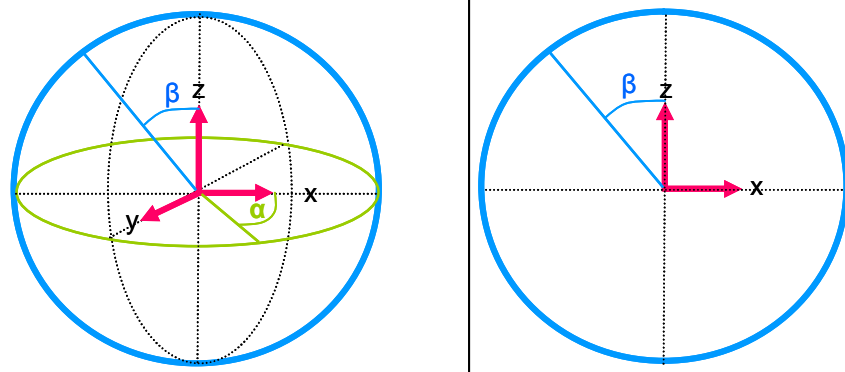
Figure 2.8, projection of a three dimensional Newton sphere onto a two dimensional plane. The two dimensional image will be a convolution over angle α (green). Blue circle corresponds to a particular radius on the plane x-z.

2.8 Time-Resolved Velocity Map Ion Imaging

The coupling of energy resolution (VMI) with time-resolved methodologies was first completed by Whitaker and co-workers[154-155], in which the non-resonant multi-photon dissociative multi-photon ionization of NO_2 was studied. Observation of oscillations in the recorded transients were attributed to the observation of "orbiting" states in which loosely bound O atom and an NO molecule rotated around one-another, in a comparable manner to van der Waals complexes.

More recently, the well studied A-band photodissociation of methyl iodide[156] has been the subject of time-resolved VMI (TR-VMI) studies by de Nalda *et al.*[157-160]. Using this technique, timescales for dissociation into ground state ($^2P_{3/2}$), and spin excited ($^2P_{1/2}$) iodine were measured, as well as dissociation timescales into different vibrational modes of the partner methyl co-fragment.

The combination of kinetic energy resolution with time resolution has enabled timescales for quantum state specific photoproduct formation to be measured. Kinetic energy resolution is ultimately limited by the time-energy uncertainty, but these studies clearly show how separation of different vibrational channels is achievable due to the difference in the KE of the photoproducts.

2.8.1 VMI Simulations and Construction

SIMION 8[TM] determines the electrostatic potential, $V(x,y,z)$, in a charge free region, defined by the variables x, y and z as illustrated by equation 2.18.

$$V(x, y, z) = \sqrt{(x^2 + y^2 + x^2)} \qquad (2.18)$$

Solutions to this satisfy the Laplace equation, shown in equation 2.19, where changes in the variables x, y and z do not result in changes in the potential.

$$\frac{\partial^2 V}{\partial x^2} + \frac{\partial^2 V}{\partial y^2} + \frac{\partial^2 V}{\partial z^2} = 0 \qquad (2.19)$$

Simulations were carried out using SIMION 8[TM] to aid the design and construction of the ion imaging optics. A 3D potential array, based upon the arrangement used by Eppink and Parker[148], consisted of a repeller, extractor and ground electrode. All electrodes were 70 mm in diameter, with the accelerator and ground having 20 mm bore holes to allow for ion transmission. The electrodes were separated by 15 mm. Simulations also included deflector

electrodes (and associated mounts) to be used to gate fragment passage. This enabled selected masses to be imaged on the detector.

Trajectory simulations were completed to predict the required voltages across both repeller and extractor electrodes to achieve VMI focussing conditions. The voltage ratio (for a 500 mm drift region) between repeller (V_R) and accelerator (V_A) was predicted to be 0.702. This value is in close agreement with the value of 0.71 determined by Eppink and Parker[148].
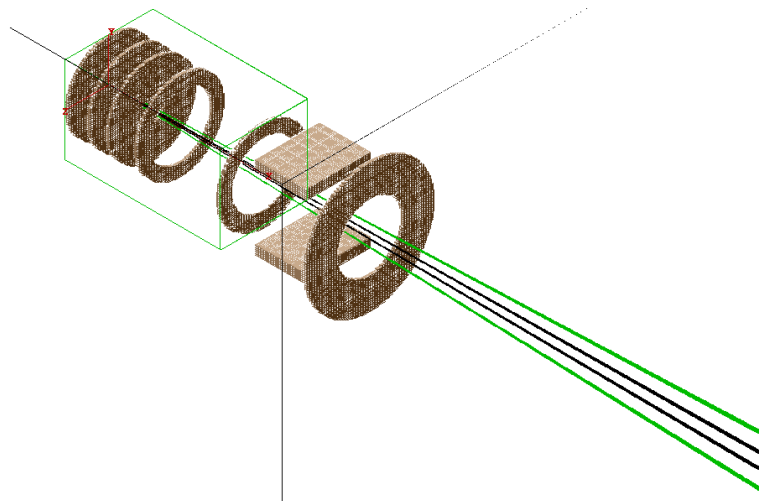
Figure 2.9, SIMION 8^{TM} trajectory simulations showing focus of four populations (with 3D Gaussian distributions) of H$^+$ with different velocity vectors with repeller set to 5000 V and accelerator to 3510 V. Green shows the two populations with 1.1 eV kinetic energy being focussed at the terminus of a 500 mm flight path, whilst black trajectories depict the two populations with 0.1 eV kinetic energy.

The diameter of the Newton sphere is ultimately determined by V_R (since V_A is essentially 0.702 x V_R). Since the detector is only 40 mm in diameter, calculations revealed that setting V_R at 5000 V enables focussing of the whole Newton sphere onto the detector, shown in **Figure 2.9**. The size of the Newton

sphere is ultimately determined by the maximum kinetic energy imposed upon the inspected photo-fragment.

Electrodes were mounted on rods, and separated by spacers made of Al_2O_3 (Kimball Physics). Geometries specified in simulations were used in the early construction. Initial testing revealed stray field-effects altering ion trajectories. These were overcome by augmenting the ground electrode with a copper cylindrical extension and extending the electrode further down the field free region. Complimentary 2D simulations showed no perturbation to the ion trajectories.

2.8.2 VMI Calibration

The recorded images simply give an array of pixels of varying intensity. To calibrate the spectrometer, i.e. to relate the pixel radius to the kinetic energy of the ion, a well studied system, giving distinct kinetic energy products was examined. HBr was identified as an ideal candidate, since both photoproducts formed are atomic in nature, essentially eliminating broadening of their velocity distributions due to population of vibrational and rotational states.

The photodissociation of HBr and indeed HI following population of the A-band has been extensively studied by both theory[161-163] and experiment[164-165]. The dissociation energy (D_0) of HBr has been measured as 30210 cm^{-1} (3.75 eV) experimentally[165], corresponding to dissociation forming H and Br ($^2P_{3/2}$). The splitting between the ground state Br ($^2P_{3/2}$) and spin excited Br ($^2P_{1/2}$) is known

to be 3685 cm^{-1} (0.46 eV). Following excitation at 200 nm, equation 1.14 can be re-written to equate the theoretical kinetic energies observed on the H photoproduct following dissociation into the $^2P_{3/2}$ and $^2P_{1/2}$ Br channels. With the reduced mass taken into account, the theoretical maximum kinetic energies in the H photoproduct are 19546 cm^{-1} and 15906 cm^{-1} for the $^2P_{3/2}$ and $^2P_{1/2}$ channels respectively. Following excitation at 243.1 nm (which also excites the A-band) kinetic energies of 10790 cm^{-1} and 7151 cm^{-1} for these two channels should also be seen. The signal from pumping with 243.1 nm and subsequent probing with 243.1 nm is expected to be small, due to the four photon nature of the overall process.
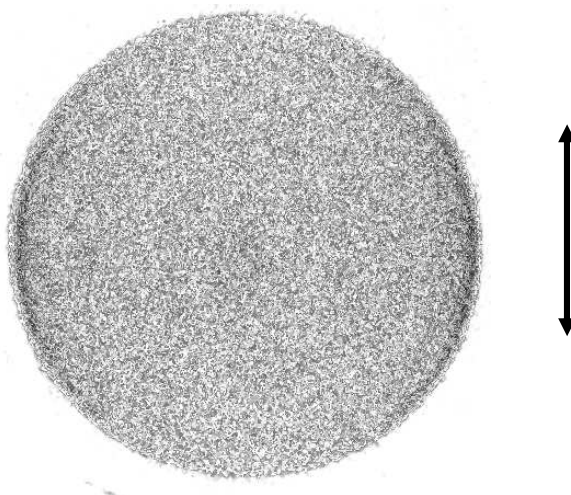
Figure 2.10, raw image of H$^+$ following photodissociation of HBr, with a time delay between pump (200 nm) and probe (243.1 nm) of 2000 fs, enabling the propagated wavepacket to dissociate. Laser polarization shown on right.

Calibration runs were completed, pumping at 200 nm and probing the H at 243.1 nm. An individual image of H from HBr is shown in **Figure 2.10**. It is worth noting that this image is a convolution of the entire Newton sphere, so dissociation events from outside of the plane of the detector ($\alpha \neq 0$) are convolved upon the true mapping of velocity vectors. Ion optic voltages were

manually optimised to $V_A = 5000$ V and $V_R = 3575$ V ($V_A/V_R = 0.715$) to yield the sharpest (and hence best focussed) images.
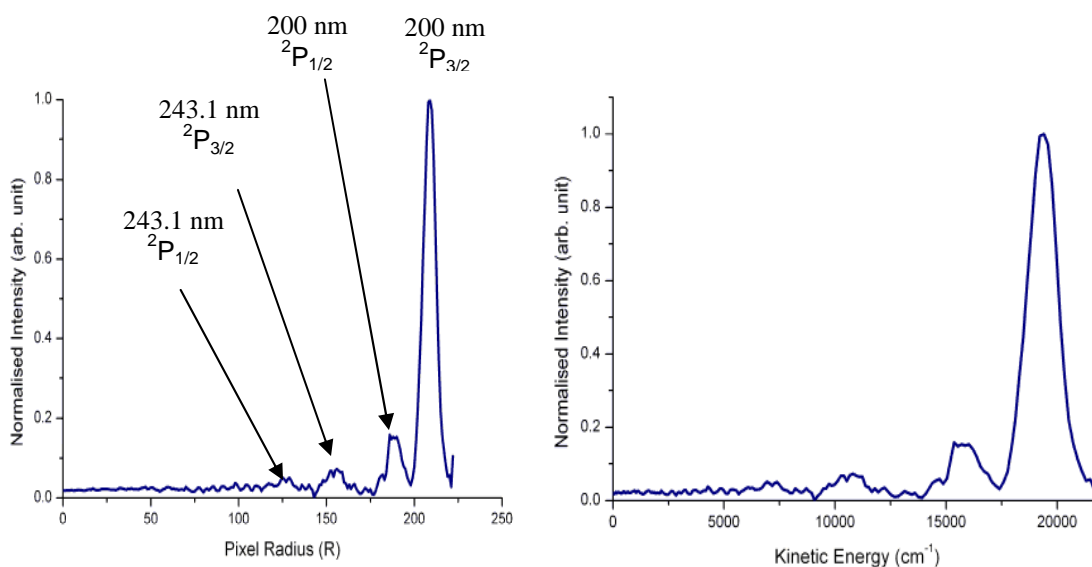
)
H$^+$ signal vs. pixel radius from the photodissociation of HBr. Assignment to different spin state product channels shown. (right) H$^+$ signal vs. kinetic energy after calibration.
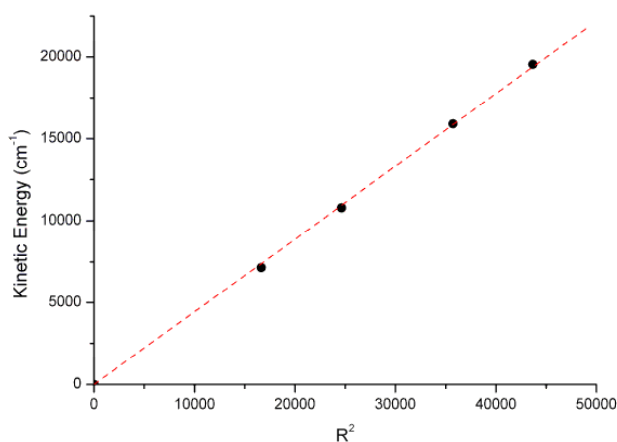
Figure 2.12, plot of kinetic energy vs. pixel radius squared. A calibration factor of 0.4441 is obtained

Processing of the raw image using the POP program[153] yields a deconvoluted plot of intensity vs. pixel radius (R), as shown in **Figure 2.11**. Assignment of these observed maxima to the calculated theoretical maximum kinetic energy values of the photoproducts yields the calibration plot shown in **Figure 2.12**.

The measured anisotropy parameters for dissociation following excitation at 200 nm for the spin excited and ground state Br channels of $\beta_2 = 0$ and $\beta_2 = -1$ respectively match excellently with previous measurements listed in the literature[164]. Due to the small signal from the probe, the anisotropy parameters at this wavelength are less accurate.

Fitting the observed peaks with Gaussian functions (G) of the form illustrated in equation 2.20, where R_0 is the peak maximum reveals the resolution of the VMI set-up to be $\approx 4 \%$ of the pixel radius. The resolution is limited by the optical bandwidth of the laser pulses used in these experiments.

$$G = e^{-(4\ln 2) \cdot \frac{(R-R_0)^2}{(0.04 \cdot R)^2}} \qquad (2.20)$$

2.8.3 TR-VMI of HBr

Integration of the two kinetic energy regions (now separated via VMI) following excitation at 200 nm over a range of different time delays allows the assignment of timescales to these two individual channels, which without the energy resolving ability lent from VMI would not have been possible.

An illustrative example of this is given in **Figure 2.13** which shows the H$^+$ transients for the two dissociation channels. It is clear to see that dissociation into the two distinct product channels occur on different timescales. The appearance time of the $^2P_{3/2}$ product channel is longer than the $^2P_{1/2}$ channel. Physical interpretation of this is difficult, given that the channel with the highest

kinetic energy (lowest level of energy deposited as internal energy of photoproducts) is dissociating slower than the lowest kinetic energy channel.
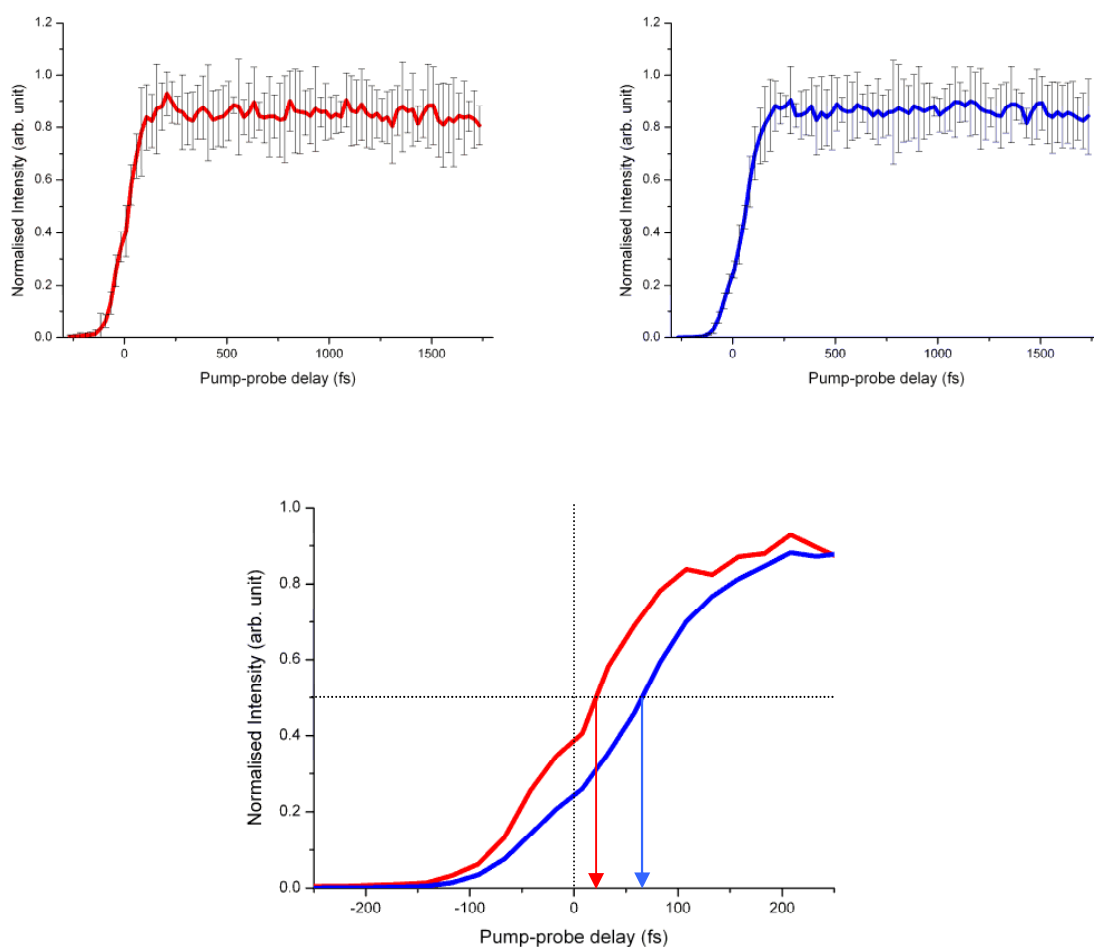
Figure 2.13, (Top) integrated H$^+$ signals for $^2P_{1/2}$ (red) and $^2P_{3/2}$ (blue) Br channels following photodissociation at 200 nm. Error bars shown correspond to a 95 % confidence limit. (Bottom) Comparison of rise times of H$^+$ signals for $^2P_{1/2}$ and $^2P_{3/2}$ channels at 200 nm, displacement of half maxima from τ_0 indicated.

The fitted timescales for dissociation, are both < 50 fs, so confident assignment of these timescale is not possible, due to the short dissociation timescales compared to the cross correlation of the two laser pulses (≈ 170 fs). Although we are unable to assign timescales to these two channels with any confidence, it is very clear that the low KE channel occurs on a faster timescale than the

high KE channel. The reasoning to this is still a matter of debate, and ongoing

calculations with theoretical collaborators aim to clarify this.

3. Ammonia

3.1 Briefing

Ammonia is regarded as an ideal small system for the study of nonadiabatic dynamics. As such extensive experimental[96-99,116-118,121-124] and theoretical[104-114] efforts over the past few decades have investigated the photodissociation dynamics of this molecule. Past literature of particular relevance to the work described herein will be described below. However the reader is referred to the introduction for a more comprehensive description of these efforts. The N-H dissociation in ammonia mimics that of the larger biological molecules, and as such serves as an ideal starting point for the study of heteroatom dissociation in these systems.
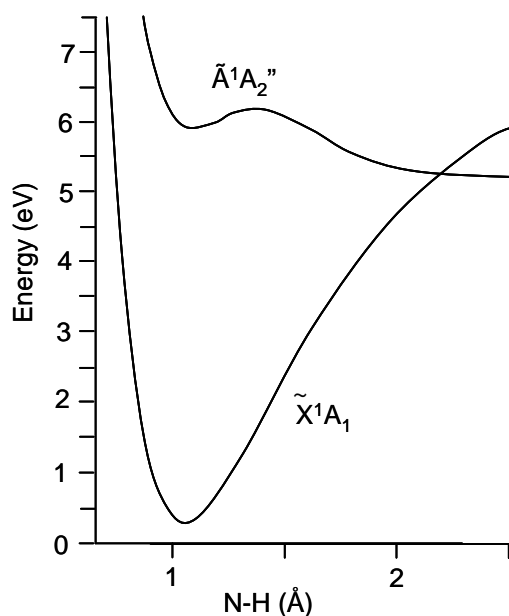
Figure 3.1, schematic representation of the PES's of NH$_3$, adapted from reference 111.

It is known that if total excitation is above 6.02 eV[118] both adiabatic, leading to electronically excited $\tilde{A}^2A_1$ NH_2 and neutral H, and non-adiabatic, leading to ground state $\tilde{X}^2B_1$ NH_2 and neutral H are energetically accessible (PES's of NH_3 shown in **Figure 3.1**). Excitation below 6.02 eV only forms ground state NH_2 ($\tilde{X}^2B_1$) via nonadiabatic dissociation. The excess energy above the dissociation thresholds, for both adiabatic and non-adiabatic dissociation, is conserved in the form of internal energy within the NH_2 fragment and kinetic energy (KE) on both the H and NH_2 co-fragments.

The absorption spectrum is dominated by a progression in the v_2' out of plane vibrational mode (umbrella mode)[97], this is due to the transition from the C_{3v} $\tilde{X}^1A_1$ state to the D_{3h} $\tilde{A}^1A_2''$ PES moving from a pyramidal to planar equilibrium geometry. This particular vibrational motion shows a clear propensity to move to the geometry of the CI.

Perhaps the most informative experiments with regard to the photodissociation of NH_3 were the extensive Rydberg tagging experiments by Ashfold's group that have yielded a plethora information regarding the interplay between adiabatic and nonadiabatic dissociation following state specific UV excitation to the $\tilde{A}^1A_2''$ PES. By monitoring the KE on the H photoproduct following population (and subsequent dissociation) of the $v_2' = 0$ and 1, Biesner *et al.*[117] clearly showed that photodissociation occurred exclusively nonadiabatically, with low amounts of vibrational excitation being deposited primarily into the v_2 bending vibrational mode of the NH_2 with a wide distribution of rotational excitation. These studies were later expanded to examine the

photodissociation dynamics from the $v_2' = 0 - 6$[118] vibrational states. Further studies by Mordaunt *et al.*[121], examined the effect of deuteration upon the dissociation, in doing so they found a correlation between the rotational excitation of the ND_2 and the measured anisotropy parameter (β_2) of the eliminated H. This angular dependence of H elimination upon initial and final rotational states of NH_3 and NH_2 respectively was modelled by Dixon[107-108] using a semi-classical impact parameter model.

Despite the large numbers of studies in the frequency domain, only a few studies of H transfer in clusters[137-138] and of high-lying Rydberg states[132-133] have been completed in the time domain. Of particular pertinence to this work are these time-resolved cluster measurements, which speculated ultrafast H transfer in NH_3 dimers and trimers, through ionisation and subsequent detection of the H transfer intermittent state. In the experiments presented in this chapter, H elimination from isolated NH_3 is directly probed, as compared to the indirect measurements of N-H dissociation in the cluster studies.

Using a combination of pump/probe spectroscopy and VMI the proceeding sections describe work completed towards studying the multichannel dynamics of the dissociation of the N-H bond, following excitation of the $v_2' = 4$ of the first electronically excited ($\tilde{A}^1A_2''$) PES of ammonia. Through a combination of pump/probe methodologies and KE resolution, partial separation of dissociation time constants into different internal energy states of the NH_2 co-fragment is possible. This has far reaching applications in enabling us to untangle competing dissociation channels in more complex systems.

3.2 Experimental

Briefly, a 10 % NH_3 in He gas mixture was expanded through an Even-Lavie valve (held at 100^oC for stability) to form a supersonic jet expansion. This was subsequently skimmed and intercepted by the co-linearly aligned pump and probe laser pulses in the centre of a repeller and accelerator electrode under VMI focussing conditions. Following photodissociation with the pump, and subsequent 2+1 REMPI of the H photo-product with the probe, the ionised fragments were accelerated along a 500 mm flight tube. At the terminus of the drift tube, these ions were detected by a vacuum imaging detector (VID), or MCP when performing VMI or TR-MS measurements respectively (a simple MCP set-up was initially used prior to installation of VID). In the VMI measurements, the fluorescence signal from the VID, due to the H^+ was measured as a function of pump-probe delay on a purpose built LabVIEW program.

3.3 TR-MS of Hydrogen Elimination from Ammonia

Figure 3.2 shows the H^+ transient obtained via TR-MS of NH_3. Intensity of the 200 nm pulse is sufficiently low ($\approx$ 1 µJ/pulse) that no fragmentation of NH_3 is observed with the pump alone, eliminating the contribution of multi-photon processes to the observed H^+ transient.
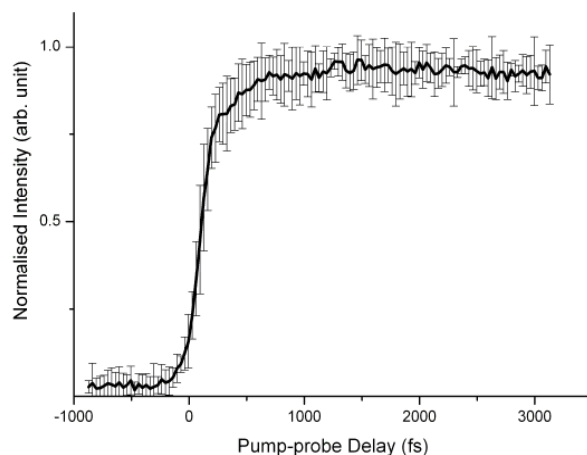
Figure 3.2, H$^+$ transient from NH$_3$ by TR-MS, following excitation of the v_2' = 4 mode of the Ã^{1}A$_2$" state in ammonia. Error bars shown correspond to a 95 % confidence limit.

Fitting of a single exponential rise yields a time-constant of 150 +/- 37 fs. This signal is a sum of all KE H channels; therefore this ultrafast timescale shows the *average* timescale for N-H cleavage into all NH$_2$ quantum channels.

3.4 TR-VMI of NH$_3$

Representative KE spectra observed for different time delays in the H$^+$ transients are shown in **Figure 3.3**. It is clear that at negative delays (when the probe precedes pump) no H$^+$ is detected. As the delay time increases, the H$^+$ signal also increases, until the signal becomes unchanged (suggesting that all dissociation events are complete) at a delay time of approximately of 1000 fs.
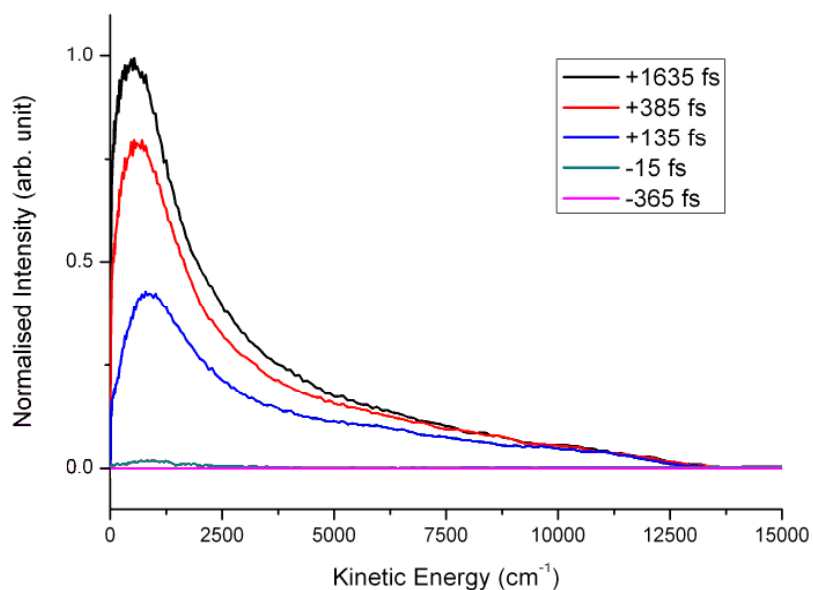
Figure 3.3, KE spectra from H$^+$ transients from a selection of pump-probe delays. NOTE: the KE spectra from the H$^+$ has been multiplied by the reciprocal of the reduced mass to show total KE release.

Figure 3.4 shows the total integral of each KE spectrum plotted as a function of the corresponding pump-probe delay. Fitting this with a single exponential rise yields a dissociation time constant of 170 +/- 22 fs, in very good agreement with the TR-MS measurement of 150 +/- 37 fs.
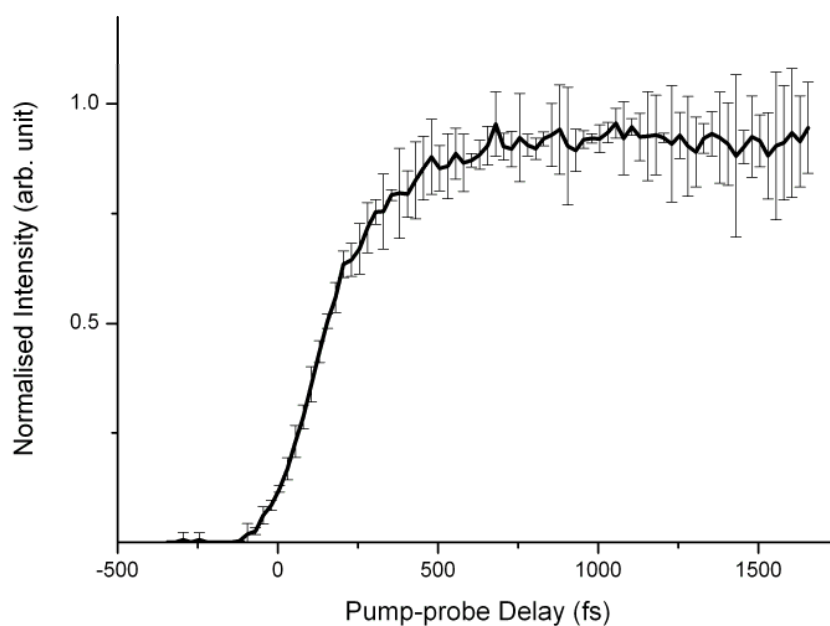
Figure 3.4, total integral of KE spectra from TR-VMI of H$^+$ from NH$_3$, following excitation of the v_2' = 4 mode of the Ã^{1}A$_2$" state. Error bars shown correspond to a 95 % confidence limit.

Biesner *et al.*[118] suggest that non-adiabatic photo-dissociation in NH$_3$ leads primarily to population of the bending vibrational mode (v_2) of the X̃^{2}B$_1$ state NH$_2$ product. Fitting the energies of the different quanta of v_2 excitation, calculated by these authors[118], with a polynomial function enabled the determination of the energies of the higher quanta excitations within this mode that are energetically populated following photo-dissociation at 200 nm (D_0 experimentally determined to be 37115 cm^{-1} Mordaunt *et al.*[120]). The associated energies of these overtones are displayed in table 3.1.

$v_2 =$	Energy of State (cm^{-1})	Total KE (cm^{-1})
0	0	12885
1	1495	11390
2	2958	9927
3	4389	8496
4	5784	7100
5	7142	5743
6	8461	4424
7	9739	3146
8	10974	1911
9	12164	721

Table 3.1, calculated energies of the bending vibrational mode (v_2) of the $\tilde{X}^2B_1$ state of NH_2, and the associated maximum total KE that may be observed, assuming population of this vibrational mode (i.e., E_{photon} - D_0 - $E_{Vibration}$ = *total KE*, where E_{photon} is the photolysis photon energy, D_0 is the dissociation energy and $E_{vibration}$ is the energy of associated vibrational state).

Using these calculated KEs, it is possible to partially resolve the KE spectra with respect to vibrational state product distribution. **Figure 3.5** shows the TKE and the corresponding quanta of excitation in the v_2 mode in the $\tilde{X}^2B_1$ NH_2 product.
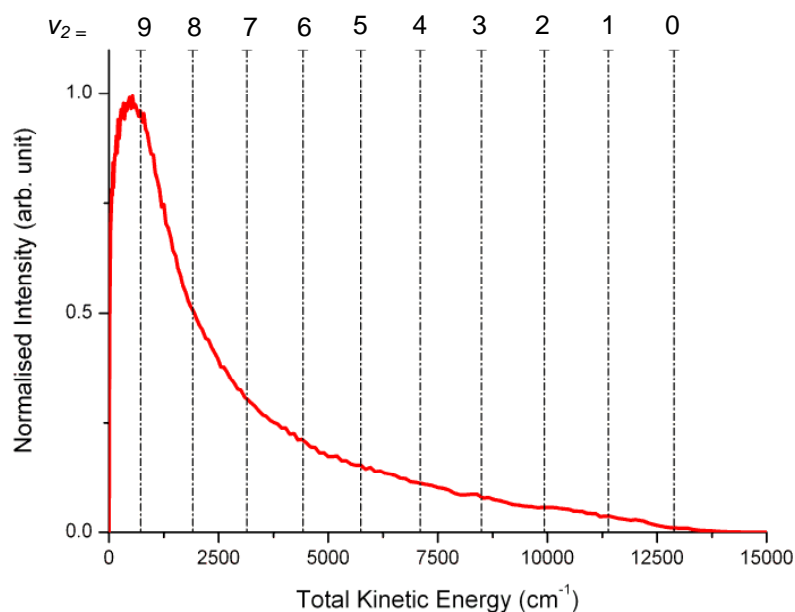
Figure 3.5, KE spectrum from H$^+$ transient at a pump/probe delay of 1000 fs. The corresponding energies for different quanta of v_2 excitation in the NH$_2$ $\tilde{X}^2B_1$ state is also shown.

It is worth noting at this point that due to the spectral profile of the ultrafast laser pulses utilised, the KE resolution is limited; essentially meaning that rotational resolution is not feasible. By integrating KE regions corresponding to certain quanta of excitation in the v_2 mode of the accompanying NH$_2$ photofragment, dissociation time-constants into various product quantum states is possible. Several examples of these vibrationally resolved dissociation timescales are shown in **Figure 3.6**.
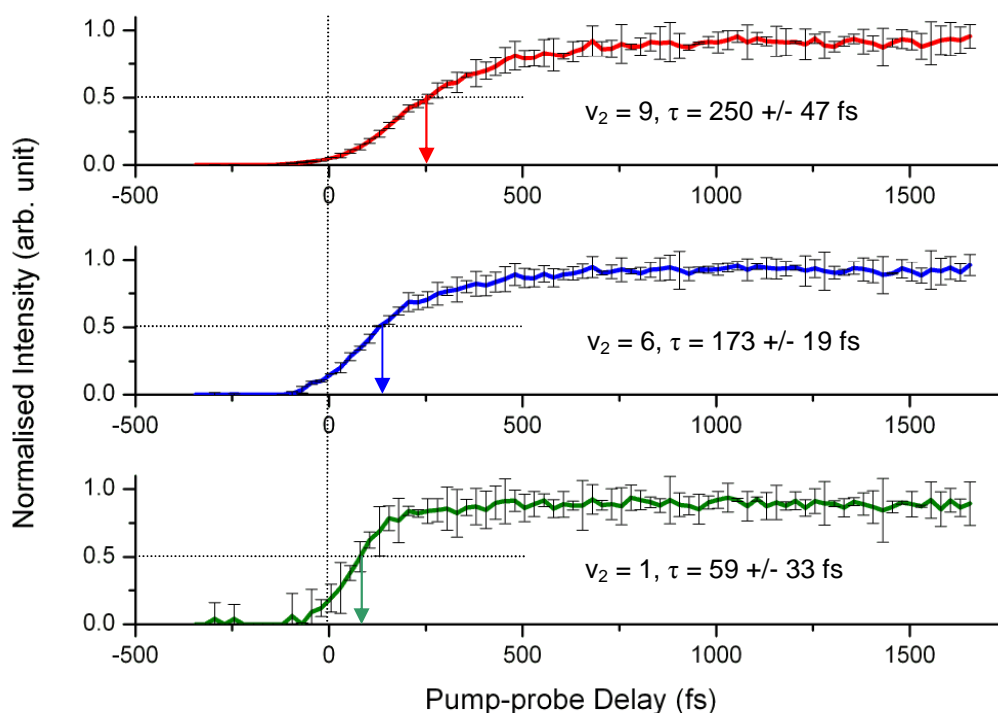
Figure 3.6, integrals from assigned vibrational channels, v_2 = 9 (red), v_2 = 6 (blue) and v_2 = 1 (green). It is clear that dissociation timescales vary considerably across the TKER spectrum. Error bars shown correspond to a 95 % confidence limit.

It is clear from the fitting of these partially resolved channels that dissociation into different product states occurs on different time-scales. Fits to each KE integral required a single exponential rise function, the signal to noise ratio of the v_2 = 0 meant a reliable fit to this channel was not possible. These fits are summarised in table 3.2.

v_2	0	1	2	3	4	5	6	7	8	9
τ (fs)	-	59 +/- 33	94 +/- 51	135 +/- 17	147 +/- 20	155 +/- 17	173 +/- 19	173 +/- 17	151 +/- 22	250 +/- 47

Table 3.2, table of fitted time-constants to different regions of KE spectrum assigned by quanta of excitation in the v_2 mode of the corresponding $\tilde{X}^2B_1$ state NH_2 co-fragment.
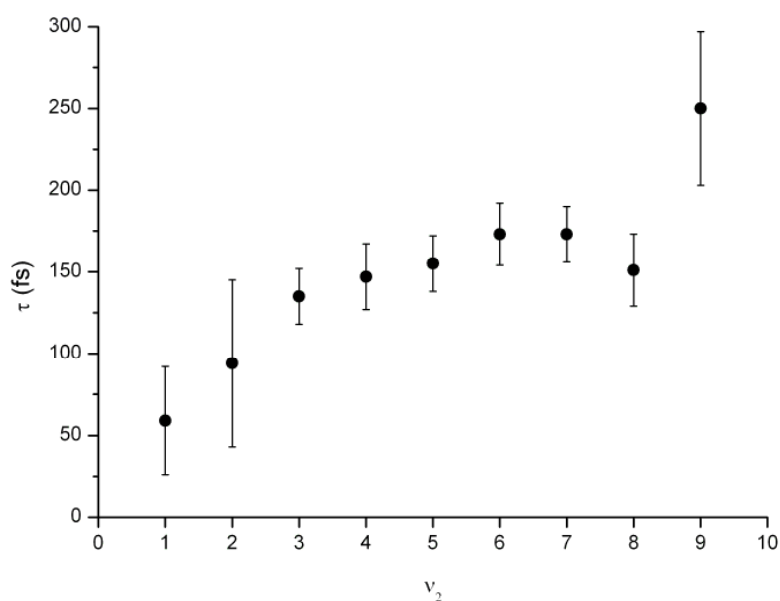
Figure 3.7, plot of fitted time-constants vs. amount of quanta in the v_2 mode.

Figure 3.7 shows the plot of fitted time-constants vs. product states. It is clear that as the KE imparted onto the H increases (that is, as internal excitation in NH_2 decreases), the time-constant for dissociation generally decreases. It is also seen that the measured dissociation time-constants appear to plateau between $v_2 = 3$ to $v_2 = 8$, whilst there is a sudden increase in the measured time-constant for $v_2 = 9$, where adiabatic dissociation is energetically open. Extrapolation of the last few vibrational channels to $v_2 = 0$, suggests that dissociation into the highest possible KE channel occurs in < 50 fs, in close agreement with linewidth[98] measurements and more recent full-dimensional quantum mechanical calculations[115].

3.5 Rotational Excitation

Frequency domain experiments have shown population of a variety of different rotational states within the $\tilde{X}^2B_1$ state of the NH_2 fragment following dissociation from the $v_2' = 4$ mode of the $\tilde{A}^1A_2"$ state in NH_3[117]. Due to the spectral bandwidth of fs pulses, rotational resolution is not possible here. Therefore it is plausible that contribution to vibrational channels identified above could be from lower vibrationally states with large amounts of rotational excitation, as observed by Biesner *et al*[118].

3.5.1 Anisotropy Parameters

Mordaunt *et al.*[121] successfully showed an angular dependence of H elimination upon the degree of rotational excitation in the partner ND_2 following excitation of the $v_2' = 0$ of the $\tilde{A}^1A_2"$ state of NHD_2. Our imaging set-up enables similar measurements of the angular dependence of H elimination. Comparative measurements were therefore carried out in NH_3 specifically aimed at studying the effect of high vibrational excitation (of the v_2' mode) on the degree of anisotropy of the H fragments and the product quantum states of the NH_2 partner fragments.
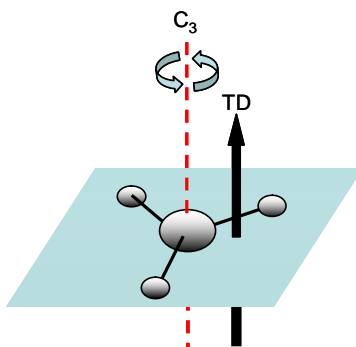
Figure 3.8, schematic of trigonal planar structure of $\tilde{A}^1A_2$" PES with C_3 axis and $\tilde{A} \leftarrow \tilde{X}$ transition dipole moment (TD) shown. Molecular plane highlighted in blue.

The $\tilde{A}^1A_2$" PES has a trigonal planar geometry, with the $\tilde{A} \leftarrow \tilde{X}$ transition dipole moment parallel to the C_3 axis, as shown in **Figure 3.8**. The laser preferentially excites molecules with their transition dipole aligned with the laser polarization axis (perpendicular to molecular plane). NH_2 fragments formed with low rotational excitation are formed with internuclear trajectories that pass straight through the CI, as NH_2 fragments with low rotational excitation are formed with little out of plane torque. As a result, H photofragments are formed primarily perpendicular to the laser polarization, hence the negative measured anisotropy parameters. Trajectories resulting in high rotational excitation experience more out of plane torque, and as such parallel H elimination occurs, with a positive measured anisotropy parameter.
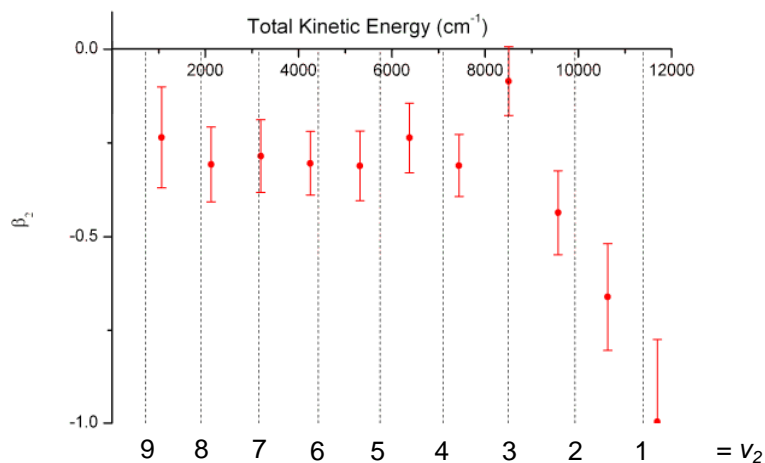
Figure 3.9, measured anisotropy parameters for different KEs. v_2 channels highlighted. Error bars shown correspond to the calculated 95 % confidence limit.

Figure 3.9 shows the measured anisotropy parameters of H as a function of total KE release. The measurement of the limiting case of -1 for high KE H elimination suggests that the NH$_2$ partner fragment has very little rotational excitation upon dissociation.

3.5.2 Calculation of Anisotropy Parameters

Dixon and co-workers[107,119] established that dissociation into different rotational states of NH$_2$ result in different H anisotropy parameters. The semi-classical impact parameter model developed in that work, relates the dissociation trajectory, the initial optically prepared state and the rotational state of the corresponding NH$_2$ photoproduct to the H recoil anisotropy (β_2). This model works under the assumption that no further forces act upon the system beyond the CI during dissociation. The conservation of energy and angular momentum results in a relationship between the rotation about the non-principle axis of the NH$_2$ photoproduct and the outgoing H trajectory and hence β_2 when considering

the dissociation in a fixed body frame[107]. This relationship is given by equations 3.1 and 3.2

$$\beta_2 = A_0 P_2 (\cos x) \tag{3.1}$$

$$\frac{\beta_2}{A_0 (J', J'', K)} = \frac{3N(N+1)\hbar^2}{2\mu R_{TS}^2 E_T (N)} - 1 \tag{3.2}$$

P_2 is the second order Legendre polynomial, x is the angle between the transition dipole and dissociating bond, μ is the reduced mass, R_{TS} is the CI internuclear displacement, J' is the initially prepared rotational state in the parent NH_3, J'' is the rotational state of the ground state NH_3 prior to optical excitation, K is the rotational state about the non-principle axis in both NH_3 (and NH_2), E_T is the KE release for a particular N (rotational state in NH_2) and A_0 is the alignment parameter. The alignment parameter is dependant upon J', J'' and K. A_0 is described by equation 3.3.

$$A_0 (J', J'', K) = (-1)^{J'+K} \sqrt{30}(2J'+1) \begin{pmatrix} J' & J' & 1 \\ K & -K & 0 \end{pmatrix} \times \begin{Bmatrix} J'' & J' & 1 \\ 2 & 1 & J' \end{Bmatrix} \tag{3.3}$$

The two last terms of this expressions are the 3-j and 6-j coupling symbols, taken from work by Zare[166]. These terms describe the coupling between two and three angular momentum vectors respectively. In the two vector case, a coupled state, $|jm>$, is represented by two vectors j_1 and j_2 precessing around the resultant vector, j, which in turn precesses around the z axis. The precession of j_1 and j_2 results in variable z components for these vectors (m_1

and m_2 respectively), although at any given time the sum of m_1 and m_2 is equal to the z component (m) of j. The square of the 3-j symbol may thus be interpreted as the probability density for instantaneous coupling of the uncoupled state $|j_1m_1, j_2m_2>$ to form a new state, $|jm>$, with a resultant length of $[j(j+1)]^{1/2}$. A schematic for this is shown in **Figure 3.10**. A similar pictorial representation of 6j coupling can be found in reference 166.
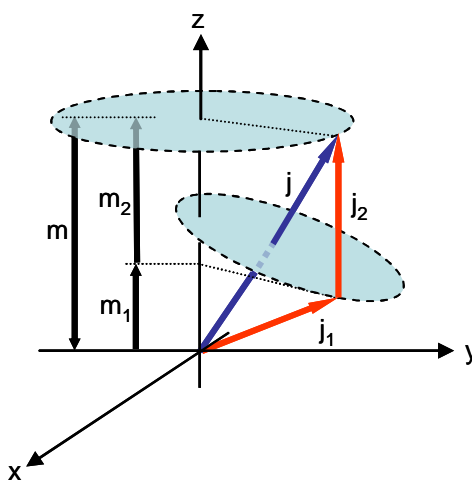
Figure 3.10, vector model representation of a coupled state |jm> as discussed in the preceding paragraph.

The three strongest transitions for $v_2' = 4$ mode of $\tilde{A}^1A_2"$ state of NH_3 were determined to be the $R_0(0)$, $Q_1(1)$ and $R_1(1)$ using PGopher, where the transition nomenclature is given as, $\Delta J_K(J)$. Using 3-j and 6-j symbols derived from these transitions (calculated using Mathematica) expected anisotropy parameters into different vibrational channels of the NH_2 in these experiments were simulated.
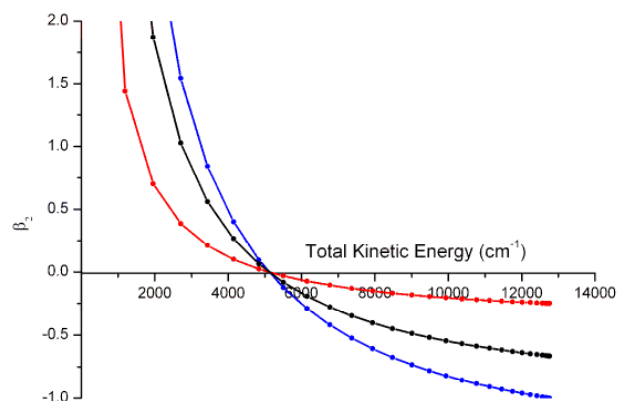
Figure 3.11, simulated anisotropy parameters for $R_0(0)$ (blue), $Q_1(1)$ and $R_1(1)$ (red) transitions dissociating into $v_2 = 0$ NH$_2$ product channel. Weighted average of these transitions shown in black, Kinetic energy assignments made using reference 118.

For low rotational excitation in the NH_2 photoproduct, negative anisotropy parameters are predicted for each of the transitions- for the $R_0(0)$ transition a β_2 of -1 is predicted, whilst for $Q_1(1)$ and $R_1(1)$ transitions, a value of -0.25 is predicted, due to 3-j and 6-j terms being equivalent for both $Q_1(1)$ and $R_1(1)$ transitions. **Figure 3.11** shows the predicted anisotropy parameters for each of the three transitions, as well as a weighted average (predicted intensities of 0.554, 0.229 and 0.217 respectively).
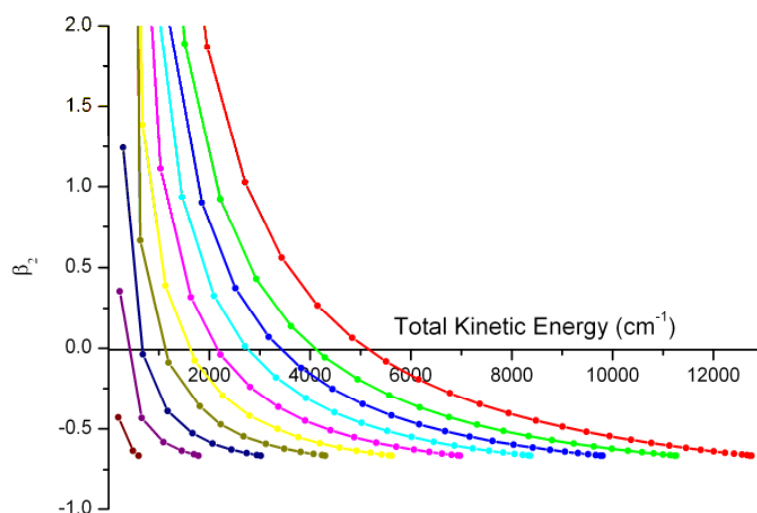
Figure 3.12, simulated anisotropy parameters for weighted average of transitions across all vibrational channels i.e., $v_2 = 0$ (red) to $v_2 = 9$ (dark brown) in NH_2. KE assignments made using reference 118.

The trends observed for these three transitions are repeated across all vibrational channels, with decreasing KE, as shown in **Figure 3.12.** It is clear that use of this impact parameter model to interpret the experimentally observed anisotropy parameter is insufficient (compare to **Figure 3.9**). The impact parameter model holds for low J' and J'' values and low vibrational states, under the assumption that all trajectories pass through the CI (assumed to be at a single internuclear separation in all cases), but here the mixture of populated high vibrational states and relatively high J' and J'' values appears to result in the breakdown of this model for anything but the highest KE H observed in these experiments.

3.6 Conclusions

The use of TR-VMI to observe the photodissociation of NH_3 following population of the $v_2' = 4$ of the first electronically excited $\tilde{A}^1A_2''$ state has allowed partial separation of state specific dissociation channels[167]. Although these measurements have not enabled separation of rotational fine structure within the photo-products, due to the time-bandwidth product associated with fs light pulses, they have provided evidence that this technique may further enhance time-resolved measurements by providing moderate energy resolution.

It is clear that channels leading to high KE H elimination occur on faster timescales than low KE channels. Extrapolation of our data leads to a dissociation time-constant of < 50 fs for the $v_2 = 0$ channel, in very close agreement with predictions from simulated spectra[115] and frequency resolved measurements[98]. The observation of an extended dissociation time-constant into the $v_2 = 9$ channel suggests that adiabatic dissociation is contributing to the H signal at these low KEs. This slower time-constant may be reconciled as the wave-packet's velocity slowing during adiabatic dissociation, due to the wave-packet having to climb up the PES as it avoids the CI to yield electronically excited NH_2 products.

The observation of negative anisotropy parameters across the entire KE spectrum strongly suggests that low levels of rotational excitation are deposited into the NH_2 fragments during dissociation[121]. This work has also shown how a

simple impact parameter model is insufficient to describe photodissociation into vibrationally excited products.

3.7 Future Work

Quantum dynamical calculations are currently underway to describe this dissociation process in more detail. These simulations will be highly complimentary to the experimental findings presented in this chapter. Moreover these experimental findings will provide a stringent test of the qualitative and quantitative suitability of these calculations.

Efforts are also underway to perform vibrationally mediated experiments, in much the same way as the experimental work of Crim and co-workers[125-130], where an intermediate vibrational state is populated prior to electronic excitation, essentially altering the accessible Franck-Condon region, and thus affecting the observed dissociation dynamics. In using a fs excitation source, study of *time-dependant* Franck-Condon factors will now be possible, and perhaps indirect probing of the de-coherence of the initially prepared vibrational state.

4. Nitrogen Containing Five Membered Rings

4.1 Briefing

Studying a structural analogue of the 5-membered ring component in adenine will develop a clearer understanding of the impact of increasing the internal degrees of freedom (vibrational modes) within a hetero-aromatic system and the involvement of πσ* PESs in the photodissociation dynamics. The relationship between molecular size and degrees of freedom is shown by equation 4.1, where s is the degree of freedom, N is the number of atoms in the species and k is the number of geometrical constraints ($k = 5$ in a linear system and 6 in a non-linear species).

$$s = 3N - k \qquad (4.1)$$

Previous work by DeWitt and Levis[168-169] (and references therein) in substituted benzene species have shown that as the number of atoms in the molecule increases and hence the internal degrees of freedom also increase, the extent of fragmentation also increases following optical excitation with fs pulses. Since non-statistical dissociation processes via πσ* PESs are expected to be prominent following UV excitation in these hetero-aromatic species, they provide an ideal starting point to investigate the effect of increasing internal degrees of freedom upon non-statistical processes.

To achieve this, imidazole and methylated derivatives thereof were studied. Due to a general lack of dynamics studies on imidazole, pyrrole was also studied, which has a very similar geometrical and electronic structure to imidazole and also enables direct comparison with other related studies in pyrrole.

PESs calculated by Sobolewski and Domcke[82] for pyrrole clearly identify the presence of πσ* surfaces which are predicted to be active following UV excitation. Following photoexcitation and probing at 243.1 nm and observed using VMI, Temps and co-workers[88] noted very fast H elimination occurring perpendicular to the laser polarization, following population of the optically bright ππ* PES. This was consistent with the wavepacket propagating from the ππ* PES to a repulsive πσ* PES on an ultrafast timescale eventually leading to direct dissociation. Comparison with 1-methylpyrrole, where this fast channel is effectively blocked, confirmed the heteroatom co-ordinate as responsible for this mechanism. In both pyrrole and the methyl derivative, a slower IC mechanism was also identified. Later work by Lippert *et al.*[91] at 250 nm, directly populating the πσ* surface, observed H elimination in 100 fs, consistent with the involvement of the πσ* surface. These authors also recorded a secondary slower component, occurring in 1.1 +/- 0.5 ps, consistent with reflection and trapping of the wavepacket on the excited PES, subsequently followed by IC to the electronic ground state and then dissociation. Later work by Temps[89], at 217 nm, studied deuterated pyrrole (at the heteroatom co-ordinate) and observed fast H elimination, which was attributed to C-H bond fission, although

the authors were careful to point out that this may be due to H/D exchange in the gas line of their apparatus.

Recent MRCI calculations in pyrrole[84,86] and imidazole[94] have suggested the participation of a ring opening mechanism, which involves a separate $\pi\sigma^*$ PES with respect to a N-C co-ordinate leading to heavier photofragments. These calculations have also confirmed the involvement of the $\pi\sigma^*$ surface with respect to the N-H co-ordinate in both of these species[85,94], in line with previous experimental and theoretical findings. Whilst other fragmentation pathways are operative, the results for pyrrole yielded 80 % of the calculated trajectories from the $\pi\pi^*$ PES as dissociating along the N-H co-ordinate via the $\pi\sigma^*$ PES[85] following excitation at 6.55 eV, illustrating the dominance of this pathway in the photochemistry of pyrrole.

Initially presented in this chapter are H elimination results from pyrrole. The results obtained in imidazole, 2-methyl, 4-methyl and 2,4-dimethyl derivatives are subsequently presented. By studying pyrrole, we are able to compare the effects of C substitution on the dynamics of H elimination. By studying the methylated derivatives of imidazole we are able to make inferences regarding the involvement of non-statistical dissociation processes in systems with increasing internal degrees of freedom.

The 1-methylimidazole derivative has also been examined to determine the contribution of H from C-H co-ordinates, which has been experimentally observed in pyrrole[89]. Simulations in imidazole[94] by Barbatti and Lischka, have

identified a πσ* surface with respect to the C-H co-ordinates in imidazole which supports this experimental observation in pyrrole, and as such the relative contribution of this channel needs to be determined to allow confident assignment of heteroatom co-ordinate dissociation channels, discussed in the proceeding section.

4.2 Potential Energy Surfaces

The only available PESs of imidazole[93] are based on calculations for pyrrole[82]. As yet unpublished calculations on imidazole have recently been performed by Nix[170] at the B3LYP level, which are shown in **Figure 4.1**. This work has also been expanded to encompass 2-methyl, 4-methyl and 2,4-dimethyl derivatives studied here, presented in **Figure 4.2**. It is apparent, from **Figure 4.2** that methylation lowers the energy of the repulsive πσ* PES. The reduction in energy can be attributed to either: (1) stabilisation of the molecule and radical, effectively lowering the energy of the πσ* surface; (2) destabilisation of the ground state potential, effectively increasing the energy of the S_0 surface; (3) a combination of the two. It is interesting to note from **Figure 4.2** that as the πσ* surface is reduced in energy with increasing methylation, a barrier on this surface begins to emerge, the height of which increases with methylation. These barrier heights are presented in Table 4.1, and correspond to the difference in energy between the well and barrier maximum. The following dynamics measurements of imidazole and methyl derivatives thereof provide a qualitative test of the accuracy of these calculated surfaces, which will be discussed later on in this chapter.
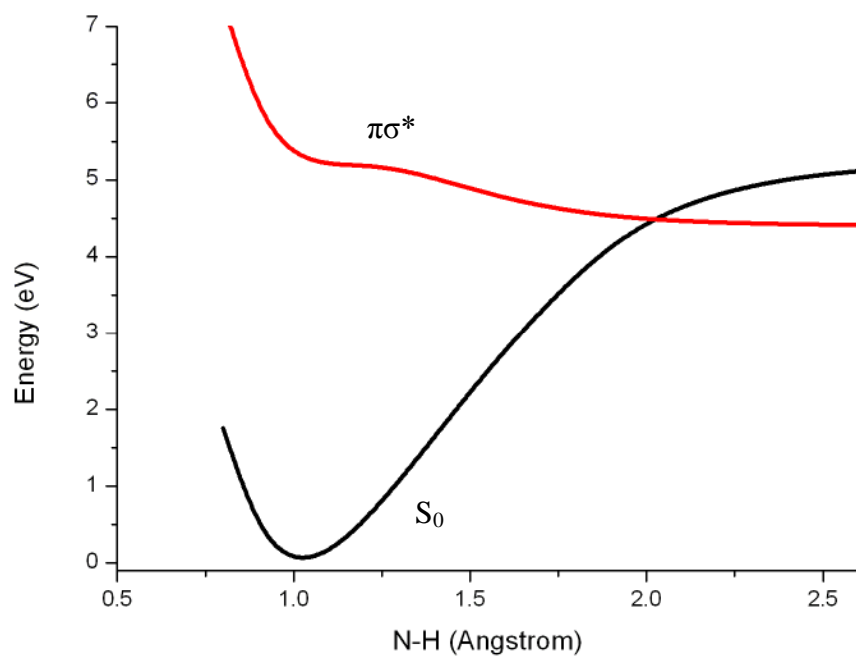
Figure 4.1, πσ* and ground state PESs for imidazole, taken from reference 170.
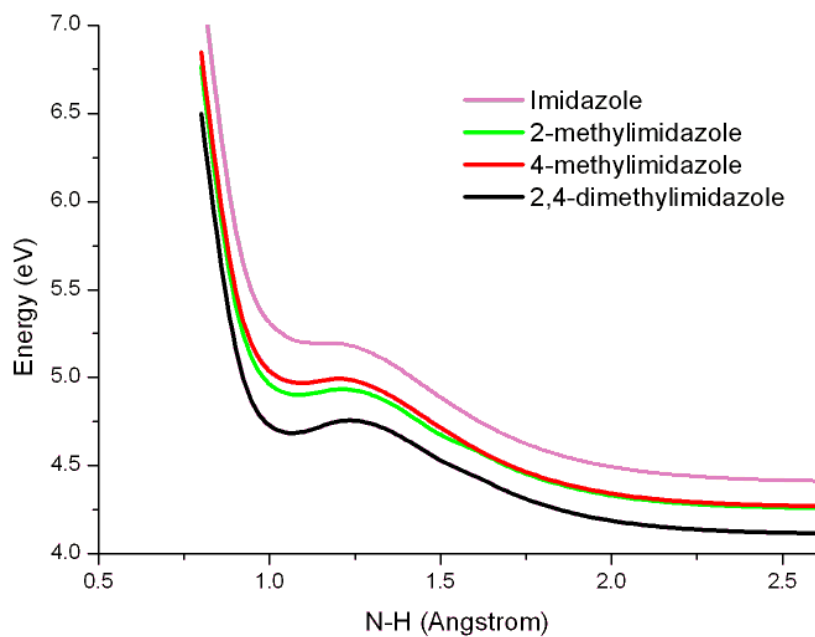
Figure 4.2, πσ* PES of imidazole, 2-methylimidazole, 4-methylimidazole and 2,4-dimethylimidazole, taken from reference 170.

Species	Barrier Height (eV)
imidazole	0
2-methylimidazole	0.038
4-methylimidazole	0.031
2,4-dimethylimidazole	0.065

Table 4.1, barrier heights on πσ* PES, taken from reference 170.

4.3 Experimental

Briefly, species under study are heated to generate sufficient vapour pressure, typically $70^{o}C$ - $100^{o}C$ depending on the molecule, and co-expanded with He through an Even-Lavie valve to form a supersonic jet expansion. This is subsequently skimmed and intercepted by the co-linearly aligned pump and probe laser pulses in the centre of the repeller and accelerator electrodes under VMI focussing conditions. Following photodissociation with the pump, and subsequent 2+1 REMPI of the H photo-product with the probe, the ionised fragments are accelerated along a 500 mm flight tube. At the terminus of the drift tube, these ions are detected by an MCP (or VID when performing VMI). The yield of H^{+} signal as a function of time delay between pump and probe pulses is recorded and analysed on a purposely built LabVIEW program.

4.4 Hydrogen Elimination from Pyrrole

Figure 4.3 shows the observed H^{+} transients from pyrrole (heated to $100^{o}C$) following excitation at 200 nm, using a 2+1 REMPI mechanism to ionise H.

Dissociation along the πσ* surface following excitation at 200 nm was measured as occurring in 107 +/- 33 fs, consistent with previous measurements[91].

Perhaps the most striking result of this measurement is that no evidence of a slower mechanism consistent with a IC mechanism was seen, which has been observed by Lippert *et al.*[91] This suggests that passage of the wavepacket through the ππ*/πσ* CI is very efficient following excitation at 200 nm. The prominent role of this CI may be due to the fact that the initial excitation is ≈ 17000 cm^{-1} above the dissociation energy of the N-H co-ordinate[90], increasing the probability for the wavepacket to pass non-adiabatically through the ππ*/πσ* CI and directly dissociate to ground state pyrrolyl and H fragments.
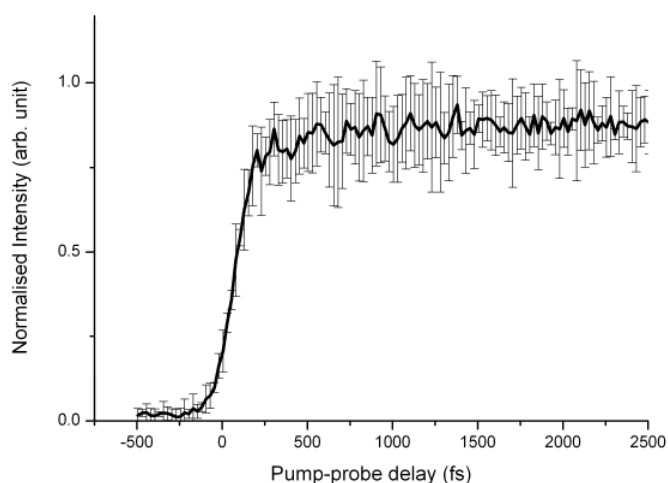
Figure 4.3, H+ transients from pyrrole. Error bars shown correspond to a 95 % confidence limit.

4.5 Velocity Map Ion Imaging of Imidazole

The measured kinetic energy spectrum following photodissociation at 200 nm in imidazole is presented in **Figure 4.4**. The kinetic energy spectrum clearly shows bimodal distribution, which is qualitatively similar to what has previously been observed in TKER measurements in both pyrrole[90], and imidazole[93] at similar excitation energies. However these two studies have a larger low KE contribution (at 193.3 nm), which may be due to the fact that these are ns laser based experiments, suggesting that a contribution from a slower process beyond the temporal window of our measurements are contributing to this low KE portion of the KE spectrum. The bimodal distribution seen in imidazole is replicated in the methyl derivatives studied.
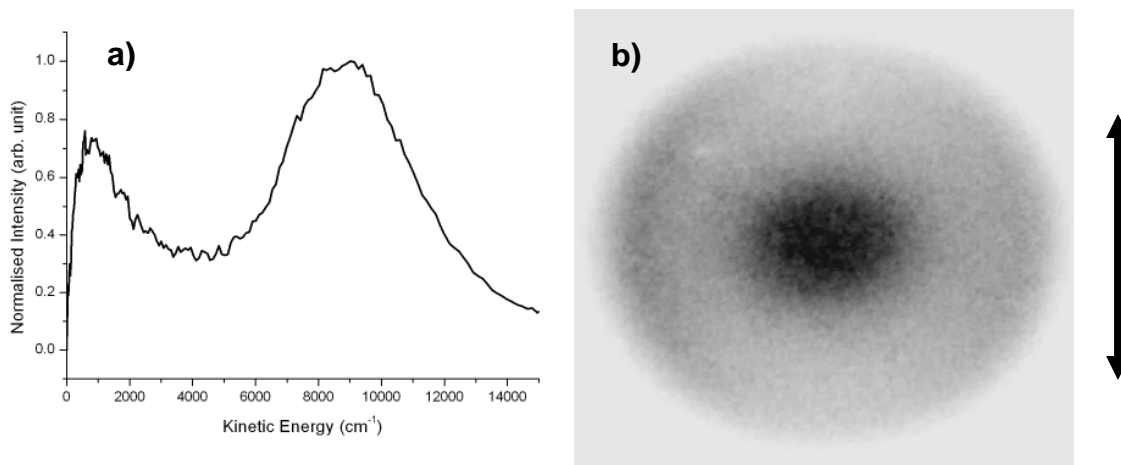
Figure 4.4, a) kinetic energy released upon H fragment following photodissociation of imidazole at 200 nm; b) raw H$^+$ projection with laser polarisation shown on right. The delay between pump (200 nm) and probe (243.1 nm) was set at 2500 fs
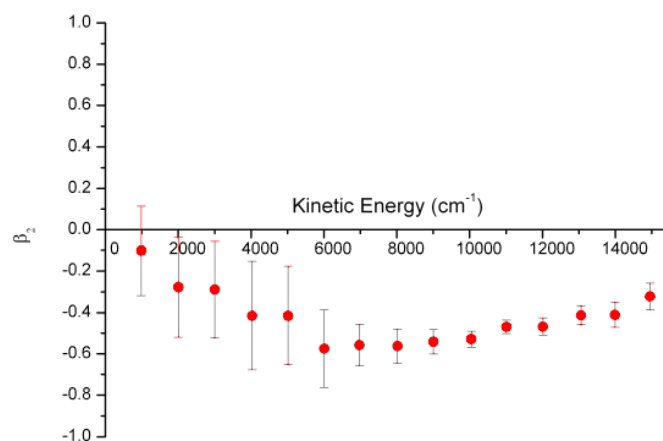
Figure 4.5, anisotropy parameter as a function of KE. At all kinetic energies H elimination occurs with perpendicular character.

Figure 4.5 shows the anisotropy parameter plotted as a function of KE. It is clear that at all KEs, dissociation is perpendicular in character (negative β_2) in agreement with previous measurements[93]. The anisotropy in the low KE region suggests that a slow IC mechanism is not operative in imidazole, as a more isotropic distribution would be seen from slower mechanisms, as the excited molecules undergo multiple rotations prior to dissociation. This negative anisotropy parameter at low KE suggests that adiabatic dissociation (with respect to the $\pi\sigma^*/S_0$ surface crossing), leading to electronically excited imidazolyl may well be contributing to the observed signal. Such a mechanism has also been proposed in analogous measurements carried-out in phenol leading to excited state phenoxyl radicals[171, 172].

4.6 Time-Resolved Hydrogen Elimination

Figure 4.6 shows the measured H^+ transient from imidazole (bottom) as well as two colour mass spectra (pump/probe signal minus probe alone signal-top)

for different pump/probe delay times. Part a clearly shows that when the pump precedes the probe there is a sizeable increase in H^+ signal. Part b (at time zero) clearly shows an enhanced parent ion signal showing the multiphoton nature of this signal and part c shows no H^+ signal when the probe precedes the pump. It is worthy of note that the mass spectra presented here are typical of what one sees for the adenine experiments. Fitting of the H^+ transient with a single exponential rise yields a dissociation time constant of 53 +/- 48 fs. This timescale is considerably shorter than the 107 +/- 33 fs obtained for pyrrole, as illustrated in **Figure 4.7**.
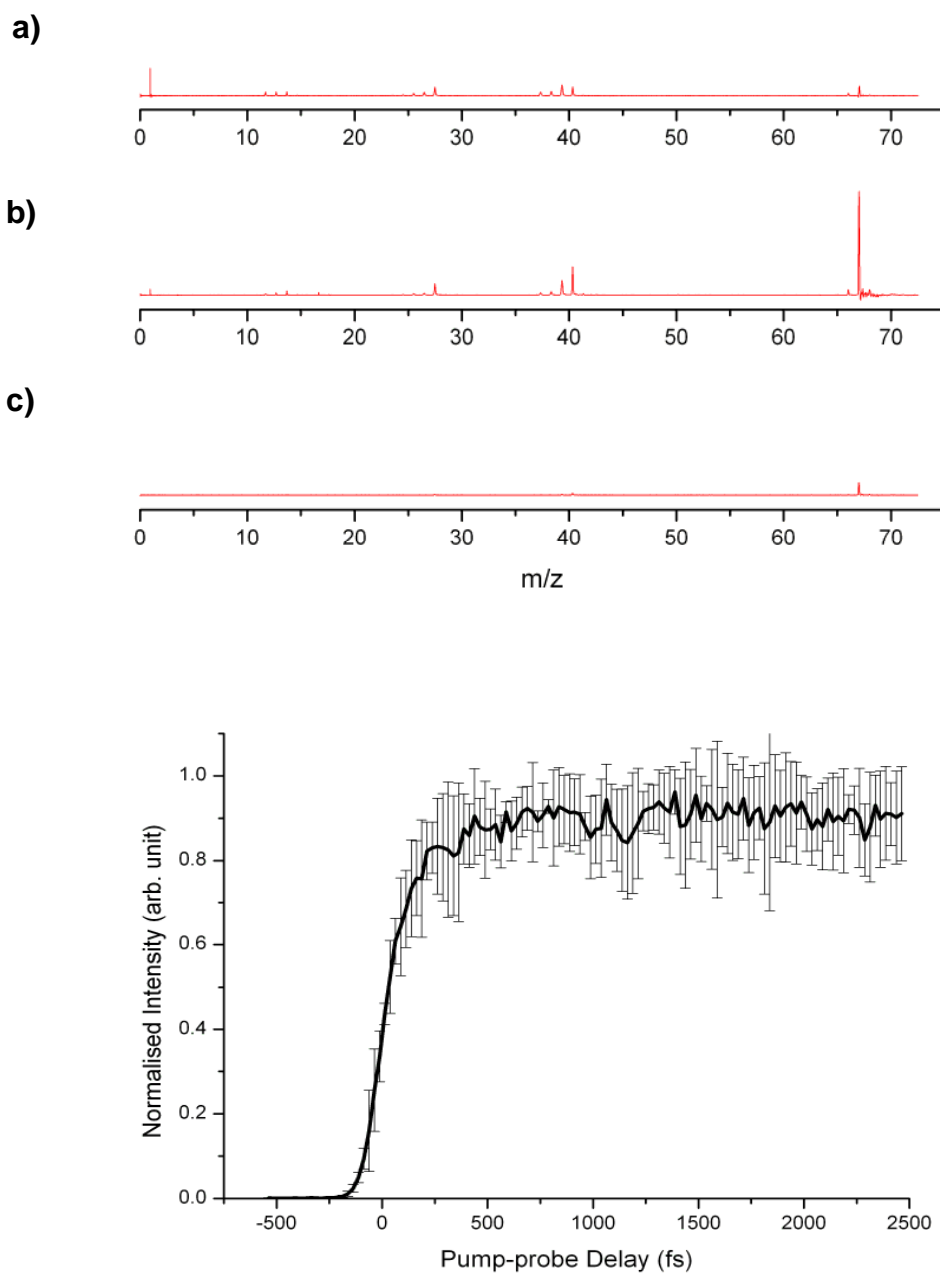
Figure 4.6, (top) representative 2-colour mass spectra from different pump/probe delays (absolute intensities shown): a) when pump precedes probe by 1000 fs; b) when pump and probe arrive at the same time (time-zero) and c) when probe precedes pump by 1000 fs. NOTE: H$^+$ signal greatly increases when pump precedes probe; (bottom) H$^+$ transient from imidazole, single exponential rise fit of 53 +/- 48 fs. Error bars shown correspond to a 95 % confidence limit.
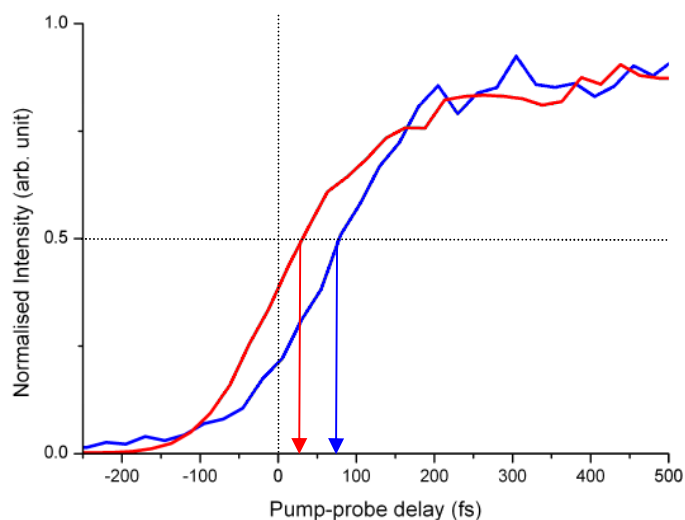
Figure 4.7, direct comparison between H⁺ transient rises in imidazole (red) and pyrrole (blue). Arrows to guide the eye to respective timescales from H atom elimination on pump-probe delay axis.

In imidazole, and all studied derivatives the neutral nature of the H signal detected was confirmed by sweeping the wavelength of the probe through the 2s ← 1s transition, clearly indicating the resonant nature of the detection scheme, an example of which is illustrated in **Figure 4.8**. It is worthy of note that the probe alone is sufficiently high enough in intensity that it can both directly populate the $\pi\sigma^*$ PES (causing H elimination) and resonantly ionise these H within the pulse envelope. As such a background level of H⁺ is routinely detected from probe alone.
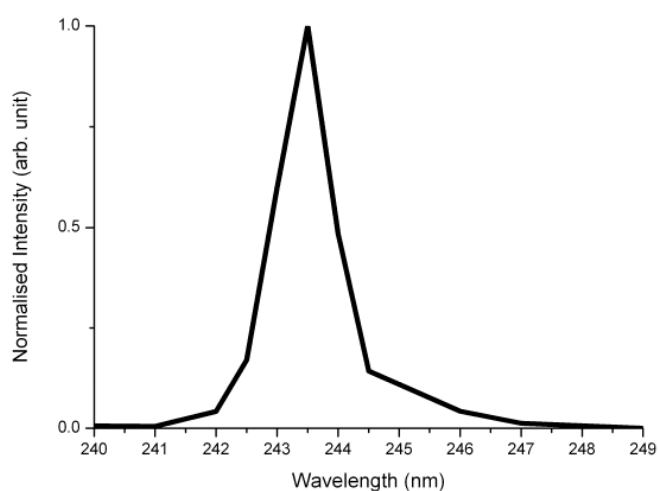
Figure 4.8, representative example of a 2-colour H$^+$ signal in 2-methylimidazole as a function of probe wavelength. The clear reduction in signal intensity as the probe wavelength is moved away from the 2+1 REMPI resonance clearly indicates the neutral nature of the H$^+$ signal.

Figure 4.9 shows H$^+$ transients observed in 4-methylimidazole, 2-methylimidazole and 2,4-dimethylimidazole (heated to 90° C, 140° C and 85^{0} C respectively). It is important to note that the yield of the pump-probe H signal was reduced in the methylated derivatives. However, due to the sensitivity of the H$^+$ signal to slight differences in alignment and fluctuations of laser intensity, it was not possible to quantify this difference in signal intensity between derivatives with any great accuracy. The fits to the observed transients show clear differences (**Table 4.2**), with the imidazole dissociating in ≈ 50 fs, and the methyl derivatives dissociating on a substantially longer timescale (≈ 100 – 120 fs). The lack of a slow component to the fits in all studied species lends further support to the conclusion drawn from the measured anisotropy parameters at low KE in the previous section, that suggest the low KE channel observed in these VMI studies is due to adiabatic dissociation, rather than some statistical process, which we would anticipate to occur on a longer timescale (> 1ps).
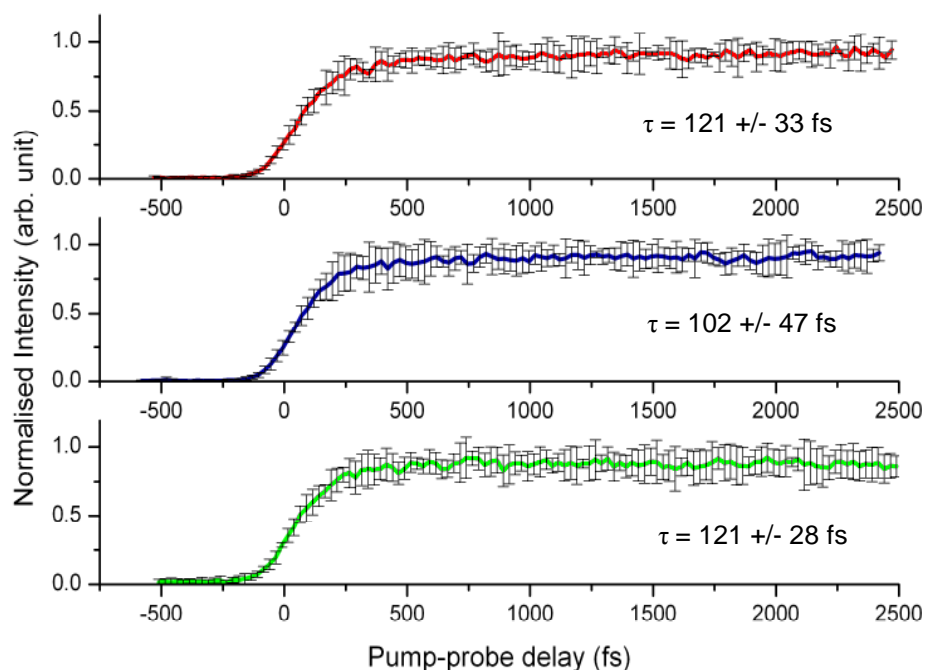
Figure 4.9, H⁺ transients from 2-methylimidazole (red), 4-methylimidazole (blue) and 2,4-dimethylimidazole (green). Error bars shown correspond to a 95 % confidence limit.

Species	τ (fs)
imidazole	53 +/- 48
2-methylimidazole	121 +/- 33
4-methylimidazole	102 +/-47
2,4-dimethylimidazole	121 +/- 28
1-methylimidazole	-

Table 4.2, fitted appearance times for H⁺ from imidazole and it's methyl-derivatives.

The observed step in the H⁺ transient for 1-methylimidazole, depicted in **Figure 4.10**, clearly indicates a dynamical process is active following excitation at 200 nm. Whilst the measured H⁺ must come from the C-H co-ordinate (the N-H coordinate is blocked), it is not possible to say with certainty whether these H's are from the ring or from the methyl group. However the previous observation

of this effect in pyrrole[89], and recent simulations in imidazole[94] suggests the πσ* PES with respect to a C-H co-ordinate on the ring itself is the most likely source of this observed signal.
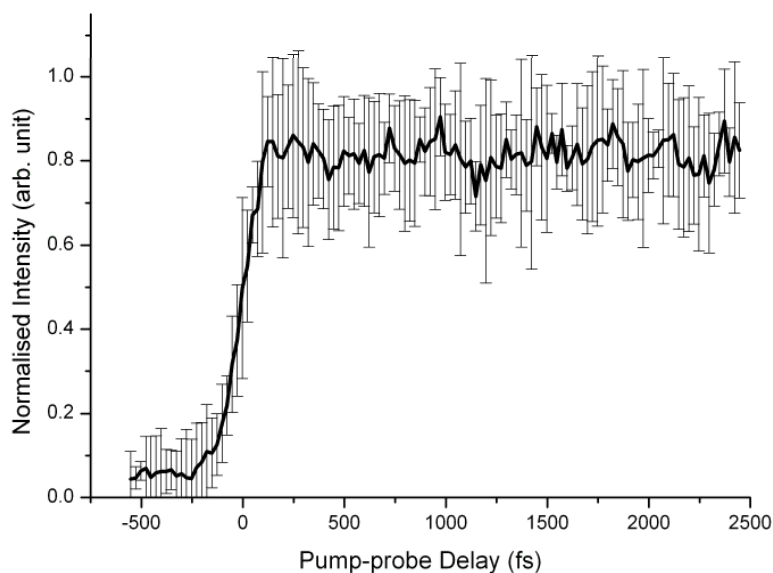
Figure 4.10, H⁺ transient from 1-methylimidazole with single exponential rise fit of 10 +/- 10 fs. Error bars shown correspond to a 95 % confidence limit.

Comparison of the pump/probe H⁺ signal intensity, normalised with respect to the signal obtained from the probe alone H⁺ signal allows comparisons of the relative contribution of the ring H's compared to H bound to the heteroatom in 1-methylimidazole and imidazole respectively. The calculated efficiencies show that the ring H's contributes much less to the H⁺ yield than the H bound to the heteroatom, by a factor of 20. This suggests once again, that the contribution to the total H⁺ from C-H is only a minor channel and as such its contribution to the observed H⁺ transients studied here in imidazole and its derivatives (excluding 1-methylimidazole) is minimal.

4.7 Conclusions

In the H^+ transients for all species (pyrrole, imidazole, 2-methylimidazole, 4-methylimidazole, 2,4-dimethylimidazole and 1-methylimidazole) there was no observation of a slow step, consistent with an IC mechanism[88-91,93]. Although there is a low KE component in imidazole and its derivatives from the VMI data (that is consistent with a slower dissociation mechanism due to statistical unimolecular decay), its absence suggests that either IC and statistical unimolecular decay is occurring on an extremely fast time-scale, comparable to that of direct dissociation or some other mechanism is active.

The difference in dissociation timescale between pyrrole (107 +/- 33 fs) and imidazole (53 +/- 48 fs) is sizeable. The $\pi\sigma^*$ surface is ≈ 3000 cm^{-1} higher in energy in imidazole[170] than in pyrrole[82], and has a steeper gradient. This may be responsible for the faster dissociation timescale and serves to illustrate the sensitivity of these time-resolved measurements to small differences in the PES. Further to this is that the dynamical measurements carried out in this work strongly suggest that the surfaces calculated by Nix[170] are qualitatively accurate.

The lack of a slow time-constant component in the H^+ transients as well as the presence a low KE channel observed in the VMI measurements suggests that adiabatic dissociation, leading to electronically excited photoproducts, is energetically accessible in imidazole and all methylated imidazole derivatives studied.

It is also evident from the fitted timescales for dissociation in the methyl derivatives that increasing the internal degrees of freedom increases the timescale for H detachment. The differences in the measured time-constants between the methylated derivatives suggests that subtle changes in the structure may influence the dynamics, however due to the large uncertainties associated with these measurements, qualitative assessment of this is not possible.

The observation of H elimination from the imidazole ring in 1-methylimidazole, clearly shows that co-ordinates other than the heteroatoms are also involved in the photodissociation dynamics. This is assigned as being due to a πσ* surface with respect to a C-H co-ordinate identified by Barbatti *et al.*[94]. However, this work strongly suggests that this is only a minor channel in the dynamics following excitation at 200 nm.

4.8 Future Studies

It is anticipated that TR-VMI studies of all species discussed in this chapter will be completed to allow direct measurement of the timescales of the high KE channels and low KE channels separately.

It is also anticipated that 4, 5-dimethylimidazole will also be studied in this manner. This study is not presented here due to the current lack of a commercial supplier of this compound. The methylation co-ordinates in this

species are where imidazole is incorporated in N^9-H adenine, and as such is a more relevant model system to study.

5. Adenine

5.1 Briefing
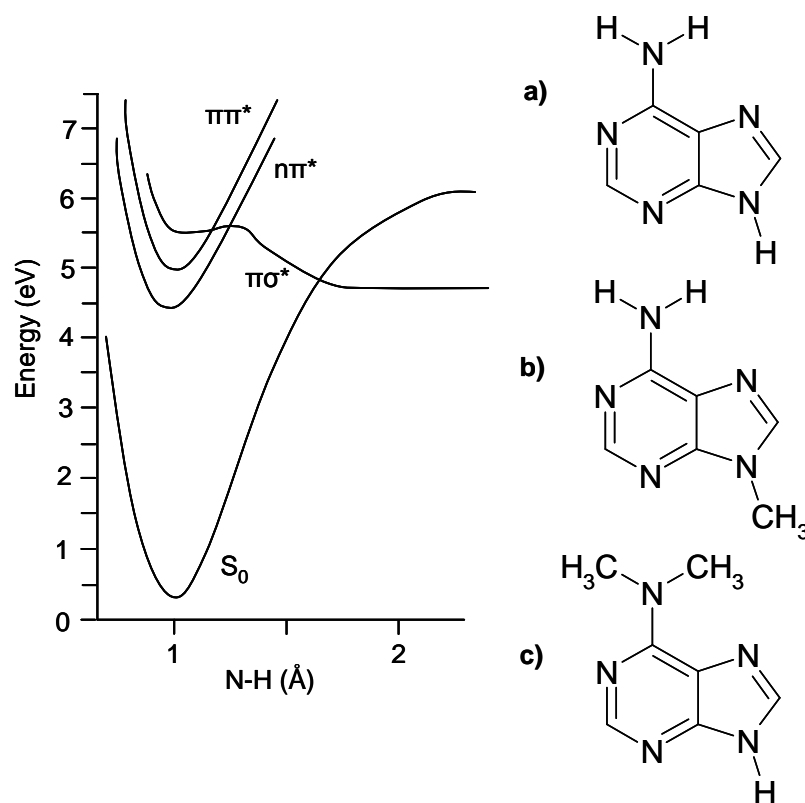
Figure 5.1, PES of N^9-H co-ordinate of adenine, with structures of studied species shown on right. a) Ade; b) 9-MA and c) 6-DMAP. PESs adapted from reference 38.

In an aim to try and develop a full picture of the nature of the photo-resistive properties of DNA, much effort has been focussed into examining smaller DNA base sub-units of these large structures. In particular, adenine has been the focus of much of these efforts. The involvement of the optically dark, repulsive $\pi\sigma^*$ surfaces (shown in **Figure 5.1**) at the hetero-atom co-ordinates (amino and azole) as viable relaxation mechanisms have been the focus of this particular piece of work. Initial studies described in the proceeding sections were aimed at investigating the photodissociation of adenine following

excitation at 266 nm using a nanosecond (ns) and femtosecond (fs) laser system, as well as the very first time-resolved H elimination results from adenine, 9-methyladenine and 6-dimethylaminopurine and VMI imaging studies of these species.

A more substantial discussion to adenine is presented in the introduction. As a result, the following section presents only the most relevant studies related to this work. The energetic threshold at which the πσ* surface with regard to the N^9-H co-ordinate becomes active is still a matter of some debate. Stolow and co-workers[45-47], using time-resolved photoelectron spectroscopy (TR-PES) following excitation at 266 nm, interpreted differences in the observed photo-electron spectra between 9-methyl adenine and N^9-H adenine as being indicative of the participation of this πσ* PES at this wavelength. However, when the pump wavelength was altered to 250 nm this channel was seen to disappear. This was attributed to enhanced vibrationally mediated coupling between the ππ* and πσ* states at 250 nm, with no such enhancement for the coupling between the ππ* and πσ* states at 266 nm. Rydberg tagging experiments by Ashfold *et al.*[53] clearly showed an onset of a high KE H elimination channel following excitation at ≤ 233 nm, centred at ≈ 9000 cm^{-1}, highly suggestive of the participation of the πσ* PES at these wavelengths. Very recent calculations by Conti *et al.*[173] suggest that the πσ* surface should become energetically accessible with excitation energies ≤ 221 nm.

Domcke and Sobolewski's calculations[38] identified πσ* surfaces at the azole (N^9-H) co-ordinate and at the amino (N^{10}-H) co-ordinate. The adenine –

thymine base pair studies by Schultz and co-workers[74-77] implicate H-transfer mechanisms as being involved in relaxation following optical excitation. Since *in-situ* the N^{10}-H co-ordinate of adenine is actively involved in hydrogen bonding between the DNA bases, whilst the N^9 is now bonded to the sugar phosphate moiety, it is surprising that in the literature the H elimination channel from the N^{10}-H co-ordinate is largely overlooked. The πσ* surface, with respect to the N^{10}-H co-ordinate, has very recently been predicted to become active following excitation at wavelengths ≤ 206 nm by Conti *et al.*[173].

The mixed conclusions drawn from experimental and theoretical efforts have left the participation of the πσ* PES's in one of nature most important molecules a matter of great debate. What follows is our efforts to try and understand the extent of πσ* participation in the photochemistry of adenine and derivatives thereof using both ns and fs light pulses at excitation wavelengths of both 266 nm and 200 nm.

5.2 Power Dependence Studies at 266 nm

Laser fluence studies on the appearance of adenine (for the remainder of this chapter adenine shall be referred to as Ade) parent ion signal and H^+ signal were carried out with both a ns and fs light source. The measured signal for a particular ion, I, can be described by the absorption cross section, σ, the laser fluence, F, and the photon order, n.

$$I = \sigma \cdot F^n \qquad (5.1)$$

From equation 5.1, one can see that plotting the natural log of the signal intensity vs. the natural log of the laser fluence yields a plot with a gradient equal to the number of photons required for ionisation, n.

By using different temporal length laser pulses, the observation "time-window" that dynamic processes contribute to the signal may be studied. In the fs measurements, only processes occurring within the temporal width of the pulse may contribute to the signal, that is, only dissociative processes yielding H on a timescale comparable to the ≈ 120 fs pulse duration are detected. In the ns measurements this "time-window" is much larger, since the pulse duration is greater than the timescales expected for slower internal conversion (IC ≈ 1.2 ps[43,47,51]) which can lead to statistical unimolecular decay. As such using a ns laser source enables us to probe H from direct dissociation and statistical unimolecular decay, whilst with fs pulses only direct dissociation can be probed.

5.2.1 Power Dependence Experimental

A pulsed ns Spectra-Physics GCR series Nd:YAG laser's output was frequency quadrupled through two successive KDP crystals to form light at 266 nm (fundamental 1064 nm). Pulse durations of 4-5 ns were achieved with pulse energies in the range of 1 – 15 mJ. The output of the fs laser (described previously) was frequency tripled, to form light at 266 nm. Pulse durations of approximately 120 fs were achieved with pulse energies in the range of 1 – 30 μJ.

Ade was heated to 240-250°C and co-expanded with Ar through a purposely built stainless steel oven to form an effusive beam. This was subsequently skimmed and intercepted by one of the laser beams (as described above) in the centre of a repeller and accelerator electrode (V_R = 3600 V and V_A = 2800 V). Ions generated (Ade$^+$ and H$^+$) through multiphoton ionisation, were accelerated along a 500 mm field free region and detected upon impact with an MCP. The MCP output was monitored on an oscilloscope and processed using a program running LabVIEW.

5.2.2 Nanosecond Results

Ade$^+$ and H$^+$ signals were recorded over a range of different pulse powers, 7 and 15 mJ/pulse, corresponding to laser intensities between $\approx 1\times10^{11}$ W/cm^2 and $\approx 3\times10^{11}$ W/cm^2. Plots showing the natural log of the signal intensity vs. the natural log of the pulse power for both Ade$^+$ and H$^+$ are shown in **Figure 5.2**. The measured gradients of 1.1 for Ade$^+$ and 2.7 for H$^+$ suggest that photon orders for ionisation are 1 and 3 respectively. Excitation and subsequent ionisation under such a temporally broad ns laser pulse allows both direct H elimination and any H signal due to IC followed by statistical unimolecular decay to contribute to the observed signal.
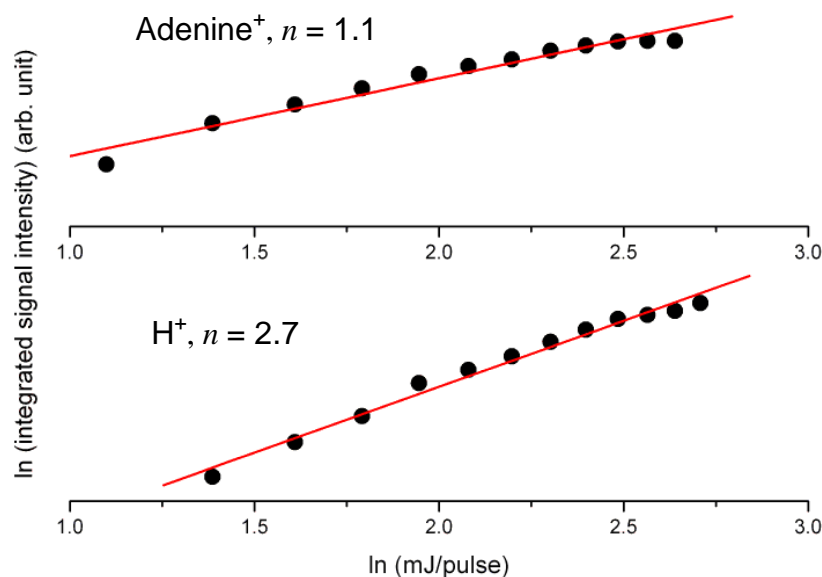
Figure 5.2, plots of the natural log of ns laser signal intensity vs the natural log of pulse power. The gradient yields the photon order (n). (top) n of Ade$^+$ signal determined as 1.1 (bottom) n of H$^+$ determined as 2.7.

5.2.3 Femtosecond Results

Ade$^+$ and H$^+$ signals were recorded over a range of different pulse powers, 7 and 30 µJ/pulse, corresponding to laser intensities between $\approx 7\times10^{12}$ W/cm^2 and $\approx 3\times10^{13}$ W/cm^2. Plots showing the natural log of the signal intensity vs. the natural log of the pulse power for both Ade$^+$ and H$^+$ are shown in **Figure 5.3**. The measured gradients of 0.8 for Ade$^+$ and 2.6 for H$^+$ suggest that photon orders for ionisation are 1 and 3 respectively. Of important note is that observation of H$^+$ is suggestive that the process responsible for its generation is ultrafast (< 120 fs), since both initial excitation and subsequent ionisation must occur within the temporal duration of the fs laser pulse.
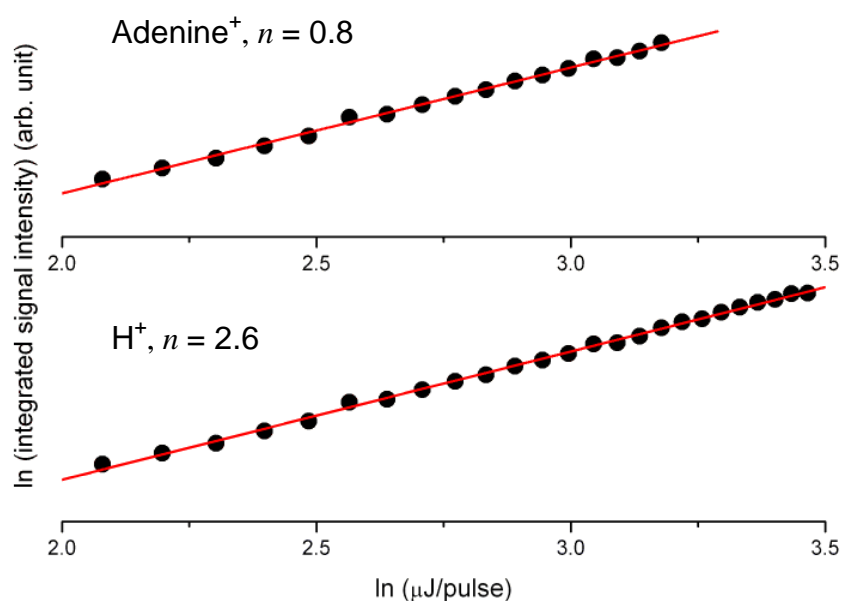
Figure 5.3, plots of the natural log of fs laser signal intensity vs the natural log of pulse power. (top) *n* of Ade⁺ signal determined as 0.8 (bottom) *n* of H⁺ determined as 2.6.

5.2.4 Discussion of Power Dependence Studies at 266 nm

The IP of adenine is known to be 8.48 eV[174]. As such 2 photons are required to ionize Ade and therefore a photon order of 2 is anticipated. This does not agree with the measured photon orders of 1 for both ns and fs measurements. This suggests that either the initial excitation to the optically bright ππ* state or the ionisation step is saturated due to the large photon density, resulting in a photon order that is dependant upon only one of the steps. A similar saturation effect has previously been observed in fs Ade⁺ power dependence measurements[175].

The IP of H is known to be 13.60 eV[176]. Coupled with the fact that H must initially be formed by a photo-initiated process, a photon dependence of 4 is

expected (3 photons at 266 nm are required to ionize H). Again, in both ns and fs measurements, the photon dependence is 1 less than anticipated. This reduced photon order lends itself to the saturation of the ππ* excitation. As such the, power dependence is reflected in the ionisation of H, which requires 3 photons.

In the ns H data, we can conclude that both slow IC/statistical decay and direct dissociation via the πσ* surface is contributing to the observed signal. For the fs measurements, signal contribution via the slow IC/statistical decay mechanism is not possible, since this process occurs on a timescale far greater than the pulse duration. As a result, only a very fast process may contribute to the signal (≈ 100 fs). This, coupled with the measured photon dependence of approximately 3 for the H^+, suggests H is being detected which is formed through active participation of the πσ* PESs [177].

A substantially smaller H^+ yield is observed in the fs experiments compared to the ns experiments. This can be rationalised as being due to low laser intensities at the wings of the fs pulse i.e. initial excitation of Ade occurs at the front end of the fs pulse, dissociation occurs over ≈ 100 fs, followed by ionisation by the rear end of the pulse.

Figure 5.4 shows that for the ns experiments, the intensities of both the Ade^+ and H^+ are equal at a power intensity of ≈ 2.5×10^{11} W/cm^2 whilst in the fs measurements this equivalence point is not reached until intensities of ≈ 2.5×10^{13} W/cm^2. This higher intensity is as expected, as ionisation of the H can

only occur at the rear end of the pulse where the intensity is much lower and therefore greater power densities are needed to generate substantial H$^+$ signal.
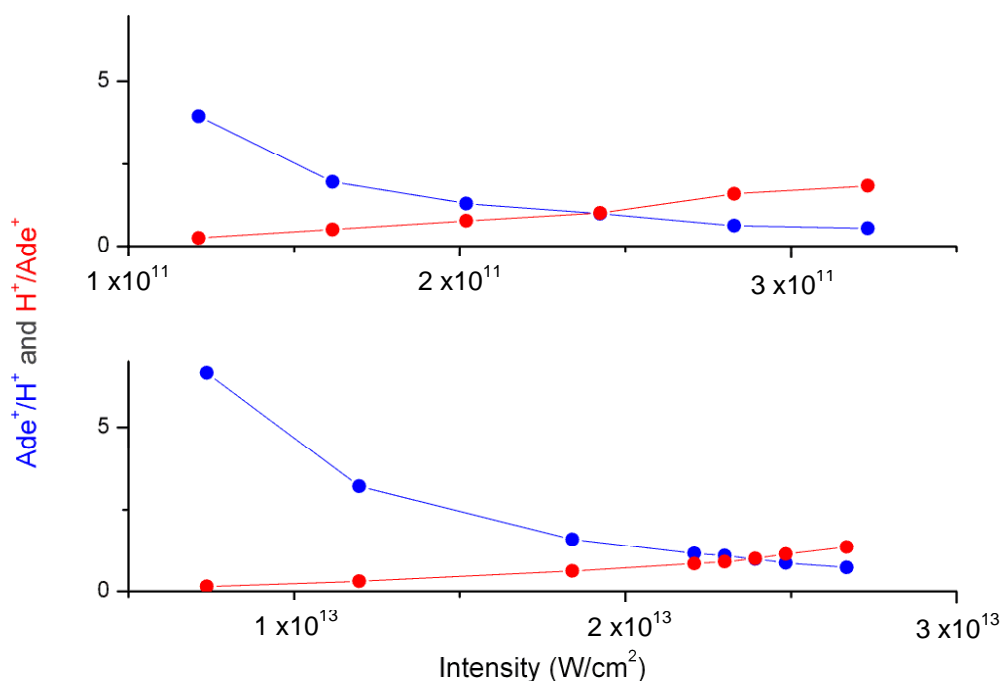
Figure 5.4, plots showing relative ratio of Ade$^+$ signal to H$^+$ (blue) and H$^+$ signal to Ade$^+$ signal (red) for ns (top) and fs (bottom) measurements. NOTE- plots are on different intensity scales.

It is not possible to assign with certainty the source of the H$^+$ signal. But the observed photon dependence of approximately 3 and the ultrafast nature of this signal (in the fs measurements) does at least hint at some dynamical process, which may involve the repulsive $\pi\sigma^*$ surface. It is not possible to eliminate dissociative multi-photon ionisation as the source of H$^+$, where optical excitation to some repulsive cationic state is effectively generating the observed H$^+$ signal.

_____

5.2.5 Time-resolved Mass Spectrometry at 266 nm

In an effort to further characterise the nature of the H^+ signal observed in Ade following photo-excitation at 266 nm, pump-probe TR-MS experiments were carried out[178], pumping at 266 nm and probing 243.1 nm to resonantly ionise the H photo-product. Complimentary Ade^+ transients were also collected.

5.2.6 TR-MS Experimental

Briefly, Ade was heated to 250^oC and co-expanded with He through an Even-Lavie valve to form a supersonic jet expansion. This was subsequently skimmed and intercepted by the co-linearly aligned pump and probe laser pulses in the centre of a repeller and accelerator under VMI focussing conditions. Following photodissociation with the pump, and subsequent ionisation with the probe, the ionised fragments were accelerated along a 500 mm flight tube. At the terminus, these ions were detected by an MCP. The yield of H^+/Ade^+ signal as a function of time delay between pump and probe pulses was recorded and analysed on a purposely built LabVIEW program.

5.2.7 TR-MS Results

Figure 5.5 shows the observed H^+ transient from Ade, pumping with 266nm. The lack of an exponential rise at positive delay times strongly suggests that no H elimination is occurring following excitation at 266 nm.

_____
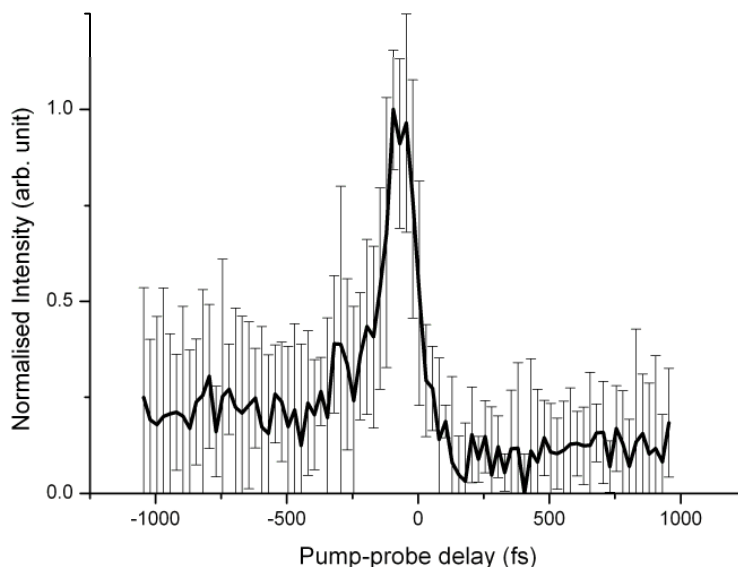
Figure 5.5, H⁺ transient from Ade, pumping with 266 nm and probing with 243.1 nm. Error bars shown correspond to a 95 % confidence limit.

The peak maximum located near time zero is most likely due to multi-photon ionisation through population of some short lived resonant state ($\leq$ 100 fs). The observed baselines on either side of the peak are shown to be markedly different. When the pump precedes the probe the H⁺ signal is the same magnitude as the signal from probe alone. When the probe precedes the pump the signal increases, indicative of a probe-pump signal. Fitting of this is not possible due to the large uncertainties in the experimental data points and the convolution of this exponential rise with the apparent multi-photon component.
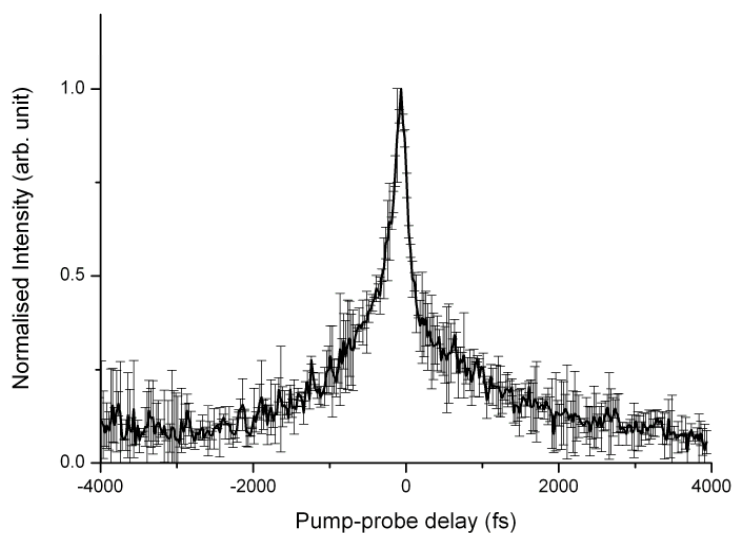
Figure 5.6, Ade⁺ transient after pumping with 266 nm and probing with 243.1 nm. Error bars shown correspond to a 95 % confidence limit.
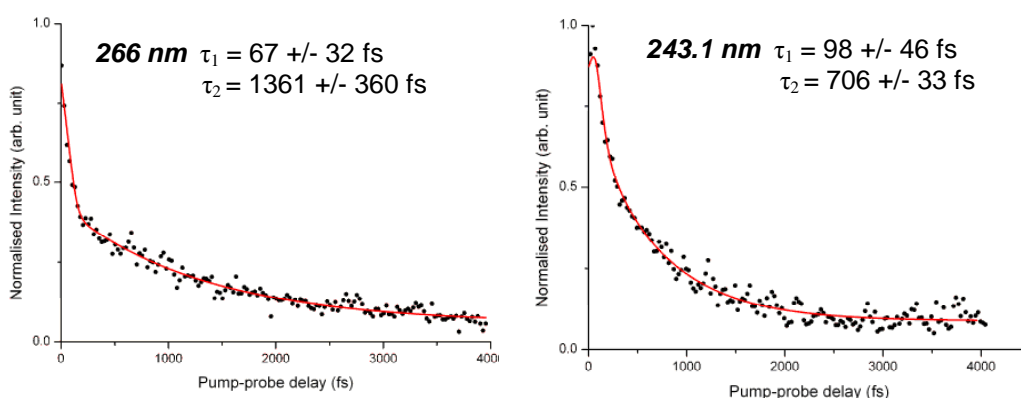
Figure 5.7, fits to Ade⁺ transient with double decay functions. Left shows fits when the pump (266 nm) arrives first and right when probe (243.1 nm) arrives first.

Figure 5.6 shows the Ade$^+$ transient recorded across positive and negative pump/probe delays. Figure 5.6 has been re-plotted in figure 5.7 to show on separate plots the data corresponding to when the pump precedes the probe (LHS) and when the probe precedes the pump (RHS). Fitting these transients with a biexponential decay function yields time constants of τ_1 = 67 +/- 32 fs and τ_2 =1361 +/- 360 fs when pump precedes the probe, and τ_1 = 98 +/- 46 fs and τ_2 = 706 +/- 33 fs when probe precedes the pump. These values for the

pump/probe decays agree with those previously reported in the literature[43,45-46,51]. The long time-constant has previously been identified as an internal conversion mechanism from $\pi\pi^* \rightarrow n\pi^* \rightarrow S_0$, whilst the fast time-constant has previously been assigned to direct dissociation along the $\pi\sigma^*$ surface.

5.2.8 Conclusion Regarding Hydrogen Elimination from Adenine Following Excitation at 266 nm

Although the fluence measurements imply an ultrafast H elimination channel in Ade following excitation at 266 nm[177], in line with what would be expected from a dissociative $\pi\sigma^*$ PES, the subsequent time-resolved measurements[178] suggest that no (or at best very little) neutral H is eliminated. This may however be hindered by the fact that Ade itself has a strong UV absorption cross section at 243.1 nm[179], which may reduce the photon flux available to ionise any formed neutral H. It seems more likely though that H is formed from a dissociative ionisation mechanism at the multiphoton level. This model would also account for other apparent observations of $\pi\sigma^*$ dynamics at this wavelength [43,45,47,51,76].

5.3 Velocity Map Ion Imaging of Hydrogen from Adenine and Methyl Derivatives

Excitation at 200 nm results in wave-packet propagation above the CI's for the $\pi\sigma^*$ surfaces at both the N^9 and N^{10} heteroatom co-ordinates in Ade and as

such the total yield of H elimination may be considered a linear combination of these two paths.

To separate these two distinct dynamical pathways, VMI studies of H elimination from Ade, 9-methyladenine (9-MA) and 6-dimethylaminopurine (6-DMAP) were carried out[178]. In 9-MA the H elimination channel with respect to this co-ordinate is blocked, essentially allowing only the N^{10} co-ordinate to contribute to any observed direct H elimination channels. Similarly in the 6-DMAP measurements, where the N^{10} co-ordinate is methylated, only H elimination via the N^9 co-ordinate may be observed.

5.3.1 Experimental

Briefly, Ade (250°C), 9-MA (200°C) and 6-DMAP (170°C) were independently heated and co-expanded with He through an Even-Lavie valve to form a supersonic jet expansion. This was subsequently skimmed and intercepted by the co-linearly aligned pump and probe laser pulses in the centre of a repeller and accelerator electrode under VMI focussing conditions. Following photodissociation with the pump, and subsequent 2+1 REMPI of the neutral H product with the probe ($\approx$ 2.5 ps later), the ionised fragments are accelerated along a 500 mm flight tube. At the terminus, these ions are detected by a vacuum imaging detector (VID). The images of the H^+ were recorded and analysed on a purposely built LabVIEW program.

5.3.2 Results
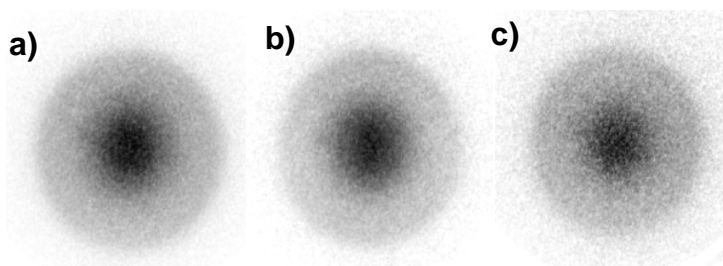
Figure 5.8, raw VMI images of H⁺ following photodissociation at 200 nm of a) Ade; b) 9-MA and c) 6-DMAP. The delay between pump and probe pulses set at 2500 fs

Raw images of H⁺ Ade, 9-MA and 6-DMAP are shown in **Figure 5.8**. Each KE spectrum shows a bimodal distribution. Maxima appear at ≈ 1000 cm⁻¹ and ≈ 8000 - 9000 cm⁻¹, as depicted in **Figure 5.9**. The observed KE spectra match very well with previous TKER measurements at similar wavelengths in Ade[53].
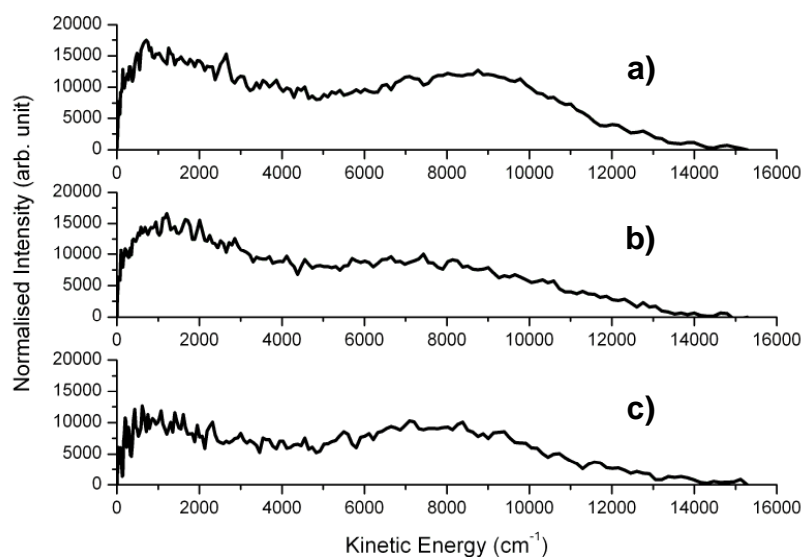
Figure 5.9, KE spectra from a) Ade; b) 9-MA and c) 6-DMAP

Separating the two KE channels enables us to model both the low and high KE channels. The low KE pathway is modelled with an equation of the form shown in equation 5.2.

$$y = f \cdot (KE)^{1/2} \cdot \left(e^{KE/W} \right)^{-1} \qquad (5.2)$$

where y is the intensity at a given KE, f is a amplitude scaling factor and W is a scaling factor representing the decay of the low KE channel at higher KE's. The high KE channel is simply modelled using a Gaussian function.
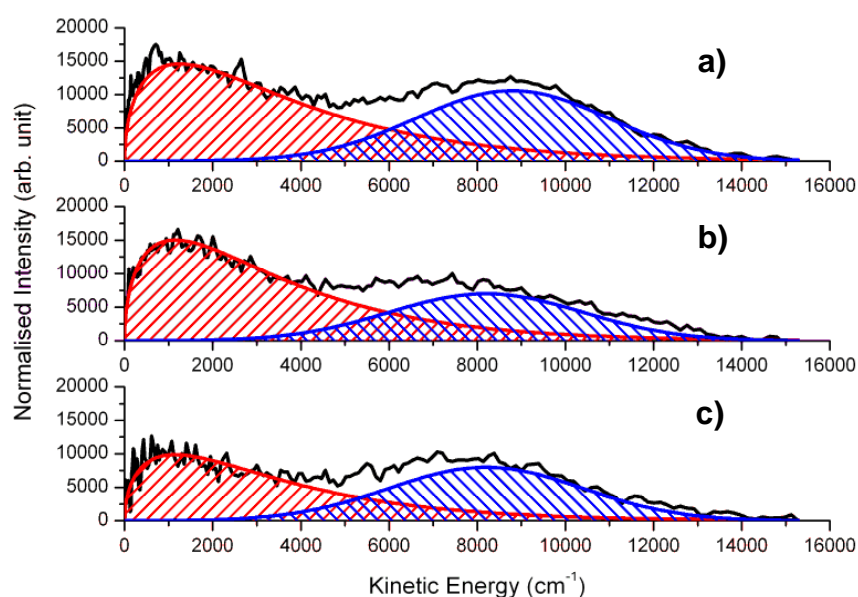
Figure 5.10, kinetic energy spectra from a) Ade; b) 9-MA and c) 6-DMAP. Fits to high KE (blue) and low KE (red) channels indicated on each plot.

Figure 5.10 depicts the fits to the high KE and low KE channels in Ade, 9-MA and 6-DMAP using the functions described. The high KE channel in the Ade is likely due to a combination of H signal from both the N^9 and N^{10} dissociative πσ* PESs, whilst the high KE channel in 9-MA is due to the N^{10} co-ordinate and the high KE channel in 6-DMAP is from the N^9 co-ordinate. The low KE channel in all three species is either due to some multiphoton process or from photodissociation leading to excited state fragment products (minus H), with less energy available to H as KE. With the reduced KE, these latter processes

are expected to be slow relative to the direct dissociation mechanisms via the

πσ* PES, since KE is proportional to velocity. When the KE is low, the

momentum of the wavepacket is also low and hence dissociation will occur on

a longer timescale.

Species	High KE : Low KE
adenine	1:1.3
9-methyladenine	1:1.8
6-dimethylaminopurine	1:1.0

Table 5.1, ratios of integrals of fits to the high KE channel vs. low KE channel in Ade, 9-MA and 6-DMAP.

Table 5.1 shows the relative ratios of the integrals of the high and low KE

channels taken from the KE spectra in Ade and the methylated derivatives.

These measured ratios clearly show a large proportion of high KE channel in

each species, indicative of substantial participation of the πσ* PES.
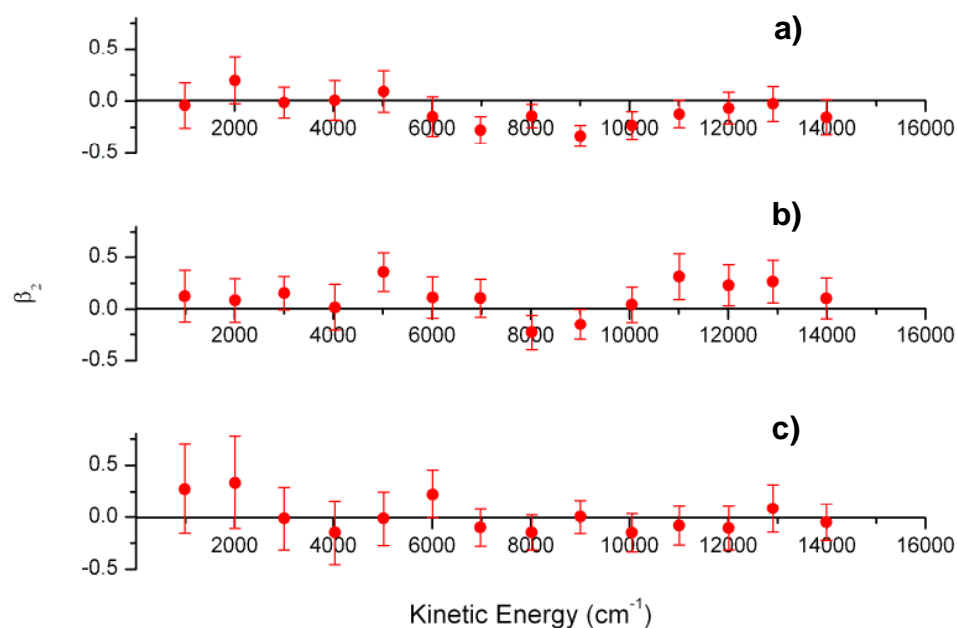
Figure 5.11, measured β_2 parameters from a) Ade; b) 9-MA and c) 6-DMAP following photodissociation at 200 nm.

Figure 5.11 shows the measured β_2 parameters for Ade, 9-MA and 6-DMAP. In Ade, slightly negative values are observed in the high KE channel. This is in qualitative agreement with the measured anisotropy parameters in Ade following dissociation from a higher lying $\pi\pi^*$ surface[53], which at 200 nm is energetically accessible. The observation of anisotropy is indicative that this high KE channel is occurring on an ultrafast timescale, since the photodissociation must occur on a timescale that is less than the rotational period of the parent molecule.

5.4 Time-Resolved Hydrogen Elimination from Adenine and Methyl Derivatives Following Excitation at 200 nm

The VMI images of Ade, 9-MA and 6-DMAP showed a bimodal distribution. The high KE channel is expected to appear on a fast timescale following dissociation, whilst the low KE channel is expected to appear on a slower timescale. To measure the relative appearance times of these two channels and to assess whether the ratios of the high and low KE channels observed in VMI measurements are reproducible in the time domain, TR-MS studies at 200 nm were completed[178].

Due to the long run times (120 hrs) required to collect TR-VMI transients, these studies have not been completed, as the current valve source is not capable of providing a sufficient sample density over such extended periods.

5.4.1 Experimental

Briefly, Ade (250°C), 9-MA (200°C) and 6-DMAP (170°C) were independently heated and co-expanded with He through an Even-Lavie valve to form a supersonic jet expansion. This was subsequently skimmed and intercepted by the co-linearly aligned pump and probe laser pulses in the centre of a repeller and accelerator electrode under VMI focussing conditions. Following photodissociation with the pump, and subsequent 2+1 REMPI of the neutral H product with the probe, the ionised fragments are accelerated along a 500 mm flight tube. At the terminus, these ions were detected by an MCP. The yield of H^{+} signal as a function of time delay between pump and probe pulses was recorded and analysed on a purposely built LabVIEW program.

5.4.2 Results
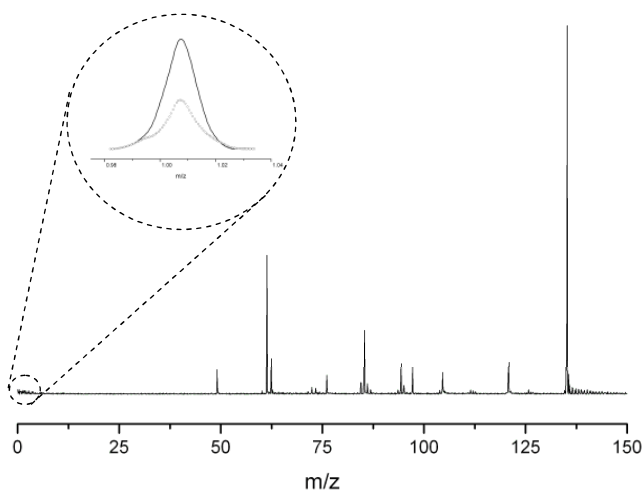
Figure 5.12, representative mass spectrum obtained from Ade. Pump precedes probe by 1000 fs. Inset shows H^{+} signal at positive delays (solid line) and at negative delays (dotted line) recorded at higher voltages on MCP (see proceeding text).

Figure 5.12 shows a typical two colour mass spectrum for Ade following excitation at 200 nm and subsequent probing at 243.1 nm following a time-delay of 1 ps. Under the experimental conditions used to observe Ade$^+$ (as well as other fragments) no H$^+$ is observed. The inset shows the H$^+$ signal both when pump precedes probe (solid line) and when probe precedes pump (dotted line), the latter showing the production of H$^+$ by the probe alone i.e., signal before time zero. The H$^+$ signal is significantly smaller than the Ade$^+$ signal. As a result, to avoid damaging the detector, higher mass signals are gated off and the detector voltages increased to a level capable of producing a workable H$^+$ signal. H$^+$ transients for all species (**Figure 5.13**) showed a clear step indicative of H elimination following excitation at 200 nm.
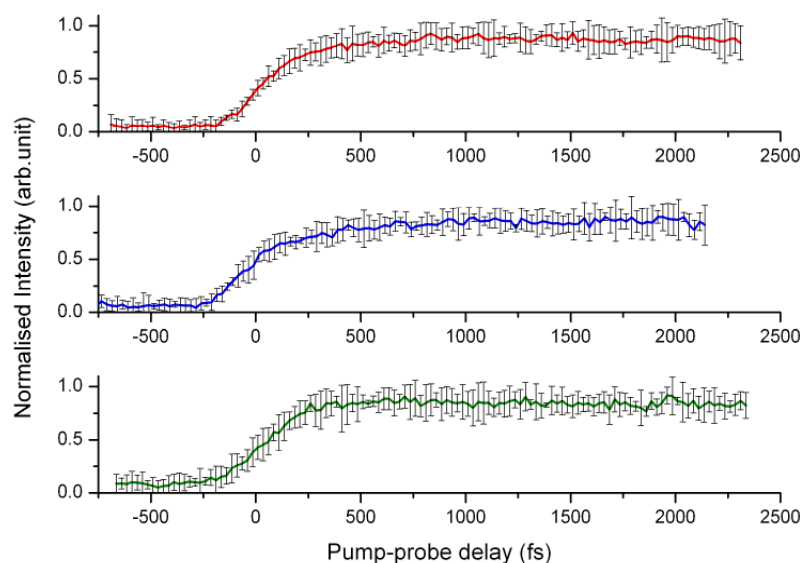
Figure 5.13, H$^+$ transients from Ade (red), 9-MA (blue) and 6-DMAP (green). Error bars shown correspond to a 95 % confidence limit.

Adequate fits to the Ade and 9-MA require two exponential rise functions and a decay component (decaying into negative delays), whilst the 6-DMAP requires a single exponential rise and decay component. The decay component most

likely corresponds to direct formation of H^+ through a short lived state resonant state ($\leq$ 100 fs) accessed through multiple photon absorption. The step functions correspond, in part to direct H elimination via the $\pi\sigma^*$ PESs. The corresponding time constants for these fits are shown in **Table 5.2**, and the fits themselves are illustrated in **Figure 5.14**.

Species	τ_1	τ_2	Ratio ($\tau_1:\tau_2$)
adenine	110 +/- 63 fs (80 %)	265 +/- 135 fs (20 %)	4.0:1
9-methyladenine	95 +/- 48 fs (65 %)	326 +/- 205 fs (35 %)	1.9:1
6-dimethylaminopurine	95 +/- 21 fs (100 %)	-	-

Table 5.2, fitted time constants for the transients shown in Figure 5.13. Relative ratios also shown for completeness.
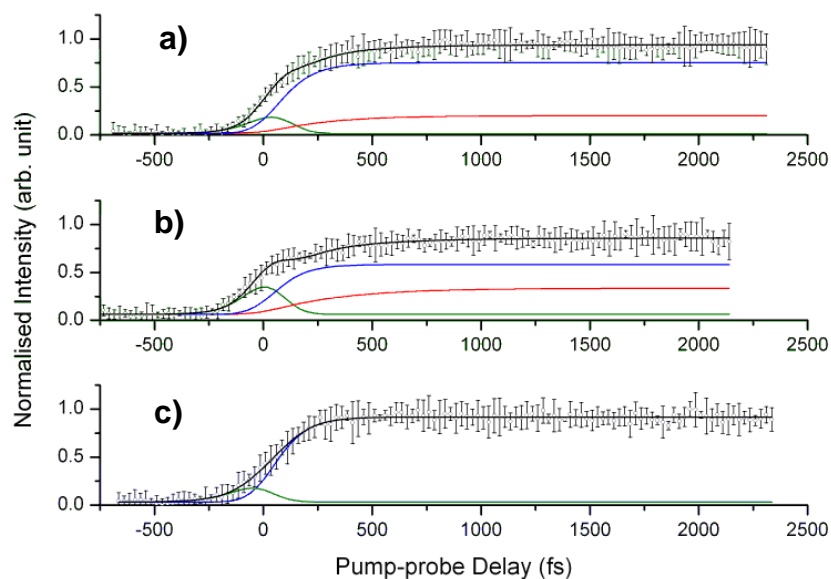
Figure 5.14, fits to a) Ade; b) 9-MA and c) 6-DMAP. Fast exponential rise (blue), slow exponential rise (red) and decay component (green) indicated on each plot. Error bars shown correspond to a 95 % confidence limit.

Complimentary Ade^+ transient data is presented in **Figure 5.15**. Fitting the pump/probe decay with a biexponential decay yields time constants of $\tau_1 = 67$

+/- 44 fs and τ_2 = 412 +/- 102 fs, whilst fitting of the probe/pump decay was only possible with a single time constant of τ_1 = 655 +/- 51 fs, matching very closely with measurements with the 243 nm pump/266 nm probe data presented earlier.
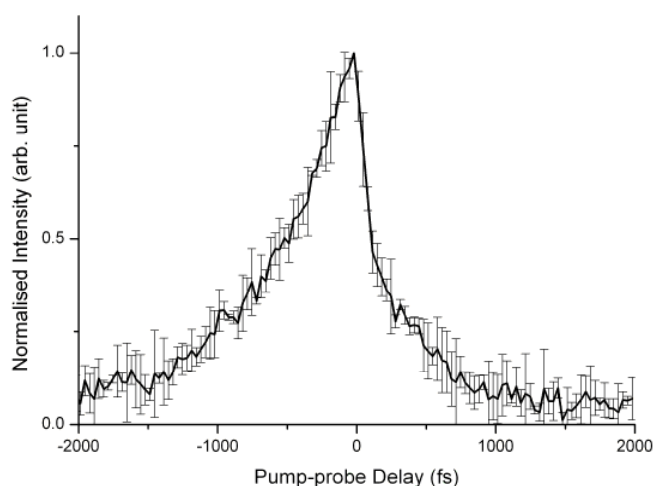
Figure 5.15, Ade$^+$ transient. Error bars shown correspond to a 95 % confidence limit.

5.4.3 Comparison of TR-MS Measurements and VMI Measurements at 200 nm

It is immediately tempting to assign each of the two observed exponential rise time constants (in the H$^+$ transients in Ade) to the two respective KE channels, assuming the high KE channel accounts for the faster of the two time constants. However sufficient differences in the observed ratios in the VMI study and TR-MS study reveal this model to be insufficient.

In the 6-DMAP KE spectra, the ratio of the high KE and low KE channels was seen to be 1:1. Given that fitting of the H$^+$ transients from this species yielded only a single time constant (95 fs) it is clear that both high KE and low KE channels must be appearing on extremely similar timescales. Since H

elimination via the amino group is blocked by methylation, and previous studies in deuterated phenol[171, 172] (at the C-H co-ordinates) showed that significant low KE H signal is still observed, it seems most likely that the source of these two channels is the N^9-H co-ordinate.

In 9-MA, where the N^9-H co-ordinate is blocked, allowing investigation of the N^{10}-H co-ordinate, VMI measurements reveal that the low KE channel dominates over the high KE channel (by a factor of 1.8). For adequate fitting of the H^+ transients a second exponential rise is required (326 fs), with half the amplitude of the faster exponential rise (95 fs). Assignment of the entire low KE channel to this slower time constant produces the wrong ratio of time constants to suitably reproduce the observed H^+ transients. In 6-DMAP, as well as previous experiments in phenol[171] it has been shown that there is potential for a low KE channel with a fast time constant. Assuming that ≈ 50 % of the low KE channel is formed on a similar timescale to the high KE channel the observed ratio of fast time constant (τ_1, 95 fs) to slow time constant (τ_2, 326 fs) can be reproduced. This suggest that upon excitation at 200 nm three separate channels are contributing to H elimination, direct dissociation via the πσ* surface at the amino co-ordinate occurring in 95 fs, resulting in high KE H. The two remaining channels result in low KE H, but are occurring on very different time-scales to one-another, most likely through either multi-photon excitation and subsequent IC or through formation of the electronically excited radical co-product, one of which is occurring in ≈ 95 fs, the other in 326 fs.

Direct deconvolution of the VMI and H^+ transients to yield information on the contributing mechanisms in Ade directly would be difficult, but based upon the assumption that the behaviour exhibited by Ade will be a linear combination of the two substituted systems, investigation into the involvement of the amino and azole co-ordinate following excitation at 200 nm is possible.

The observed ratio in Ade of high KE to low KE is revealed to be 1:1.3. By taking a weighted sum of the KE ratios in 9-MA and 6-DMAP, with weightings of 0.91 and 1.00 respectively, reproduces the observed ratio in Ade. This indicates almost equal contribution of the amino and azole co-ordinates. To further check the applicability of these conclusions, the obtained weightings for the substituted systems were applied to the time constants for Ade. These yielded an expected contribution of 83 % to the fast channel and 17 % to the slow channel, in very close agreement with the observed ratio of 4:1, fast to slow, as shown in table 5.2.

Further to this, greater interpretation may be drawn from these results with regard to the sub channels. Given the relative contributions to the Ade transient from the arguments drawn above, it is clear that ≈ 50 % of the total H signal is originating from πσ* dissociation. Furthermore a considerable proportion of this is from the amino co-ordinate and occurs in < 100 fs. A fast low KE channel, occurring from both the amino and azole co-ordinate on a similar timescale to the πσ* mechanisms is also observed. The lack of a slow channel in the H^+ transient from 6-DMAP suggests that the observed slow component in Ade (≈ 300 fs) is purely originating from the amino co-ordinate.

5.5 Conclusions

Power dependence measurements presented here, using fs pulses at 266 nm[177] initially suggested the participation of the $\pi\sigma^*$ PESs. However subsequent H^{+} transient measurements following excitation at 266 nm and probing with 243.1 nm radiation strongly imply that little or no participation of the $\pi\sigma^*$ PESs in the dissociation dynamics is occurring[178]. This conclusion does not rule out the possibility of other ultrafast mechanisms (not resulting in H elimination) occurring. This would account for previous ultrafast processes being reported at this wavelength[43,45-47,51,76].

Ade[+] transients showed a bi-exponential decay following excitation at 266 nm, the longer decay constant ($\approx$ 1300 fs) consistent with measurements in the literature corresponding to an IC mechanism[43,45-46,51]. Although the fast component to the fit also agrees well with these measurements, it is difficult to assign with any great confidence the timescale of this faster channel as the instrument response function is broad relative to this.

Following excitation at 200 nm, combined VMI and TR-MS measurements[178] strongly imply the participation of both the amino and azole $\pi\sigma^*$ PESs in the dissociation dynamics in Ade. The $\pi\sigma^*$ PESs were seen to directly dissociate in $\approx$ 100 fs, resulting in both high KE H and a similar sized population of low KE H. A slower mechanism was also observed, attributed to the N[10] co-ordinate which formed H in $\approx$ 300 fs, the longer timescale for this may suggest either electronically excited radical photodissociation products (with corresponding

low KE H) or an IC mechanism followed by statistical unimolecular decay is responsible. The observation of H elimination via the amino co-ordinate further supports the H transfer relaxation mechanisms proposed in base pairs following UV excitation [74-75].

Although the studied methylated Ade derivates will posses distorted PES (with respect to the bare adenine molecule) these results suggest that these species may be effectively used to model the dissociation dynamics of Ade itself.

5.6 Future Work

Each VMI image presented here was the summed signal integrated over a 1 hour period. As such the corresponding TR-VMI transients would require run times of 120 hours. Work is currently underway to develop a valve source capable of maintaining a suitable sample density for these extended periods to enable TR-VMI studies of these species to be carried out. This would enable further characterisation of both the observed high KE and low KE populations.

Future installation of a new UV OPA will enable studies throughout the wavelength range between 266 nm and 200 nm. This will enable us to determine the energetic onset of the $\pi\sigma^*$ PES on both the azole and amino coordinate. Studies into methyl elimination from 9-MA are planned which will model the breaking of the N^9-C bond which is present in adenine bound in DNA.

6. Review

Chapter 2 presented the successful design, construction and calibration of a TR-VMI. The photodissociation of HBr was the first system studied using this new instrument. Following population of the A-band at 200 nm, different dissociation timescales for channels leading to ground state Br ($^2P_{3/2}$) and spin excited Br ($^2P_{1/2}$) were observed. Counter intuitively, it appears that the $^2P_{1/2}$ channel dissociates faster than the higher KE $^2P_{3/2}$ channel, highlighting the need for theoretical work to try and fully understand this photodissociation event.

Chapter 3 presented the first TR-VMI measurements from NH_3[167]. Separating the TR-VMI transients into KE regions corresponding to different quanta of excitation in the bending vibrational mode (v_2) of the corresponding $\tilde{X}^2B_1$ state NH_2 co-fragment showed dissociation time-constant are dependant upon the degree of internal excitation of the NH_2 fragment. Dissociation into the highest KE channel is expected to occur in < 50 fs, in good agreement with experimental measurements[98] and recent calculations[115]. The measured negative anisotropy parameter across the entire KE spectrum strongly suggests very little rotational excitation in the photo-products. The lowest KE channel, where electronically excited $\tilde{A}^1A_2$ state is energetically possible, has an extended dissociation timescale, suggestive of adiabatic dissociation contributing to the observed signal at low KEs.

Chapter 4 presented TR-MS and VMI measurements of the photodissociation of 5-membered ring models of adenine. VMI images clearly show a high KE channel in all imidazole species consistent with what is expected from dissociation via the πσ* surfaces. Direct comparison of the photodissociation timescales of pyrrole (107 +/- 33 fs) and imidazole (53 +/- 48 fs) show significant difference, the only plausible reasoning between this difference is that the dissociative πσ* surface in imidazole lies ≈ 3000 cm^{-1} higher in energy than in pyrrole, and as such has a steeper gradient leading to faster wavepacket motion across this PES. The photodissociation of methyl imidazole derivatives have been observed to dissociate on longer timescales (~ 70 fs longer) than the bare imidazole suggesting that as internal degrees of freedom increase, the dissociation timescales along the πσ* PESs also increase. Studies on 1-methylimidazole also strongly suggest a minor C-H channel contributing to the photodissociation dynamics following excitation at 200 nm. This is reconciled as occurring along another πσ* surface with respect to a C-H co-ordinate predicted by Barbatti *et al.*[94].

Chapter 5 discussed ns and fs power dependence ionisation measurements of Ade at 266 nm[177]. The photon dependence of Ade$^+$ and H$^+$ were measured. By utilising fs laser pulses, only processes yielding H$^+$ within the envelope of the pulse could contribute to the signal. The observation of a photon dependence suggestive of the ionisation of neutral H in the fs measurements was initially interpreted as evidence of H elimination via the πσ* surfaces at this wavelength. Subsequent TR-MS measurements at 266 nm[178] however strongly suggest that this is not the case, although these measurements may be

hampered by the large absorption cross section of Ade at 243.1 nm. However, it is more likely that H$^+$ signal at 266 nm is due to dissociative multiphoton ionisation. Chapter 5 also presented the first time-resolved H elimination measurements from Ade, 9-MA and 6-DMAP[179], using a combined TR-MS and VMI approach, providing evidence of the participation of both the amino and azole πσ* surfaces in the photodissociation dynamics following excitation at 200 nm. A fast high KE channel and a fast low KE channel were identified (95 – 110 fs) while a second, slower low KE channel (265 – 326 fs) was also identified as being active at exclusively the amino site.

7. References

(1)   Zewail, A. *J. Phys. Chem. A.* **2000**, *104*, 5660.
(2)   Zewail, A. *J. Phys. Chem.* **1993**, *97*, 12427.
(3)   Nye, M. *J. Comput. Chem.* **2007**, 98.
(4)   Wynne-Jones, W.; Eyring, H. *J. Chem. Phys.* **1935**, *3*, 492.
(5)   Evans, M.; Polanyi, M. *Trans Faraday soc.***1935**, *31*, 875.
(6)   Lamb, W. *Phys. Rev.* **1964**, *134*, 1429.
(7)   Hargrove, L.; Fork, R.; Pollack, M. *Appl. Phys. Lett.* **1964**, *5*, 4.
(8)   Moulton, P. *J. Opt. Soc. Am. B.* **1986**, *3*, 125.
(9)   Herrmann, J. *J. Opt. Soc. Am. B.* **1994**, *11*, 498.
(10)   Carley, R.; Heesel, E.; Fielding, H. *Chem. Soc. Rev.* **2005**, *34*, 949.
(11)   Laarmann, T.; Shchatsinin, I.; Singh, P.; Zhavoronkov, N.; Schulz, C.; Hertel, I. *J. Phys. B.* **2008**, *41*.
(12)   Brixner, T.; Gerber, G. *ChemPhysChem.* **2003**, *4*, 418.
(13)   Ashfold, M.; Howe, J. *Ann. Rev. Phys. Chem.* **1994**, *45*, 57.
(14)   Demtröder, W. *Laser spectroscopy: Basic concepts and instrumentation.* 2nd ed.; Springer-Verlag: Berlin, 1998.pg 466-488.
(15)   Ashfold, M.; Lambert, I.; Mordaunt, D.; Morley, G.; Western, C. *J. Phys. Chem.* **1992**, *96*, 2938.
(16)   Wodtke, A.; Lee, Y. *J. Phys. Chem.* **1985**, *89*, 4744.
(17)   Mordaunt, D.; Lambert, I.; Morley, G.; Ashfold, M.; Dixon, R.; Western, C.; Schnieder, L.; Welge, K. *J. Chem. Phys.* **1993**, *98*, 2054.
(18)   Einstein, A. *Ann. Physik*, **1905**, *17*, 17.
(19)   Blanchet, V.; Lochbrunner, S.; Schmitt, M.; Shaffer, J.; Larsen, J.; Zgierski, M.; Seideman, T.; Stolow, A. *Faraday Discuss.* **2000**, 33.
(20)   Zewail, A. *SCIENCE.* **1988**, *242*, 1645.
(21)   Crespo-Hernandez, C.; Cohen, B.; Hare, P.; Kohler, B. *Chem. Rev.* **2004**, *104*, 1977.
(22)   Saigusa, H. *J. Photochem. Photobiol. C.* **2006**, *7*, 197.
(23)   Daniels, M.; Hauswirt.W. *SCIENCE.* **1971**, *171*, 675.
(24)   Serrano-Andres, L.; Merchan, M. *J. Photochem. Photobiol. C.* **2009**, *10*, 21.
(25)   Broo, A. *J. Phys. Chem. A.* **1998**, *102*, 526.
(26)   Serrano-Andres, L.; Merchan, M.; Borin, A. *PNAS.* **2006**, *103*, 8691.
(27)   Yarkony, D. *Acc. Chem. Res.* **1998**, *31*, 511.
(28)   Perun, S.; Sobolewski, A.; Domcke, W. *Mol. Phys.* **2006**, *104*, 1113.
(29)   Barbatti, M.; Lischka, H. *J. Phys. Chem. A.* **2007**, *111*, 2852.
(30)   Zechmann, G.; Barbatti, M. *Int. J. Quant.* **2008**, *108*, 1266.
(31)   Nielsen, S.; Solling, T. *ChemPhysChem.* **2005**, *6*, 1276.
(32)   Barbatti, M.; Lischka, H. *J. Am. Chem. Soc.* **2008**, *130*, 6831.
(33)   Marian, C. *J. Chem. Phys.* **2005**, *122*.
(34)   Serrano-Andres, L.; Merchan, M.; Borin, A. *Chem. -Eur. J.* **2006**, *12*, 6559.
(35)   Sobolewski, A.; Domcke, W. *Eur. Phys. J. D.* **2002**, *20*, 369.
(36)   Perun, S.; Sobolewski, A.; Domcke, W. *J. Am. Chem. Soc.* **2005**, *127*, 6257.
(37)   Chung, W.; Lan, Z.; Ohtsuki, Y.; Shimakura, N.; Domcke, W.; Fujimura, Y. *Phys. Chem. Chem. Phys.* **2007**, *9*, 2075.
(38)   Perun, S.; Sobolewski, A.; Domcke, W. *Chem. Phys.* **2005**, *313*, 107.

(39)   Kim, N.; Jeong, G.; Kim, Y.; Sung, J.; Kim, S.; Park, Y. *J. Chem. Phys.* **2000**, *113*, 10051.

(40)   Blancafort, L. *J. Am. Chem. Soc.* **2006**, *128*, 210.

(41)   Luhrs, D.; Viallon, J.; Fischer, I. *Phys. Chem. Chem. Phys.* **2001**, *3*, 1827.

(42)   Plützer, C.; Kleinermanns, K. *Phys. Chem. Chem. Phys.* **2002**, *4*, 4877.

(43)   Kang, H.; Jung, B.; Kim, S. *J. Chem. Phys.* **2003**, *118*, 11336.

(44)   Cohen, B.; Hare, P.; Kohler, B. *J. Am. Chem. Soc.* **2003**, *125*, 13594.

(45)   Ullrich, S.; Schultz, T.; Zgierski, M.; Stolow, A. *J. Am. Chem. Soc.* **2004**, *126*, 2262.

(46)   Ullrich, S.; Schultz, T.; Zgierski, M.; Stolow, A. *Phys. Chem. Chem. Phys.* **2004**, *6*, 2796.

(47)   Satzger, H.; Townsend, D.; Zgierski, M.; Patchkovskii, S.; Ullrich, S.; Stolow, A. *PNAS.* **2006**, *103*, 10196.

(48)   Bisgaard, C.; Satzger, H.; Ullrich, S.; Stolow, A. *ChemPhysChem.* **2009**, *10*, 101.

(49)   Hunig, I.; Plutzer, C.; Seefeld, K.; Lowenich, D.; Nispel, M.; Kleinermanns, K. *ChemPhysChem.* **2004**, *5*, 1427.

(50)   Zierhut, M.; Roth, W.; Fischer, I. *Phys. Chem. Chem. Phys.* **2004**, *6*, 5178.

(51)   Canuel, C.; Mons, M.; Piuzzi, F.; Tardivel, B.; Dimicoli, I.; Elhanine, M. *J. Chem. Phys.* **2005**, *122*.

(52)   Canuel, C.; Elhanine, M.; Mons, M.; Piuzzi, F.; Tardivel, B.; Dimicoli, I. *Phys. Chem. Chem. Phys.* **2006**, *8*, 3978.

(53)   Nix, M.; Devine, A.; Cronin, B.; Ashfold, M. *J. Chem. Phys.* **2007**, *126*.

(54)   Chen, H.; Li, S. *J. Phys. Chem. A.* **2005**, *109*, 8443.

(55)   Chin, C.; Mebel, A.; Kim, G.; Baek, K.; Hayashi, M.; Liang, K.; Lin, S. *Chem. Phys. Lett.* **2007**, *445*, 361.

(56)   Fabiano, E.; Thiel, W. *J. Phys. Chem. A.* **2008**, *112*, 6859.

(57)   Lei, Y.; Yuan, S.; Dou, Y.; Wang, Y.; Wen, Z. *J. Phys. Chem. A.* **2008**, *112*, 8497.

(58)   Kim, N.; Kang, H.; Jeong, G.; Kim, Y.; Lee, K.; Kim, S. *J. Phys. Chem. A.* **2000**, *104*, 6552.

(59)   Kang, H.; Lee, K.; Kim, S. *Chem. Phys. Lett.* **2002**, *359*, 213.

(60)   Ritze, H.; Lippert, H.; Samoylova, E.; Smith, V.; Hertel, I.; Radloff, W.; Schultz, T. *J. Chem. Phys.* **2005**, *122*.

(61)   Nam, S.; Park, H.; Song, J.; Park, S. *J. Phys. Chem. A.* **2007**, *111*, 3480.

(62)   Nam, S.; Park, H.; Ryu, S.; Song, J.; Park, S. *Chem. Phys. Lett.* **2008**, *450*, 236.

(63)   Belau, L.; Wilson, K.; Leone, S.; Ahmed, M. *J. Phys. Chem. A.* **2007**, *111*, 7562.

(64)   Pal, S.; Peon, J.; Zewail, A. *Chem. Phys. Lett.* **2002**, *363*, 57.

(65)   Pancur, T.; Schwalb, N.; Renth, F.; Temps, F. *Chem. Phys.* **2005**, *313*, 199.

(66)   Yamazaki, S.; Kato, S. *J. Am. Chem. Soc.* **2007**, *129*, 2901.

(67)   Schwalb, N.; Temps, F. *Phys. Chem. Chem. Phys.* **2006**, *8*, 5229.

(68)   Schneider, M.; Maksimenka, R.; Buback, F.; Kitsopoulos, T.; Lago, L.; Fischer, I. *Phys. Chem. Chem. Phys.* **2006**, *8*, 3017.

(69)   Kwok, W.; Ma, C.; Phillips, D. *J. Am. Chem. Soc.* **2008**, *130*, 5131.

(70)   Gonzalez-Vazquez, J.; Gonzalez, L.; Samoylova, E.; Schultz, T. *Phys. Chem. Chem. Phys.* **2009**, *11*, 3927.

(71)   Asturiol, D.; Lasorne, B.; Robb, M.; Blancafort, L. *J. Phys. Chem. A.* **2009**, *113*, 10211.

(72)   Serrano-Andres, L.; Merchan, M.; Borin, A. *J. Am. Chem. Soc.* **2008**, *130*, 2473.

(73)   Woutersen, S.; Cristalli, G. *J. Chem. Phys.* **2004**, *121*, 5381.

(74)   Schultz, T.; Samoylova, E.; Radloff, W.; Hertel, I.; Sobolewski, A.; Domcke, W. *SCIENCE.* **2004**, *306*, 1765.

(75)   Samoylova, E.; Schultz, T.; Hertel, I.; Radloff, W. *Chem. Phys.* **2008**, *347*, 376.

(76)   Samoylova, E.; Lippert, H.; Ullrich, S.; Hertel, I.; Radloff, W.; Schultz, T. *J. Am. Chem. Soc.* **2005**, *127*, 1782.

(77)   Gador, N.; Samoylova, E.; Smith, V.; Stolow, A.; Rayner, D.; Radloff, W.; Hertel, I.; Schultz, T. *J. Phys. Chem. A* **2007**, *111*, 11743.

(78)   Crespo-Hernandez, C.; Cohen, B.; Kohler, B. *NATURE* **2005**, *436*, 1141.

(79)   Crespo-Hernandez, C.; Cohen, B.; Kohler, B. *NATURE* **2006**, *441*, E8.

(80)   Kwok, W.; Ma, C.; Phillips, D. *J. Am. Chem. Soc.* **2006**, *128*, 11894.

(81)   Schwalb, N.; Temps, F. *SCIENCE* **2008**, *322*, 243.

(82)   Sobolewski, A.; Domcke, W. *Chem. Phys.* **2000**, *259*, 181.

(83)   Sobolewski, A.; Domcke, W.; Dedonder-Lardeux, C.; Jouvet, C. *Phys. Chem. Chem. Phys.* **2002**, *4*, 1093.

(84)   Barbatti, M.; Vazdar, M.; Aquino, A.; Eckert-Maksic, M.; Lischka, H. *J. Chem. Phys.* **2006**, *125*.

(85)   Vazdar, M.; Eckert-Maksic, M.; Barbatti, M.; Lischka, H. *Mol. Phys.* **2009**, *107*, 845.

(86)   Sellner, B.; Barbatti, M.; Lischka, H. *J. Chem. Phys.* **2009**, *131*.

(87)   Blank, D.; North, S.; Lee, Y. *Chem. Phys.* **1994**, *187*, 35.

(88)   Wei, J.; Kuczmann, A.; Riedel, J.; Renth, F.; Temps, F. *Phys. Chem. Chem. Phys.* **2003**, *5*, 315.

(89)   Wei, J.; Riedel, J.; Kuczmann, A.; Renth, F.; Temps, F. *Faraday Discuss.* **2004**, *127*, 267.

(90)   Cronin, B.; Nix, M.; Qadiri, R.; Ashfold, M. *Phys. Chem. Chem. Phys.* **2004**, *6*, 5031.

(91)   Lippert, H.; Ritze, H.; Hertel, I.; Radloff, W. *ChemPhysChem.* **2004**, *5*, 1423.

(92)   Beames, J.; Nix, M.; Hudson, A. *J. Chem. Phys.* **2009**, *131*.

(93)   Devine, A.; Cronin, B.; Nix, M.; Ashfold, M. *J. Chem. Phys.* **2006**, *125*.

(94)   Barbatti, M.; Lischka, H.; Salzmann, S.; Marian, C. *J. Chem. Phys.* **2009**, *130*.

(95)   Suto, M.; Lee, L. *J. Chem. Phys.* **1983**, *78*, 4515.

(96)   Vaida, V.; Hess, W.; Roebber, J. *J. Phys. Chem.* **1984**, *88*, 3397.

(97)   Vaida, V.; McCarthy, M.; Engelking, P.; Rosmus, P.; Werner, H.; Botschwina, P. *J. Chem. Phys.* **1987**, *86*, 6669.

(98)   Ziegler, L. *J. Chem. Phys.* **1985**, *82*, 664.

(99)   Ziegler, L. *J. Chem. Phys.* **1986**, *84*, 6013.

(100)   Nakajima, A.; Fuke, K.; Tsukamoto, K.; Yoshida, Y.; Kaya, K. *J. Phys. Chem.* **1991**, *95*, 571.

(101)   Henck, S.; Mason, M.; Yan, W.; Lehmann, K.; Coy, S. *J. Chem. Phys.* **1995**, *102*, 4772.

(102)   Henck, S.; Mason, M.; Yan, W.; Lehmann, K.; Coy, S.. *J. Chem. Phys.* **1995**, *102*, 4783.

(103)   Xie, J.; Jiang, B.; Li, G.; Yang, S.; Xu, J.; Sha, G.; Xu, D.; Lou, N.; Zhang, C. *Faraday Discuss.* **2000**, 127.

(104)   Rosmus, P.; Botschwina, P.; Werner, H.; Vaida, V.; Engelking, P.; McCarthy, M. *J. Chem. Phys.* **1987**, *86*, 6677.

(105) Seideman, T. *J. Chem. Phys.* **1995**, *103*, 10556.
(106) Polak, R.; Paidarova, I.; Spirko, V.; Kuntz, P. *Int. J. Quant.* **1996**, *57*, 429.
(107) Dixon, R. *Mol. Phys.* **1996**, *88*, 949.
(108) Dixon, R.; Hancock, T. *J. Phys. Chem. A.* **1997**, *101*, 7567.
(109) Yarkony, D. *J. Chem. Phys.* **2004**, *121*, 628.
(110) Marquardt, R.; Sagui, K.; Klopper, W.; Quack, M. *J. Phys. Chem. B.* **2005**, *109*, 8439.
(111) Nangia, S.; Truhlar, D.; McGuire, M.; Piecuch, P. *J. Phys. Chem. A.* **2005**, *109*, 11643.
(112) Li, Z.; Valero, R.; Truhlar, D. *Theor. Chem. Acc.* **2007**, *118*, 9.
(113) Bonhommeau, D.; Truhlar, D. *J. Chem. Phys.* **2008**, *129*.
(114) Bonhommeau, D.; Valero, R.; Truhlar, D.; Jasper, A. *J. Chem. Phys.* **2009**, *130*.
(115) Lai, W.; Lin, S.; Xie, D.; Guo, H. *J. Chem. Phys.* **2008**, *129*.
(116) Xie, J.; Sha, G.; Zhang, X.; Zhang, C. *Chem. Phys. Lett.* **1986**, *124*, 99.
(117) Biesner, J.; Schnieder, L.; Schmeer, J.; Ahlers, G.; Xie, X.; Welge, K.; Ashfold, M.; Dixon, R. *J. Chem. Phys.* **1988**, *88*, 3607.
(118) Biesner, J.; Schnieder, L.; Ahlers, G.; Xie, X.; Welge, K.; Ashfold, M.; Dixon, R. *J. Chem. Phys.* **1989**, *91*, 2901.
(119) Mordaunt, D.; Ashfold, M.; Dixon, R. *J. Chem. Phys.* **1996**, *104*, 6460.
(120) Mordaunt, D.; Dixon, R.; Ashfold, M. *J. Chem. Phys.* **1996**, *104*, 6472.
(121) Mordaunt, D.; Ashfold, M.; Dixon, R. *J. Chem. Phys.* **1998**, *109*, 7659.
(122) Woodbridge, E.; Ashfold, M.; Leone, S. *J. Chem. Phys.* **1991**, *94*, 4195.
(123) Loomis, R.; Reid, J.; Leone, S. *J. Chem. Phys.* **2000**, *112*, 658.
(124) Yamasaki, K.; Watanabe, A.; Kakuda, T.; Itakura, A.; Fukushima, H.; Endo, M.; Maruyama, C.; Tokue, I. *J. Phys. Chem. A.* **2002**, *106*, 7728.
(125) Bach, A.; Hutchison, J.; Holiday, R.; Crim, F. *J. Chem. Phys.* **2002**, *116*, 4955.
(126) Bach, A.; Hutchison, J.; Holiday, R.; Crim, F. *J. Chem. Phys.* **2002**, *116*, 9315.
(127) Bach, A.; Hutchison, J.; Holiday, R.; Crim, F. *J. Chem. Phys.* **2003**, *118*, 7144.
(128) Bach, A.; Hutchison, J.; Holiday, R.; Crim, F. *J. Phys. Chem. A.* **2003**, *107*, 10490.
(129) Hause, M.; Yoon, Y.; Crim, F. *J. Chem. Phys.* **2006**, *125*.
(130) Hause, M.; Yoon, Y.; Crim, F. *Mol. Phys.* **2008**, *106*, 1127.
(131) Akagi, H.; Yokoyama, K.; Yokoyama, A. *J. Chem. Phys.* **2003**, *118*, 3600.
(132) Liu, H.; Yin, S.; Zhang, J.; Wang, L.; Jiang, B.; Lou, N. *Phys. Rev. A.* **2006**, *74*.
(133) Yin, S.; Liu, H.; Zhang, J.; Jiang, B.; Xu, D.; Wang, L.; Sha, G.; Lou, N. *Chem. Phys. Lett.* **2002**, *356*, 227.
(134) Donnelley, V.; Baronavski, A.; McDonald, *J. Chem. Phys.* **1979**, *43*, 283.
(135) Yamaguchi, Y.; Hoffman, B.; Stephens, J.; Schaefer, H. *J. Phys. Chem. A.* **1999**, *103*, 7701.
(136) Xin, J.; Fan, H.; Ionescu, I.; Annesley, C.; Reid, S. *J. Mol. Spectr.* **2003**, *219*, 37.
(137) Freudenberg, T.; Stert, V.; Radloff, W.; Ringling, J.; Gudde, J.; Korn, G.; Hertel, I. *Chem. Phys. Lett.* **1997**, *269*, 523.
(138) Farmanara, R.; Ritze, H.; Stert, V.; Radloff, W.; Hertel, I. *J. Chem. Phys.* **2002**, *116*, 1443.

(139)   Farmanara, F.; Ritze, H.; Stert, V.; Radloff, W.; Hertel, I. *Eur. Phys. J. D.* **2002**, *19*, 193.

(140)   Lippert, H.; Stert, V.; Schulz, C.; Hertel, I.; Radloff, W. *Phys. Chem. Chem. Phys.* **2004**, *6*, 2718.

(141)   Demtröder, W. *Laser spectroscopy: Basic concepts and instrumentation.* 2nd ed.; Springer-Verlag: Berlin, 1998. pg 335-358.

(142)   Even, U.; Jortner, J.; Noy, D.; Lavie, N.; Cossart-Magos, C. *J. Chem. Phys.* **2000**, *112*, 8068.

(143)   Wiley, W.; McLaren, I. *J. Mass Spectrom.* **1997**, *32*, 4.

(144)   Levy, D. *SCIENCE.* **1981**, *214*, 263.

(145)   Miller, T. *SCIENCE.* **1984**, *223*, 545.

(146)   Gentry, W.; Giese, C. *Rev. Sci. Instrum.* **1978**, *49*, 595.

(147)   Chandler, D.; Houston, P. *J. Chem. Phys.* **1987**, *87*, 1445.

(148)   Eppink, A.; Parker, D. *Rev. Sci. Instrum.* **1997**, *68*, 3477.

(149)   Parker, D. *Acc. Chem. Res.* **2000**, *33*, 563.

(150)   Hause, M.; Yoon, Y.; Case, A.; Crim, F. *J. Chem. Phys.* **2008**, *128*.

(151)   Ashfold, M.; Nahler, N.; Orr-Ewing, A.; Vieuxmaire, O.; Toomes, R.; Kitsopoulos, T.; Garcia, I.; Chestakov, D.; Wu, S.; Parker, D. *Phys. Chem. Chem. Phys.* **2006**, *8*, 26.

(152)   Zare, R. N. *Angular momentum*: Understanding Spatial aspects in chemistry and physics. John Wiley & Sons, 1988. pg 117-119.

(153)   Roberts, G.; Nixon, J.; Lecointre, J.; Wrede, E.; Verlet, J. *Rev. Sci. Instrum.* **2009**, *80*.

(154)   Eppink, A.; Whitaker, B.; Gloaguen, E.; Soep, B.; Coroiu, A.; Parker, D. *J. Chem. Phys.* **2004**, *121*, 7776.

(155)   Form, N.; Whitaker, B.; Poisson, L.; Soep, B. *Phys. Chem. Chem. Phys.* **2006**, *8*, 2925.

(156)   Eppink, A.; Parker, D. *J. Chem. Phys.* **1999**, *110*, 832.

(157)   de Nalda, R.; Izquierdo, J.; Dura, J.; Banares, L. *J. Chem. Phys.* **2007**, *126*.

(158)   de Nalda, R.; Dura, J.; Garcia-Vela, A.; Izquierdo, J.; Gonzalez-Vazquez, J.; Banares, L. *J. Chem. Phys.* **2008**, *128*.

(159)   Dura, J.; de Nalda, R.; Alvarez, J.; Izquierdo, J.; Amaral, G.; Banares, L. *ChemPhysChem.* **2008**, *9*, 1245.

(160)   Dura, J.; de Nalda, R.; Amaral, G.; Banares, L. *J. Chem. Phys.* **2009**, *131*.

(161)   Peoux, G.; Monnerville, M.; Duhoo, T.; Pouilly, B. *J. Chem. Phys.* **1997**, *107*, 70.

(162)   Smolin, A.; Vasyutinskii, O.; Balint-Kurti, G.; Brown, A. *J. Phys. Chem. A.* **2006**, *110*, 5371.

(163)   Valero, R.; Truhlar, D.; Jasper, A. *J. Phys. Chem. A.* **2008**, *112*, 5756.

(164)   Langford, S.; Regan, P.; Orr-Ewing, A.; Ashfold, M. *Chem. Phys.* **1998**, *231*, 245.

(165)   Baumfalk, R.; Buck, U.; Frischkorn, C.; Nahler, N.; Huwel, L. *J. Chem. Phys.* **1999**, *111*, 2595.

(166)   Zare, R. N. *Angular momentum*: Understanding Spatial aspects in chemistry and physics. John Wiley & Sons, 1988. pg 52-66.

(167)   Wells, K. L.; Perriam, G.; Stavros, V. G. *J. Chem. Phys.* **2009**, *130*.

(168)   DeWitt, M.; Levis, R. *J. Chem. Phys.* **1999**, *110*, 11368.

(169)   Levis, R.; DeWitt, M. *J. Phys. Chem. A.* **1999**, *103*, 6493.

(170)   Nix, M. G. D. *private communication.* **2009**

(171)   Iqbal, A.; Cheung, M.; Nix, M.; Stavros, V. *J. Phys. Chem. A.* **2009**, *113*, 8157.

(172)   King, G. A.; Oliver, T. A. A.; Nix, M. G. D.; Ashfold, M. N. R. *J. Phys. Chem. A.* **2009**, *113*, 7984.

(173)   Conti, I.; Garavelli, M.; Orlandi, G. *J. Am. Chem. Soc.* **2009**, *131*, 16108.

(174)   Lin, J.; Yu, C.; Peng, S.; Akiyama, I.; Li, K.; Lee, L.; LeBreton, P. *J. Am. Chem. Soc.* **1980**, *102*, 4627.

(175)   Lin, C.; Matsumoto, J.; Ohtake, S.; Imasaka, T. *TALANTA* **1996**, *43*, 1925.

(176)   Lide, D. R. *Handbook of Chemistry and Physics*; CRC press: Ohio, 1992.

(177)   Wells, K.; Roberts, G.; Stavros, V. *Chem. Phys. Lett.* **2007**, *446*, 20.

(178)   Wells, K. L.; Hadden, D. J.; Nix, M. G. D.; Stavros, V. G. *J. Phys. Chem. Lett.* **2010**, *1*, 993

(179)   Clark, L. B. P., G. G; Tinoco I. Jr; *J. Phys. Chem.* **1965**, *69*, 4.